Fermi National Accelerator Laboratory

FERMILAB-Pub-91/352-E

A Limit on the Top Quark Mass from Proton-Antiproton Collisions at $\sqrt{s}$ = 1.8 TeV

The CDF Collaboration

Fermi National Accelerator Laboratory
P.O. Box 500, Batavia, Illinois 60510

December 1991

* Submitted to *Physical Review D.*

Operated by Universities Research Association Inc. under Contract No. DE-AC02-76CHO3000 with the United States Department of Energy

Disclaimer

A Limit on the Top Quark Mass from Proton-Antiproton Collisions at $\sqrt{s} = 1.8$ TeV

F. Abe,(9) D. Amidei,(4) G. Apollinari,(16) M. Atac,(4) P. Auchincloss,(15) A. R. Baden,(6) N. Bacchetta,(11) M. W. Bailey,(14) A. Bamberger,(4,a) P. de Barbaro,(15) B. A. Barnett,(8) A. Barbaro-Galtieri,(10) V. E. Barnes,(14) T. Baumann,(6) F. Bedeschi,(13) S. Behrends,(2) S. Belforte,(13) G. Bellettini,(13) J. Bellinger,(21) D. Benjamin,(20) J. Bensinger,(2) A. Beretvas,(4) J. P. Berge,(4) S. Bertolucci,(5) S. Bhadra,(7) M. Binkley,(4) R. Blair,(1) C. Blocker,(2) V. Bolognesi,(13) A. W. Booth,(4) C. Boswell,(8) G. Brandenburg,(6) D. Brown,(6) E. Buckley-Geer,(17) H. S. Budd,(15) G. Busetto,(11) A. Byon-Wagner,(4) K. L. Byrum,(21) C. Campagnari,(3) M. Campbell,(3) A. Caner,(4) R. Carey,(6) W. Carithers,(10) D. Carlsmith,(21) J. T. Carroll,(4) R. Cashmore,(4,a) A. Castro,(11) F. Cervelli,(13) K. Chadwick,(4) G. Chiarelli,(5) W. Chinowsky,(10) S. Cihangir,(4) A. G. Clark,(4) D. Connor,(12) M. Contreras,(3) J. Cooper,(4) M. Cordelli,(5) D. Crane,(4) M. Curatolo,(5) C. Day,(4) F. DeJongh,(4) S. Dell'Agnello,(13) M. Dell'Orso,(13) L. Demortier,(2) B. Denby,(4) P. F. Derwent,(3) T. Devlin,(17) D. DiBitonto,(18) M. Dickson,(15) R. B. Drucker,(10) K. Einsweiler,(10) J. E. Elias,(4) R. Ely,(10) S. Eno,(3) S. Errede,(7) B. Esposito,(5) A. Etchegoyen,(4,a) B. Flaugher,(4) G. W. Foster,(4) M. Franklin,(6) J. Freeman,(4) H. Frisch,(3) T. Fuess,(4) Y. Fukui,(9) A. F. Garfinkel,(14) A. Gauthier,(7) S. Geer,(4) D. W. Gerdes,(3) P. Giannetti,(13) N. Giokaris,(16) P. Giromini,(5) L. Gladney,(12) M. Gold,(10) K. Goulianos,(16) H. Grassmann,(11) C. Grosso-Pilcher,(3) C. Haber,(10) S. R. Hahn,(4) R. Handler,(21) K. Hara,(19) R. M. Harris,(4) J. Hauser,(4) C. Hawk,(17) T. Hessing,(18) R. Hollebeek,(12) L. Holloway,(7) P. Hu,(17) B. Hubbard,(10) B. T. Huffman,(14) R. Hughes,(12) P. Hurst,(5) J. Huth,(4) J. Hylen,(4) M. Incagli,(13) T. Ino,(19) H. Iso,(19) H. Jensen,(4) C. P. Jessop,(6) R. P. Johnson,(4) U. Joshi,(4) R. W. Kadel,(10) T. Kamon,(18) S. Kanda,(19) D. A. Kardelis,(7) I. Karliner,(7) E. Kearns,(6) L. Keeble,(18) R. Kephart,(4) P. Kesten,(2) R. M. Keup,(7) H. Keutelian,(4) D. Kim,(4) S. Kim,(19) L. Kirsch,(2) K. Kondo,(19) J. Konigsberg,(6) E. Kovacs,(4) S. E. Kuhlmann,(1) E. Kuns,(17) A. T. Laasanen,(14) J. I. Lamoureux,(21) S. Leone,(13) J. Lewis,(4) W. Li,(1) P. Limon,(4) T. M. Liss,(7) N. Lockyer,(12) C. B. Luchini,(7) P. Lukens,(4) P. Maas,(21) K. Maeshima,(4) M. Mangano,(13) J. P. Marriner,(4) M. Mariotti,(13) R. Markeloff,(21) L. A. Markosky,(21) R. Mattingly,(2) P. McIntyre,(18) A. Menzione,(13) T. Meyer,(18) S. Mikamo,(9) M. Miller,(3) T. Mimashi,(19) S. Miscetti,(5) M. Mishina,(9) S. Miyashita,(19) Y. Morita,(19) S. Moulding,(2) J. Mueller,(17) A. Mukherjee,(4) L. F. Nakae,(2) I. Nakano,(19) C. Nelson,(4) C. Newman-Holmes,(4) J. S. T. Ng,(6) M. Ninomiya,(19) L. Nodulman,(1) S. Ogawa,(19) R. Paoletti,(13) V. Papadimitriou,(4) A. Para,(4) E. Pare,(6) S. Park,(4) J. Patrick,(4) T. J. Phillips,(6) F. Ptohos,(6) R. Plunkett,(4) L. Pondrom,(21) J. Proudfoot,(1) G. Punzi,(13) D. Quarrie,(4) K. Ragan,(12) G. Redlinger,(3) J. Rhoades,(21) M. Roach,(20) F. Rimondi,(4,a) L. Ristori,(13) T. Rodrigo,(4) T. Rohaly,(12) A. Roodman,(3) W. K. Sakumoto,(15) A. Sansoni,(5) R. D. Sard,(7) A. Savoy-Navarro,(4) V. Scarpine,(7) P. Schlabach,(6) E. E. Schmidt,(4) O. Schneider,(10) M. H. Schub,(14) R. Schwitters,(6) A. Scribano,(13) S. Segler,(4) Y. Seiya,(19) M. Shapiro,(10) N. M. Shaw,(14) M. Sheaff,(21) M. Shochet,(3) J. Siegrist,(10) P. Sinervo,(12) J. Skarha,(8) K. Sliwa,(20) D. A. Smith,(18) F. D. Snider,(8) L. Song, (12) M. Spahn,(10) P. Sphicas,(4) R. St. Denis,(6) A. Stefanini,(13) G. Sullivan,(3) R. L. Swartz, Jr.,(7) M. Takano,(19) F. Tartarelli,(13) K. Takikawa,(19) S. Tarem,(2) D. Theriot,(4) M. Timko,(18) P. Tipton,(4) S. Tkaczyk,(4) A. Tollestrup,(4) J. Tonnison,(14) W. Trischuk,(6) N. Turini,(13) Y. Tsay,(3) F. Ukegawa,(19) D. Underwood,(1) S. Vejcik, III,(8) R. Vidal,(4) R. G. Wagner,(1) R. L. Wagner,(4) N. Wainer,(4) J. Walsh,(12) T. Watts,(17) R. Webb,(18) C. Wendt,(21) H. Wenzel,(13) W. C. Wester, III,(10) T. Westhusing,(18) S. N. White,(16) A. B. Wicklund,(1) H. H. Williams,(12) B. L. Winer,(15) J. Wyss, (11) A. Yagil,(4) K. Yasuoka,(19) G. P. Yeh,(4) J. Yoh,(4) M. Yokoyama,(19) J. C. Yun,(4) A. Zanetti,(13) F. Zetti,(13) S. Zucchelli (4,a)

The CDF Collaboration

(1) *Argonne National Laboratory, Argonne, Illinois 60439*
(2) *Brandeis University, Waltham, Massachusetts 02254*
(3) *University of Chicago, Chicago, Illinois 60637*
(4) *Fermi National Accelerator Laboratory, Batavia, Illinois 60510*
(5) *Laboratori Nazionali di Frascati, Istituto Nazionale di Fisica Nucleare, Frascati, Italy*
(6) *Harvard University, Cambridge, Massachusetts 02138*
(7) *University of Illinois, Urbana, Illinois 61801*
(8) *The Johns Hopkins University, Baltimore, Maryland 21218*

(9) *National Laboratory for High Energy Physics (KEK), Japan*
(10) *Lawrence Berkeley Laboratory, Berkeley, California 94720*
(11) *Universita di Padova, Instituto Nazionale di Fisica Nucleare, Sezione di Padova, I-35131 Padova, Italy*
(12) *University of Pennsylvania, Philadelphia, Pennsylvania 19104*
(13) *Istituto Nazionale di Fisica Nucleare, University and Scuola Normale Superiore of Pisa, I-56100 Pisa, Italy*
(14) *Purdue University, West Lafayette, Indiana 47907*
(15) *University of Rochester, Rochester, New York 14627*
(16) *Rockefeller University, New York, New York 10021*
(17) *Rutgers University, Piscataway, New Jersey 08854*
(18) *Texas A&M University, College Station, Texas 77843*
(19) *University of Tsukuba, Tsukuba, Ibaraki 305, Japan*
(20) *Tufts University, Medford, Massachusetts 02155*
(21) *University of Wisconsin, Madison, Wisconsin 53706*

Abstract

We present results of searches for the top-quark in $p\bar{p}$ collisions at $\sqrt{s} = 1.8$ TeV. The data sample was collected during 1988-1989 at the Fermilab Tevatron Collider and has an integrated luminosity of 4.1 pb^{-1}. We have extended our previous search for $e\mu$ final states to include the ee and $\mu\mu$ channels. In addition, we have searched for a low transverse momentum muon as a tag of the bottom quark in top decay events with a lepton and at least two jets. We obtain a lower limit on the top quark mass of 91 GeV/c^2 at the 95% confidence level assuming Standard Model charged current decays.

1 Introduction

The Standard Model [1, 2] predicts the existence of a weak isospin partner of the bottom quark called the top quark (t). Although the absence of flavor-changing neutral currents in bottom quark (b) decays [3] and the forward-backward asymmetry in $e^+e^- \rightarrow b\bar{b}$ [4] imply the existence of an isodoublet partner of the b, the top quark has yet to be observed.

Searches for the top quark at the CERN $p\bar{p}$ collider with $\sqrt{s} = 0.63$ TeV by the UA1 and UA2 collaborations have resulted in lower limits on M_{top} of 60 GeV/c^2 and 69 GeV/c^2 respectively [5, 6]. For these searches it was assumed that the top quark decays according to the Standard Model charged current decay, into a virtual W boson and a bottom quark. Direct searches for the top quark in e^+e^- collisions have placed lower limits as high as 46 GeV/c^2 on the top mass (M_{top}) [7], independent of decay modes. A limit $M_{top} > 44$ GeV/c^2 at the 95% C.L. independent of the top decay modes has also been inferred from the value of the W width derived from the CDF measurement of the ratio of W and Z production cross sections [8]. Lower bounds of about 50 GeV/c^2 on M_{top} have been obtained from fits to Standard Model parameters in order to account for the observed level of $B^0\bar{B}^0$ mixing [9], and upper limits of about 200 GeV/c^2 have been placed by requiring consistency with the measured W and Z boson masses [10, 11, 12], with weak neutral-current data, and with precision measurements of charge asymmetries in Z decays [13].

In previous publications, CDF has reported limits on M_{top} of 72 GeV/c^2 from a search for $p\bar{p} \rightarrow t\bar{t} \rightarrow e\mu + X$ [14], and of 77 GeV/c^2 from a search for $p\bar{p} \rightarrow t\bar{t} \rightarrow e + jets$ [15]. These results have been recently superseded by newer analyses resulting in a lower limit on the top quark mass of 91 GeV/c^2 at the 95 % C.L.[16]. In this paper, we present a more detailed account of the analysis of Reference [16]. The results are based on a 4.1 pb^{-1} data sample collected during 1988-1989 at the Fermilab Tevatron Collider at a center of mass energy of $\sqrt{s} = 1.8$ TeV [17].

At $\sqrt{s} = 1.8$ TeV, the dominant top quark production process is expected to be $p\bar{p} \rightarrow t\bar{t}$ [18, 19]. If the top quark is lighter than the W boson, the mechanism $p\bar{p} \rightarrow W \rightarrow t\bar{b}$ is also possible, but has much smaller cross section than direct $t\bar{t}$ production, except for M_{top} near 60 GeV/c^2 where the rates are similar. For the analyses described in this paper we only consider the direct production of top quark-antiquark pairs. We also assume that each t or $\bar{t}$ quark decays, according to the Standard Model, via the weak charged current into a W boson and a b quark ($t \rightarrow Wb$). The W can be real or virtual depending on M_{top}, and decays into either a charged lepton and a neutrino,

Decay Mode	Branching Ratio
$t\bar{t} \rightarrow q\bar{q}\ b\ q\bar{q}\ \bar{b}$	36/81
$t\bar{t} \rightarrow q\bar{q}\ b\ e\ \nu\ \bar{b}$	12/81
$t\bar{t} \rightarrow q\bar{q}\ b\ \mu\nu\ \bar{b}$	12/81
$t\bar{t} \rightarrow q\bar{q}\ b\ \tau\nu\ \bar{b}$	12/81
$t\bar{t} \rightarrow e\ \nu\ b\ \ \mu\nu\ \bar{b}$	2/81
$t\bar{t} \rightarrow e\ \nu\ b\ \ \tau\nu\ \bar{b}$	2/81
$t\bar{t} \rightarrow \mu\nu\ b\ \ \tau\nu\ \bar{b}$	2/81
$t\bar{t} \rightarrow e\ \nu\ b\ \ e\ \nu\ \bar{b}$	1/81
$t\bar{t} \rightarrow \mu\nu\ b\ \ \mu\nu\ \bar{b}$	1/81
$t\bar{t} \rightarrow \tau\nu\ b\ \ \tau\nu\ \bar{b}$	1/81

Table 1: Decay modes of the $t\bar{t}$ pair and their branching ratios assuming charged current decays. The symbol q denotes a light quark : u, d, c or s.

or two light quarks, as predicted by the Standard Model. The possible decay modes and their branching ratios are listed in Table 1.

Decay modes of the $t\bar{t}$ pair where both quarks decay hadronically are expected to have a high branching fraction (36/81), but are difficult to distinguish from large multi-jet backgrounds. Given the good electron and muon identification capabilities of the CDF detector, a significant improvement in the signal-to-background can be achieved for modes in which one of the top quarks decays semileptonically. Because of the large top mass, leptons from top decay are expected to have high transverse momentum (P_T, see Figure 1). The top searches described in this paper require the detection of at least one high transverse momentum ($P_T > 15$ GeV/c) electron or muon. The high-P_T lepton requirement is useful to supress large backgrounds from semileptonic decays of bottom and charm quarks.

In extensions of the Standard Model, the decay of the top quark into charged Higgs bosons, $t \rightarrow Hb$, could have an important rate if $M_H < M_{top}$ [20]. The preferred decay of the charged Higgs in most models is $H \rightarrow \tau\nu$ or $c\bar{s}$. Semileptonic decays of the b or c quarks, or leptonic decays of a τ in these events, occasionally give high P_T electrons or muons. We do not further consider this non-standard decay mode in this paper.

Two separate analyses are described in this report. First, an extension of the previous high-P_T $e\mu$ analysis of Reference [14] in which have added the channels ee and $\mu\mu$. The search has also been extended to include electrons at smaller polar angles relative to the beam. Second, we have searched in events with a high-P_T lepton and more than two jets ($lepton + jets$ events), for a low transverse momentum muon as a tag of a bottom quark in $t\bar{t} \rightarrow W^+bW^-\bar{b}$ decays.

The paper is organized as follows : Section 2 summarizes the features of the CDF detector relevant for these analyses; Sections 3- 6 describe the lepton triggers, lepton selection and lepton isolation; the jet and missing transverse energy algorithms and the Monte Carlo are discussed in Sections 7 and 8; the searches for the top quark in the dilepton channel ($t\bar{t} \rightarrow ee, e\mu$, or $\mu\mu$) and in the $lepton + jets$ (with $b \rightarrow \mu$ tag) channel are presented in Sections 9 and 10. Finally, in Section 11 we combine the results of these searches and we extract a lower limit on the mass of the top quark.

2 The CDF Detector

The CDF detector (see Figure 2) has been described in detail elsewhere[21] and will only briefly be reviewed here. Scintillator planes located at small angles with respect to the beam directions are used to tag inelastic events. A vertex time projection chamber (VTPC) provides tracking information up to a radius of 22 cm from the beam axis for $|\eta| < 3.25$, where $\eta = -\ln(\tan(\theta/2))$ is the pseudorapidity and θ is the polar angle relative to the proton beam direction [22]. In the analyses presented here, this chamber is used to measure the position of the interaction vertex along the beam axis with a resolution of 1 mm and to aid in the identification of photon conversions. At larger radii, an 84-layer central tracking chamber (CTC) measures charged particle momenta for $|\eta| \leq 1.2$ in a 1.4 Tesla magnetic field with a precision of $\delta P_T/P_T^2 \simeq 0.0011$ $(\mathrm{GeV}/c)^{-1}$ for beam-constrained tracks [10].

Outside the tracking chambers, electromagnetic (EM) and hadronic (HAD) calorimeters are arranged in a fine-grained, projective tower geometry covering most of the 4π solid angle. The calorimeters are divided into three regions of pseudorapidity: central ($|\eta| < 1.1$), plug ($1.1 < |\eta| < 2.4$), and forward ($2.4 < |\eta| < 4.2$). The central EM and HAD calorimeters consist of lead-scintillator and iron-scintillator sandwiches respectively. In the plug and forward regions the calorimeters are constructed with gas proportional chambers. The segmentation of the calorimeters is $\Delta\eta \times \Delta\phi = 0.1 \times 15^\circ$ in the central region and $\Delta\eta \times \Delta\phi = 0.1 \times 5^\circ$ in the plug and forward regions. The calorimeter systems are summarized in Table 2. In the region $|\eta| < 1.1$, the EM calorimeters have proportional wire chambers with cathode strips perpendicular to the wires (strip chambers) embedded at a depth of six radiation lengths. These strip chambers measure the lateral shape and position of EM showers and are used for

System	η Range	Energy Resolution	Thickness
CEM	$\lvert\eta\rvert < 1.1$	$13.5\%/\sqrt{E_t} \oplus 2\%$	18 X_0
PEM	$1.1 < \lvert\eta\rvert < 2.4$	$28\%/\sqrt{E} \oplus 2\%$	18-21 X_0
FEM	$2.4 < \lvert\eta\rvert < 4.2$	$25\%/\sqrt{E} \oplus 2\%$	25 X_0
CHA	$\lvert\eta\rvert < 1.3$	$75\%/\sqrt{E_t} \oplus 3\%$	4.5 λ_0
PHA	$1.3 < \lvert\eta\rvert < 2.4$	$90\%/\sqrt{E} \oplus 4\%$	5.7 λ_0
FHA	$2.4 < \lvert\eta\rvert < 4.2$	$130\%/\sqrt{E} \oplus 4\%$	7.7 λ_0

Table 2: Summary of CDF calorimeter properties. The symbol $\oplus$ signifies that the constant term is added in quadrature in the resolution. Thicknesses are given in radiation lengths for electromagnetic calorimeters and absorption lengths for hadronic calorimeters. The EM resolutions are for electrons and photons; the HAD resolutions are for isolated pions.

electron and photon identification.

Outside of the central calorimeter, the region $|\eta| < 0.63$ is instrumented with four layers of drift chambers for muon detection. The central calorimeter has a thickness of approximately five absorption lengths for incident hadrons. Muons of momenta below approximately 1.6 GeV/c stop in the calorimeter without reaching the muon detector. In both the forward and backward region there is a muon spectrometer consisting of magnetized steel toroids with drift chamber planes and trigger scintillation counters.

	Central Electron	Plug Electron	Central Muon
Level 1 (μb)	22	88	255
Level 2 (μb)	0.49	0.16	1.1
Level 3 (μb)	0.25	0.11	0.13

Table 3: Cross sections for lepton triggers. The thresholds for the different triggers are described in the text. At the typical luminosity of 10^{30} cm^{-2}s^{-1}, a cross section of 1 μb corresponds to an event rate of 1 Hz.

3 Lepton Triggers

CDF employed a four level trigger system [23]. The lowest level trigger, level 0, required a coincidence between hits in the forward and backward scintillation hodoscopes (beam-beam counters) to select beam crossings with inelastic interactions. The beam-beam counters have an effective cross section of 47±3 mb [8, 24], which represents an event rate of 47 KHz at the typical Tevatron luminosity during the 1988-1989 run of 10^{30} cm^{-2}s^{-1}. The next 3 levels of triggering reduced this to a rate of 1-2 Hz, at which events could be written to tape. The cross sections for the lepton triggers discussed in this section are presented in Table 3.

The level 1 trigger consisted of a logical OR of a number of triggers designed for the detection of electrons, muons and jets. The first level electron trigger used information exclusively from the calorimeters, which at the trigger level was available with a segmentation $\Delta\eta \times \Delta\phi = 0.2 \times 15°$. The central electron trigger required at least one EM tower in the central region with E_T above a threshold of 3 GeV. Plug electrons were collected with a trigger that required at least one EM tower, in any region of the calorimeter, with more than 6 GeV of transverse energy. The level 1 muon trigger[25] was based solely on the muon chamber information. The track direction is measured using the arrival times of of the drift electrons at the sense wires in the chamber. Using the constraint that the track had to originate at the beamline, and knowing the line integral of the magnetic field traversed by the particle, this measurement could be turned into a measurement of the transverse momentum of the track. Events with tracks in the central muon chambers of P_T greater than a programmable threshold were accepted. This threshold was initially set at 5 GeV/c and was later lowered to 3 GeV/c; in both cases the efficiency for high transverse momentum muons ($P_T > 15$ GeV/c) was measured to be above 90%.

The level 2 trigger included a large number of triggers optimized to be sensitive to many different physics processes. It was based on a list of calorimeter clusters provided by a nearest-neighbor hardware cluster finder as well as information from a hardware track processor (CFT)[26]. Here we briefly describe the level 2 triggers relevant for the top searches, namely the inclusive electron and muon triggers.

The electron and muon triggers in the central region used transverse track projections found by the track processor. This device processes fast timing information from the CTC to identify high P_T tracks in the Rϕ plane by comparing the CTC hits with predetermined patterns. The processor has a momentum resolution $\delta P_T/P_T^2 \simeq 0.035($ GeV/c$)^{-1}$. The track finding efficiency of the CFT was $98.0 \pm 0.5\%$.

The central electron trigger required the existence of a CFT-track of $P_T > 6$ GeV/c pointing to an electromagnetic cluster of $E_T > 12$ GeV. An electromagnetic cluster was constructed as a set of contiguous EM trigger towers each with $E_T >$ 3.6 GeV, with at least one tower (the seed tower) with $E_T >$ 4 GeV, and with less than 12.5% of the energy in the corresponding cells of the hadronic calorimeter. In the plug region, where no tracking information was available, the electron trigger simply required the existence of an electromagnetic cluster with E_T above a nominal threshold of 23 GeV. The central muon trigger required a match within 15° in ϕ between a track-segment in the muon chambers and a CFT-track with $P_T > 9$ GeV/c.

Trigger efficiencies as a function of E_T or P_T were measured from samples of events collected with independent triggers and are displayed in Figure 3. With a 12 GeV threshold, the trigger efficiency for isolated central electrons of $E_T > 15$ GeV was determined to be $98.0 \pm 0.5\%$ from a study of W and Z events. The slow turn-on of the efficiency curve for the plug electron trigger was caused by several effects : (i) the trigger calculation of transverse energy assumed that the interaction occurred at z=0 (the z-vertex distribution had a standard deviation of 30 cm); (ii) the trigger only used information from one of the three depth segments of the PEM, and the gains in the trigger could only be adjusted to compensate for the partial sampling in an average way; (iii) there were gain variations in the PEM quadrants that were corrected in the offline analysis but that were not considered in the trigger; (iv) there was a small number of non- functioning chambers in the PEM which caused a degradation in the response of the calorimeter which was also not accounted for in the trigger thresholds. The efficiency of the plug electron trigger was $50 \pm 6\%$ at $E_T = 30$ GeV. The combined level 1 and level 2 trigger efficiency for central muons of $P_T > 15$ GeV/c was determined to be $91 \pm 2\%$. The inefficiency was found to be dominated by the level 1 inefficiency, and is caused mostly by delta rays that affect the angle measurement in the muon chambers. Because of a hardware malfunction during the early part of the run, only 3.5 $\text{pb}^{-1}$of data were collected with the muon trigger. Data samples collected by the muon trigger are treated as having the full integrated luminosity (4.1 pb^{-1}) and a correction is applied to the trigger efficiency to account for the difference in sample size.

The final layer of triggering, level 3[27] consisted of a farm of 60 Fermilab Advanced Computer Program (ACP) [28] modules running a streamlined version of the CDF offline reconstruction code. Due to constraints on execution time, only transverse track projections were reconstructed. For central electrons, the level 3 algorithm required that the reconstructed cluster energy be above the level 2 threshold, and that there be a track with $P_T > 6$ GeV/c pointing to it. For plug electrons the only requirement at level 3 was that the reconstructed E_T be above 7.5 GeV. The muon level 3 algorithm required a match of better than 10 cm in ϕ between a track of $P_T > 11$ GeV/c and a track-segment in the muon chambers.

4 Electron Identification in CDF

Electron identification in CDF has been described in earlier publications [15],[8] and will only be summarized here. In the $e + jets$ analysis we consider electrons in the central rapidity region ($|\eta| \leq 1.0$). For the dilepton search, electrons in the plug calorimeter ($1.1 \leq |\eta| \leq 2.4$) are also included.

4.1 Central Electrons

Central electron candidates have a CTC track that extrapolates to an electromagnetic cluster in the central calorimeter. An EM cluster is constructed starting from a seed tower with $E_T >$ 3 GeV and including neighboring towers with $E_T >$ 100 MeV. The size of the cluster is limited to 3 towers in pseudorapidity ($\Delta\eta = 0.3$) by 1 tower in azimuth ($\Delta\phi = 15°$). The energy in the corresponding hadronic towers must be less than 12.5 % of the energy of the electromagnetic towers. Fiducial cuts on the position of the strip chamber shower are applied to be away from calorimeter boundaries to ensure that energy is well measured. The electron fiducial volume covers 84 % of the solid angle in the region $|\eta| < 1.0$.

The following electron identification variables can be be used to discriminate against charged hadrons : (i) the hadronic energy fraction of the cluster, HAD/EM; (ii) the ratio of cluster energy to track momentum, E/P; (iii) a comparison of the lateral shower profile in the calorimeter cluster with that of test beam electrons, Lshare; (iv) the distance between the extrapolated track position and the strip chamber shower position measured in the ϕ (azimuth) and z (along the beam direction) views, Δx and Δz; and (v) a chi-squared comparison of the strip chamber shower profiles the ϕ and z views with those of test beam electrons, $\chi^2_\phi$and χ^2_z.

The distributions of the identification variables before cuts are shown in Figure 4 for electrons from a sample of $Z \to ee$ events. The selection of this electron sample, which is used to determine cut efficiencies, is described in Section 4.1.3.

Electrons from converted photons can be removed [15] with high efficiency (88 ± 4%) using tracking information. Any electron without a matching VTPC track or with an oppositely charged CTC track forming a low e^+e^- effective mass is rejected as a photon conversion candidate. The first requirement rejects conversions occurring at radii larger than the VTPC inner radius, and the second requirement also rejects electrons from Dalitz decays of neutral pions. The number of non-conversion electrons mistakenly rejected by this algorithm depends on the density of tracks near the electron. In the inclusive electron sample, which consists predominantly of electrons from bottom decay, it is estimated that approximately 5% of prompt electrons are rejected by these requirements.

In the top search, where electrons from semileptonic decays of the top quark are expected to be well separated from jet activity, we add lepton isolation requirements that reduce backgrounds from misidentified hadrons, photon conversions, and bottom or charm decays. A discussion of lepton isolation is given in Section 6.

The two analyses (dileptons and $e + jets$) presented in this paper use similar central electron selection cuts. The requirements used are listed in Table 4, and are discussed below.

4.1.1 Central Electrons in the Dilepton Analysis

For events in which both electrons are in the central region, one electron is required to pass a strict set of cuts and the second electron is required to pass a loose set of cuts. This gives better efficiency than applying strict cuts on both electrons, and still provides good background rejection. The strict set of cuts is used in dilepton categories containing only one central electron (eg. $e\mu$ and central electron - plug electron events). The loose and strict central electron cuts used in the dilepton analysis are listed Table 4.

In addition to the basic identification criteria, an explicit isolation requirement is imposed on the central electron candidates to minimize backgrounds from misidentified hadrons and electrons from bottom or charm decays. We require $E_T^{cone} < 5$ GeV, where E_T^{cone} is the total transverse energy in towers inside a cone of $R \equiv \sqrt{(\Delta\phi)^2 + (\Delta\eta)^2} = 0.4$ centered around the electron, excluding the EM and HAD depositions in the electron cluster.

4.1.2 Central Electrons in the $e + jets$ Analysis

For the $e + jets$ top search we have kept the same electron selection requirements of the earlier analysis of Reference [15]. With only one high-P_T lepton required, backgrounds are larger than in the dilepton case. For this reason, the $e+jets$ electron cuts need to be somewhat more stringent than the strict electron cuts of the dilepton analysis (see Table 4).

Since in the $e+jets$ channel top events are characterized by significant jet activity, we use an isolation requirement that is only sensitive to the energy deposited in the immediate vicinity of the electron. Specifically, the sum of the E_T (E_T^{iso}) in the calorimeter towers surrounding the electron cluster is required to be below 2 GeV.

4.1.3 Central Electron Detection Efficiencies

The efficiencies of the electron identification criteria are determined from a sample of $Z \rightarrow ee$ events [15], except for the isolation requirement, whose efficiency is estimated from the ISAJET [30] top Monte Carlo program and the full detector simulation [31]. Distributions of the electron quality variables for electrons from $Z \rightarrow ee$

Variable	Strict Cuts	Loose Cuts	$e + jets$ Cuts
E_T	> 15 GeV	> 15 GeV	> 20 GeV
HAD/EM	< 0.05	$< 0.055 + 0.045 E_T/100$	< 0.05
P_T	> 10 GeV/c	> 10 GeV/c	-
E/P	< 2.0	-	< 1.5
Lshare	< 0.2	-	< 0.2
Δx	< 1.5 cm	-	< 1.5 cm
Δz	< 3.0 cm	-	< 3.0 cm
χ^2_z	< 10	-	< 10
χ^2_ϕ	-	-	< 10
Isolation	$E_T^{cone} <5$ GeV	$E_T^{cone} < 5$ GeV	$E_T^{iso} < 2$ GeV

Table 4: Central electron identification requirements.

Variable	Strict Cuts	Loose Cuts	$e + jets$ Cuts
HAD/EM	0.97	0.99	0.97
E/P	0.96	-	0.91
Lshare	0.98	-	0.98
Δx	0.98	-	0.98
Δz	0.99	-	0.99
χ^2_z	0.95	-	0.95
χ^2_ϕ	-	-	0.86
Combined	0.88 ± 0.03	0.99 ± 0.01	0.77 ± 0.03

Table 5: Efficiency of the central electron identification requirements. The errors are statistical.

events are shown in Figure 4. A pure sample of Z events was obtained by requiring first an electron candidate passing the strict selection requirements and then a second isolated EM cluster such that the pair forms a mass between 80 and 105 GeV/c^2. Since the cuts on the electron identification variables were not applied on the second electrons, they constitute an unbiased sample. In Figure 4 we display the electron variables for the second cluster. In the cases where both clusters satisfy the strict selection requirement, we include an entry in the plot for each electron.

The central electron identification efficiencies for the different selections are summarized in Table 5. They are found to be 88 ± 3%, 99 ± 1% and 77 ± 3% for the strict, loose, and $e + jets$ selection criteria, excluding the 5 % loss of prompt electrons associated with the conversion removal. The lepton isolation requirements result in a further loss of efficiency which varies slightly with top mass. For a 90 GeV/c^2 top mass, the efficiencies of these requirements are about 85% for both the dilepton and $e + jets$ analyses.

4.2 Plug Electrons

Electromagnetic clusters in the plug calorimeter are constructed in the same manner as in the central calorimeter, except that cluster size can be as large as 5 towers in pseudorapidity ($\Delta\eta = 0.5$) by 5 towers in azimuth ($\Delta\phi = 25°$) [29]. Electron candidates are selected by imposing the following requirements on plug EM clusters: (i) HAD/EM < 0.1 ; (ii) the shower profile in the transverse direction be consistent with test beam results, $\chi^2_{trans} < 10$; (iii) the existence of a match between a track and a cluster in the calorimeter; because the CTC tracking efficiency drops to approximately 50% at $|\eta| = 2$, VTPC tracks are also used; (iv) there be at least 70% of the predicted number of hits in the VTPC (N_{VTPC}) pointing to the cluster; (v) the shower be away from the edges of the calorimeter to ensure a reliable energy measurement. This last fiducial requirement reduces the pseudorapidity coverage of the plug calorimeters to $1.26 < |\eta| < 2.22$ and the ϕ coverage by 11%.

In addition, two isolation requirements are imposed on plug electrons : (i) $I \equiv E_T^{cone}/E_T < 0.1$, where E_T^{cone} is the transverse energy deposited in the calorimeter in a cone of $\Delta R = 0.4$ centered around the electron candidate, excluding the electron EM deposition, and E_T is the transverse energy of the electron; and (ii) there is at most one CTC track with $P_T >$ 5 GeV/c pointing to the EM cluster. We note that at low E_T, the calorimeter isolation cut chosen for plug electrons is more stringent than for central electrons. This helps reject particle misidentification backgrounds the plug

Variable	Cut
E_T	$>$ 15 GeV or 30 GeV
HAD/EM	$<$ 0.10
χ^2_{trans}	$<$ 10
N_{VTPC}	$>$ 70%
Track match	require CTC or VTPC track
Isolation	I $<$ 0.1
	at most 1 CTC-track with $P_T>$ 5 GeV/c

Table 6: Plug electron identification requirements.

region, where the electron identification cuts are less powerful than in the central region, especially because of the limited use of CTC tracks (no E/P requirement).

Plug electrons in the dilepton analysis are required to have E_T $>$ 15 GeV, except for those event types (see Section 9) where we must rely on the plug electron to trigger the apparatus. In those cases, the plug electron threshold in the analysis is raised to 30 GeV, where the trigger is $\simeq$ 50% efficient (see Figure 3).

The plug electron selection requirements are summarized in Table 6. All of the efficiencies, except the isolation efficiency, are determined from a sample of $Z \rightarrow ee$ events. These events are selected by requiring one central electron satisfying the strict cuts discussed in Section 4.1.1 and an isolated plug EM cluster of $E_T>$ 25 GeV such that the invariant mass of the pair is between 80 and 100 GeV/c^2. This selection results in 89 events; the plug electron efficiency is found to be 0.79 ± 0.04 (statistical error).

The efficiencies for the plug electron requirements are listed in Table 7. Distribu-

Cut	Efficiency
HAD/EM	> 0.99
χ^2_{trans}	0.96 ± 0.03
N_{VTPC}	0.94 ± 0.02
Track matching	0.84 ± 0.04
Combined	0.79 ± 0.04

Table 7: Efficiency of the plug electron identification requirements

tions of HAD/EM and of χ^2_{trans} for plug electron candidates from W decays with a matching track are displayed in Figure 5. The plug electron isolation efficiency for top events is estimated from the ISAJET Monte Carlo and the detector simulation. For $M_{top} = 90$ GeV/c^2, the efficiency is 87 %.

Since the expected η distribution of plug electrons in top events is different from that of electrons from W/Z decays, we must examine the rapidity dependence of the plug electron selection. The only requirement that is found to vary significantly as a function of rapidity is the one on the CTC track matching. However, the track matching cut that is applied is the logical OR of the CTC and VTPC matching requirements. Since the latter requirement has high efficiency at large η, the combination of the two has negligible rapidity dependence (See Figure 6).

5 Muon Identification in CDF

In this section we will describe selection criteria for muons in the rapidity interval $|\eta| < 1.2$. For the analyses discussed in this paper we are interested in the detection of high P_T (> 15 GeV/c) muons from $t \rightarrow Wb, W \rightarrow \mu\nu$ decays as well as much lower P_T muons from the decay chains $t \rightarrow b \rightarrow \mu$ or $t \rightarrow b \rightarrow c \rightarrow \mu$. Muons in the forward muon detectors are not considered since their contribution to the total acceptance is small.

5.1 High P_T muons

High transverse momentum muons are identified in the region $|\eta| <1.2$ by requiring that the tower to which the candidate track extrapolates has energy deposition consistent with that of a minimum ionizing particle. The region $|\eta| <0.6$ is instrumented with muon chambers, outside of the central calorimeters, providing a means of triggering and improved muon identification.

The energy deposited in the calorimeters by muons from cosmic rays passing near the beamline is shown in Figure 7. In order to suppress backgrounds from hadrons that interact in the calorimeters, we ask that the energy deposited by muon candidates from top decay be consistent with that of a minimum ionizing particle. In the dilepton analysis the energy deposited is required to be below 2 GeV in the EM compartment and below 6 GeV in the hadronic compartment. In the $\mu+jets$ analysis the HAD requirement is slightly tighter, since backgrounds are higher when only one high P_T charged lepton is required. We demand that the sum of the energy deposited in the EM and HAD calorimeters be less than 5 GeV. To ensure that the energy deposited is well measured, we reject muons that are near a crack in the calorimeter. This requirement defines a muon fiducial volume that covers 85% of the solid angle for $|\eta| \leq 1.2$. From samples of muons from cosmic rays, $Z \rightarrow \mu\mu$, and $J/\psi \rightarrow \mu\mu$

decays the minimum ionization requirements have been determined to be 98 ± 1% and 97 ± 1% efficient for the dilepton and $\mu + jet$ selection requirements respectively.

All CTC track candidates are required to pass a number of quality requirements. The reconstructed track must be within 0.5 cm from the beamline in the transverse plane and within 5 cm of the interaction vertex in the z-direction. These requirements are helpful in rejecting cosmic rays and misreconstructed tracks. Their efficiency is measured to be $> 99\%$ using a sample of electron tracks from $W \rightarrow e\nu$ decays.

For muon candidates within the solid-angle subtended by the muon chambers, we demand a match in ϕ between the extrapolated track and the hits in the muon chambers. In Figure 8 we show the distance δ_x between the extrapolated track and the hits in the muon chambers for a sample of high P_T muons. In the dilepton analysis we only impose a very loose matching requirement, $|\delta_x| < 10$ cm; in the $\mu + jets$ analysis, where we need more rejection against interacting hadronic showers that leak into the muon chambers, the requirement is $|\delta_x| < 1.5$ cm.

To determine the efficiency of the $|\delta_x|$ cut, we selected a sample of minimum ionizing dimuon candidates with pair invariant mass between 70 and 110 GeV/c^2. From this sample of $Z \rightarrow \mu\mu$ candidates, the efficiencies for the $|\delta_x| < 10$ cm and $|\delta_x| < 1.5$ cm requirements are determined to be $> 99\%$ and $90 \pm 3\%$ respectively. In the latter case the inefficiency is due to delta rays.

Finally, just as in the electron case, we impose isolation requirements on possible $t \rightarrow \mu$ candidates. In the dilepton analysis we impose the same isolation requirement used on central electrons, $E_T^{cone} < 5$ GeV; in addition the sum of the transverse momenta of all tracks excluding the muon in a cone of 0.4 centered around the muon (P_T^{cone}) must be < 5 GeV/c. In the $\mu + jets$ analysis we require $E_T^{iso} < 1.5$ GeV, where

Variable	Dilepton Analysis Cuts	$\mu + jets$ Cuts
P_T	> 15 GeV	> 20 GeV
η range	$\lvert\eta\rvert \leq 1.2$	$\lvert\eta\rvert \leq 0.63$
Impact parameter	< 5 mm	< 5 mm
z-vertex match	< 5 cm	< 5 cm
EM energy	EM < 2 GeV	EM < 2 GeV
HAD energy	HAD < 6 GeV	EM + HAD < 5 GeV
$\lvert\delta x\rvert$	< 10 cm ($\lvert \eta \rvert \leq 0.63$)	< 1.5 cm
Isolation	$E_T^{cone} < 5$ GeV, $P_T^{cone} < 5$ GeV/c	$E_T^{iso} < 1.5$ GeV

Table 8: Identification requirements for high transverse momentum muons.

the transverse energy is summed over the eight towers surrounding the one traversed by the muon candidate. For $M_{top} = 90$ GeV/c^2, the efficiencies of the isolation requirements are 85% and 80% for the dilepton and $\mu + jets$ analyses respectively. The high P_T muon selection requirements and efficiencies are summarized in Tables 8 and 9.

5.2 Muons from bottom decay in top events

For top masses not much higher than the W mass, the P_T spectrum of the bottom quarks in the decay t $\rightarrow$ Wb is expected to be soft (see Figure 9). For this reason muons from bottom decays tend to have low transverse momentum (see Figure 10).

Since calorimeter information alone is not sufficient to separate muons from hadrons

Cut	Dilepton Analysis Efficiency	$\mu + jets$ Efficiency
Impact parameter	> 0.99	> 0.99
z-vertex match	> 0.99	> 0.99
EM & HAD cuts	0.98	0.97
$\|\delta x\|$	> 0.99	0.90
Combined	$98 \pm 1\%$	$87 \pm 3\%$

Table 9: Efficiencies for the high transverse momentum muon selection requirements.

in this P_T region, the acceptance for muons from $t \rightarrow b \rightarrow \mu$ and $t \rightarrow b \rightarrow c \rightarrow \mu$ is limited to the region covered by the muon chambers ($| \eta | \leq 0.63$). Furthermore, no mimumum ionizing requirement is imposed on the muon candidates, since muons from b and c-decays are not expected to be isolated. The only requirements are that (i) the muon candidate track pass the same quality requirements listed in the previous Section and (ii) that the extrapolated CTC track match with the track segment in the muon chambers.

At the transverse momenta of interest, multiple scattering causes the matching between the track and the hits in the muon chambers to be significantly worse than for the high P_T muons discussed in the previous Section. We require $|\delta_x| < 15$ cm for $P_T < 4$ GeV/c and $|\delta_x| < 60$ cm$/P_T$ (GeV/c) at higher transverse momentum. The identification requirements are summarized in Table 10.

To evaluate the efficiency of the $|\delta_x|$ requirement, we examine a sample of $J/\psi \rightarrow \mu\mu$ decays. Figure 11 shows the invariant mass distribution of all oppositely charged dimuon candidates in the region of the J/ψ; these events were selected by requiring

Variable	Requirement
P_T	2 GeV/c $< P_T <$ 15 GeV/c
η range	$\lvert\eta\rvert \leq 0.63$
Impact parameter	$<$ 5 mm
z-vertex match	$<$ 5 cm
$\lvert\delta x\rvert$	$<$ min(15 cm, 60 cm/P_T)

Table 10: Identification requirements for muons from bottom and charm decays in $t\bar{t}$ events.

a match $|\delta_x| < 10$ cm for one of the two muons at the reconstruction stage. The transverse momentum distribution of muon candidates with dimuon invariant mass ($M_{\mu\mu}$) in the signal region 3.0 GeV/$c^2 < M_{\mu\mu} <$ 3.16 GeV/c^2, after subtraction of the contribution from the continuum underneath the peak, is shown in Figure 12. The rather sharp threshold at P_T = 3 GeV/c is due to the fact that most of these events were recorded with a trigger that required two tracks of P_T > 3 GeV/c as determined by the track processor.

With one muon constrained to $|\delta_x| < 10$ cm by the selection process, we study the unbiased δ_x distribution of the other muon for events in the region of the J/ψ peak; events in the sideband regions 2.92 GeV/$c^2 < M_{\mu\mu} <$ 3.00 GeV/c^2 and 3.16 GeV/$c^2 <$ $M_{\mu\mu} <$ 3.24 GeV/c^2 are used to correct for the non-muon background contamination. The δ_x distribution is well described by a Gaussian of σ = 15 cm/P_T (GeV/c) (see Figure 13), in agreement with expectations from multiple scattering. The efficiency of the matching requirements on muons is shown in Figure 14; because of statistical fluctuations in the correction procedure, the measured efficiency can be > 100%.

6 Lepton Isolation

After a heavy quark is produced and before it decays, it 'fragments' or 'hadronizes' into a hadron containing its flavor, and some other softer hadrons. Since the products of a top hadron decay have a large invariant mass, they distribute over a larger solid angle than the decay particles of a lighter quark of the same energy. The leptons from a top decay are therefore typically well separated from the acompanying bottom jet and from the decay products of the other t-quark in the event. Also due to the large mass of the top quark, additional particles (X) produced in the top-quark fragmentation, t-quark $\rightarrow$ t-meson $+X$, are expected to carry only a small fraction of initial parent-quark's momentum (see Section 10.5). Given these heavy quark fragmentation and decay properties, leptons from top decay are expected to be more isolated than those from lighter bottom or charm quark decays. Additional energy near the leptons can originate from the hadronization of gluons radiated by the initial and final state partons (gluon radiation), or from the spectator partons in the $p\bar{p}$ interaction (underlying event).

Lepton isolation cuts are used in the top analysis to help reduce backgrounds from bottom and charm production. The isolation cuts are also useful to reject 'fake' lepton backgrounds from particle misidentification, electrons from photon conversions and Dalitz decays, and muons from the decay in flight of hadrons, since these background particles originate from ordinary QCD jets and are surrounded by other activity from the jet. These cuts are described in Sections 4 and 5.

Uncertainties can be introduced in the analysis from the limited knowlege of the modeling of the top fragmentation and decays, the modeling of gluon radiation, and of the detector simulation of the isolation variables. As a check of the detector simulation, we have compared isolation distribution variables for leptons from Z^0 decays with Monte Carlo predictions (see Figure 15). The distribution of the variable E_T^{cone}, the transverse energy in the towers within a cone of R $\equiv \sqrt{(\Delta\phi)^2 + (\Delta\eta)^2}$ = 0.4, excluding the lepton energy deposition, is shown for central electrons and for central muons. For muons, we also show the distribution of P_T^{cone}, the sum of track momenta inside the cone of R=0.4. For plug electrons, the distribution of the isolation ratio $I = E_T^{cone}/E_T^e$ is shown in Figure 15. In each case, the cut value used in the dilepton analysis of Section 9 is shown for reference. The (small) energy detected in the vicinity of leptons from Z^0 decays comes mostly from the 'underlying event', or fragments from the spectator partons. The good agreement between the data and Monte Carlo in Figure 15 gives confidence in the detector simulation and the Monte Carlo modeling of the underlying event. For leptons from Z^0 decays, the efficiency of the isolation cuts exceeds 97%. Leptons from top decay are somewhat less isolated than those from Z^0 decays, as can be seen in Figure 16 which shows the distributions of the isolation variables for leptons from $t\bar{t}$ events with M_{top} = 90 GeV/c^2. For a single lepton from $t\bar{t}$, the efficiency of the isolation cuts in the dilepton analysis is 88%.

As a further check of the modeling of the energy flow around leptons, the isolation distribution of an inclusive electron sample [15], consisting predominantly of leptons from semileptonic decays of bottom quarks, has been compared with $b\bar{b}$ Monte Carlo predictions. Such a comparison is shown in Figure 17, using the variable E_T^{iso} used in the *lepton + jets* analysis. E_T^{iso} is defined as the sum of the transverse energy in calorimeter towers immediately adjacent to the electron cluster. The agreement is quite good .

7 Jets and Missing Transverse Energy

The jet reconstruction algorithm used in CDF [32] is a fixed cone algorithm. A circle of radius 0.7 in $\eta - \phi$ space is drawn about any tower with $E_T > 1$ GeV. The energies in towers with $E_T > 0.1$ GeV inside the circle are added to that of the seed tower, the energy centroid is calculated, and a new circle is formed. The process is repeated until the list of towers in the circle remains unchanged. If two clusters overlap such that one shares more than 50% of the energy, the two clusters are merged; otherwise common towers are assigned to the nearest cluster.

Because of effects of calorimeter non-linearities, gaps in the calorimeter coverage near detector boundaries, and energy leakage outside the clustering cone, the jet-energies reconstructed by the algorithm are systematically lower than the energies of the original partons. The energy degradation of reconstructed jets is a function of the E_T of the jets and, because of cracks between calorimeter modules, is also a function of the location of the jet in the calorimeter. This degradation in response varies between 20% and 40% for jets with E_T near 20 GeV. The systematic uncertainty in the jet energy scale for central jets in the E_T range 18-180 GeV is estimated to range between 13% and 5% for the lower and higher energy jets respectively.

The missing transverse energy ($\not{E}_T$) is defined to be the negative of the vector sum of transverse energy in all calorimeter towers with $|\eta| < 3.6$. The η range is restricted because the final focusing magnets of the Tevatron obscure parts of the forward hadron calorimeter. To be included in the sum, individual tower energies must exceed detector-dependent energy thresholds. These thresholds are 100 MeV in the central calorimeters, 300 MeV in the plug EM calorimeter, 800 MeV in the forward HAD calorimeter and 500 MeV in the plug HAD and forward EM calorimeters. For events with muon candidates, the $\not{E}_T$ measurement is corrected by vectorially subtracting the energy deposited in the tower traversed by the muon and then adding the P_T of the muon candidate as measured in the central tracking chamber.

The resolution on the $\not{E}_T$ measurement depends on the amount of energy in the event. For minimum bias events, the resolution for the two components $\not{E}_{T_x}$ and $\not{E}_{T_y}$ of the $\not{E}_T$ vector can be parametrized[11] as $\sigma(\not{E}_{T_{x,y}}) = 0.47\sqrt{\sum E_T}$ where $\sum E_T$ is the total transverse energy in the event. For $W + jets$ events, which have characteristics similar to top events, the $\not{E}_T$ resolution is well reproduced by the detector simulation (see Section 8).

8 The Monte Carlo

The ISAJET Monte Carlo program [30] and the full detector simulation [31] are used to determine the acceptances of our analyses to top events. After simulation, Monte Carlo events are passed through the complete offline reconstruction in the same way as the real data. Corrections are then made to account for the trigger efficiencies, and for small differences between the data and Monte Carlo lepton reconstruction efficiencies .

In the Monte Carlo, the branching ratios for the W decays in the process $t \rightarrow Wb$ are set at 1/9 for $W \rightarrow l\nu$ and 1/3 for $W \rightarrow u\bar{d}$ or $c\bar{s}$. For $b \rightarrow \mu$ and $b \rightarrow c \rightarrow \mu$ we use the following branching ratios :

$$\begin{aligned} BR(B \rightarrow \mu + X) &= 10.2\% \\ BR(D^0 \rightarrow \mu + X) &= 7.5\% \\ BR(D^+ \rightarrow \mu + X) &= 17\% , \end{aligned} \tag{1}$$

in agreement with the most recent values from the CLEO [33] and L3 experiments [34] and from the Particle Data Group (PDG) [35].

The modeling of the momentum spectrum of muons from bottom decays is important in the evaluation of the muon acceptance. The spectrum generated by the ISAJET program is in good agreement with the experimental measurement from Reference [33].

The $W + jets$ process constitutes the main background to the top search in the $lepton + jets$ channel. $W + jets$ Monte Carlo data sets are generated with the PAPAGENO[36] program, which includes the appropriate tree level matrix elements. In the Monte Carlo, the partons generated by PAPAGENO are fragmented into hadrons and an underlying event is added to the hard scattering process following the method employed by ISAJET. This program is also used to generate $t\bar{t}$ events to compare its modeling of $t\bar{t}$ production and decay with those of ISAJET.

The detector simulation includes effects such as cracks, photon conversions and detector resolution. In the simulation, the calorimeter response to hadrons with $P_T >$ 10 GeV/c is adjusted to agree with test beam data; at lower P_T the response is tuned to reproduce isolated track data collected with a minimum bias trigger.

In the $lepton + jets$ top analysis we characterize events by jet multiplicity, where we count jets above an E_T threshold which is set at 10 GeV. The understanding of the energy scale in the Monte Carlo, and more importantly, the understanding of the jet reconstruction efficiency as a function of parton E_T, has been verified by comparing with our data on direct photon production[15] . In events containing a high E_T photon recoiling against a jet, the jet is expected to balance the photon in E_T . Since the photon is very well measured in the EM calorimeter, this provides a sample of jets originating from partons of well defined energy. The results are summarized in Figure 18, where we show the probability of reconstructing a cluster of $E_T > 10$ GeV as a function of the photon E_T. Based on this study, and on similar studies of the jet E_T spectrum for events including electrons recoiling against jets [15] the uncertainty on the energy scale is estimated to be 20% for jets with E_T of 10 GeV.

The $\not{E}_T$ resolution is also well reproduced by the detector simulation. This agreement is indicated [15] in Figure 19, where the transverse mass distribution of $W + 1$ *jet* events is compared with the prediction from the PAPAGENO Monte Carlo program and the detector simulation. This distribution is sensitive to the $\not{E}_T$ resolution, and its shape is in good agreement with the Monte Carlo prediction.

9 Dilepton Search

9.1 $t\bar{t}$ Dilepton Signature

Top quarks at the Tevatron are produced mainly in pairs via the process $p\bar{p} \rightarrow t\bar{t}$ (see Section 1). With an expected semileptonic branching ratio of $\frac{1}{9}$ per lepton, the fraction of events with both top quarks decaying entirely hadronically is $\frac{36}{81}$, with a resulting multijet signature that seems extremely difficult to distinguish from large QCD multijet backgrounds. An important enhancement in the signal-to-background ratio is obtained by requiring at least one electron or muon in the final state. The case in which one top quark decays semileptonically and the other hadronically accounts for $\frac{12}{81}$ of the $t\bar{t}$ rate for a given lepton species. A search in this channel, $lepton + jets$, in which the presence of a b quark from the top decay is detected via the decay $b \rightarrow \mu$, is presented in a subsequent section of this report.

In this section, we present results from a search for high-P_T dilepton final states of the processes $t\bar{t} \rightarrow e\mu + X$, $ee + X$, and $\mu\mu + X$. The analysis is an extension of the previous $e\mu$ analysis of Reference [14], where we now include the channels ee and $\mu\mu$. The search has also been extended to include electrons in the plug calorimeter.

The simultaneous decay of each of the top quarks into $l\nu b$ ($l = e$ or μ) has branching ratios of $\frac{2}{81}$ for $e\mu$, $\frac{1}{81}$ for ee, and $\frac{1}{81}$ for $\mu\mu$. These double semileptonic decays of the $t\bar{t}$ pair, with an overall branching fraction of $\frac{4}{81}$, constitute the majority of the dilepton signal. Small contributions from sequential decays of a daughter b or c quark or a τ lepton are also considered.

To separate the $t\bar{t}$ dilepton events from backgrounds from semileptonic decays in $b\bar{b}$ events, and from charged hadrons that may mimic leptons, the two final state leptons are required to be isolated and to have high transverse momenta. These requirements provide a very clean $t\bar{t}$ signal in the $e\mu$ dilepton channel, where a small remaining background comes predominantly from $Z^0 \rightarrow \tau\tau$ events with final states containing an electron and a muon. The ee and $\mu\mu$ channels have important additional lepton pair backgrounds from the Drell-Yan mechanism. In the Drell-Yan process, a quark-antiquark pair annihilate to produce a virtual photon or a Z^0 which decays into lepton pairs. Simple kinematical and event topology cuts (dilepton invariant mass, dilepton opening angle, and missing transverse energy) are employed to supress these backgrounds and are discussed further in this section.

9.2 Event Selection

The events selected for the dilepton analysis are classified according to the regions where the leptons are detected. We use the notation CE for electrons detected in the central calorimeter and PE for those detected in the plug calorimeter. Muons detected in the chambers of the central muon detector are denoted by MU. Muons directed outside the central muon chambers, which are detected as tracks in the central tracking chamber having minimum ionizing energy deposition in the central calorimeter, are denoted by MI. The different electron and muon detection fiducial regions are illustrated in Fig. 20. There are 10 possible classes of dilepton events : CE-CE, CE-MU, CE-MI, CE-PE, MU-MU, MU-MI, MU-PE, PE-MI, PE-PE and MI-MI. Since leptons from top decay are emitted preferentially in the central rapidity region, the PE-PE category, having both electrons in the plug region, has less than 2% of the total dilepton acceptance. Since muons outside the muon chamber coverage do not trigger the apparatus, the MI-MI category also has negligible contribution. We will consider only the first 8 categories.

The electron and muon identification variables used in the dilepton analysis have been described in Sections 4 and 5. A transverse momentum cut on the leptons is chosen to preserve a large portion of the top signal, while rejecting much of the backgrounds from $b\bar{b}$ decays and from particle misidentification. These backgrounds have lepton transverse momentum spectra that fall much faster than for the case of $t\bar{t}$. The predicted number of $e\mu$ events detected with both leptons above a common threshold P_T^{min}, is shown in Fig. 21 as a function of this threshold, for Monte Carlo $b\bar{b}$ and $t\bar{t}$ events. The significant difference between the lepton spectra of signal and background motivates a choice of transverse momentum threshold of 15 GeV/c on both leptons. Events in the signal region are thus required to have both leptons above $P_T^{min} = 15$ GeV/c.

All categories of dilepton events, with one exception, can be triggered by one or both of the central electron and muon triggers, which are highly efficient at the 15 GeV/c threshold. For events in the PE-MI category, because of triggering considerations, we have raised the threshold on the plug electron to $E_T^e = 30$ GeV. At this threshold, the plug calorimeter trigger, needed to collect PE-MI events, is 50% efficient (see Section 3).

Further improvement in the signal-to-background ratio is achieved by placing isolation cuts on the leptons. These cuts are discussed in Section 6.

After the lepton identification, isolation, and transverse momentum cuts, 4 $e\mu$, 271 ee, and 112 $\mu\mu$ dilepton events are found in the data.

9.3 Dilepton Data and Final Event Topology Cuts

After the dilepton event selection cuts, additional kinematical and event topology cuts are used to reduce backgrounds. The event topology cuts are summarized in Table 11. A back-to-back cut requiring $\Delta\phi_{ll} < 160°$, where $\Delta\phi_{ll}$ is the dilepton azimuthal opening angle, is placed to supress a small background in the $e\mu$ channel expected from $Z^0 \to \tau\tau$, $b\bar{b}$ and particle misidentification. Large backgrounds from Z^0 and Drell-Yan events in the dielectron and dimuon channels, are also reduced by the back-to-back cut. Added rejection is obtained by applying a dilepton invariant mass window cut around the Z^0 peak and a missing transverse energy cut. We remove ee and $\mu\mu$ events with dilepton invariant mass in the range $75 < M_{ll} < 105$ GeV/c^2 or with missing transverse energy $\not{E}_T < 20$ GeV. The intermediate γ or Z^0 in Drell-Yan events is produced mainly at low transverse momentum, and therefore gives rise to dileptons with nearly balancing momenta (back-to-back) in the transverse plane . In addition, since there are no neutrinos in these events, the missing transverse energy tends to be small, being due only to fluctuations in the calorimeter measurement. In contrast, the opening angle and missing energy cuts preserve a large part of the top signal. In $t\bar{t}$ events, the two t-quarks are emitted back-to-back in the transverse plane, with only small imbalances due to gluon radiation of the incoming partons or of the outgoing quarks. Since the directions of the products of the decay of heavy top quarks are not strongly correlated with the top direction of flight, most of the dileptons from $t\bar{t}$ survive the $\Delta\phi_{ll}$ cut. Also, due to the presence of two neutrinos in the final state, $t\bar{t}$ dilepton events will likely satisfy the $\not{E}_T$ requirement. For $M_{top} = 90$ GeV/c^2 the $\Delta\phi_{ll}$ and $\not{E}_T$ cuts have a combined efficiency of $\sim 80\%$.

9.3.1 $e\mu$

The lepton transverse momenta for the 4 electron-muon events are shown in Fig. 22a. The transverse momentum of the least energetic lepton for each event is plotted in Fig. 22b against the dilepton azimuthal opening angle. Before the final back-to-back cut we expect 4.7 $e\mu$ events from backgrounds, mostly from $Z^0 \rightarrow \tau\tau$, $b\bar{b}$, and particle misidentification (see Section 9.6). The back-to-back cut is expected to reduce backgrounds by a factor of four, while preserving 84% of the $t\bar{t}$ signal for $M_{top} = 90$ GeV/c^2. Figures 23 and 24 show the corresponding Monte Carlo distributions for $t\bar{t}$ and for $Z^0 \rightarrow \tau\tau$ events, respectively.

After the final back-to-back cut only one candidate $e\mu$ event, the one with the highest transverse momentum leptons, is left in the data. The three events rejected have an electron in the plug calorimeter and therefore had not been found in the previous $e\mu$ analysis of Reference [14]. They also have small $\not{E}_T$, and are consistent with being background events.

The event in the signal region is the same one found in the previous analysis [14]. It has an isolated central electron with E_T^e of 31.7 GeV and an isolated opposite sign muon (MI) with P_T^μ of 42.5 GeV/c with a dilepton azimuthal opening angle of 137°. Other characteristics of the event include the presence of a second muon candidate with transverse momentum of 9.9 GeV/c in the forward muon detector, and two small calorimeter clusters with observed transverse energy depositions of 14 GeV and 5 GeV. Figures 25 show a tracking chamber display and a calorimeter display for the candidate. Some properties of the event are summarized in Table 12. The calculation of backgrounds for the dilepton channels is discussed in Section 9.6. Here we note that for the $e\mu$ channel we expect a total of 1.2 ± 0.5 background events after the back-to-back cut. The most important backgrounds are : 0.3 ± 0.2 event from $b\bar{b}$, 0.2 ± 0.1 event from $Z^0 \rightarrow \tau\tau$, 0.12 ± 0.01 from WW and 0.6 ± 0.4 from particle misidentification. All these backgrounds, except for WW, have rapidly falling lepton spectra and concentrate near the 15 GeV/c^2 lepton P_T threshold. Based on this information alone, the event in the signal region could be interpreted as a WW event. The dilepton kinematics of WW diboson events is very similar to that of $t\bar{t}$ when the top quark mass is above the W mass. However, differences between these two types of events arise from the presence of two b-quarks which can give extra jets or leptons in a $t\bar{t}$ event. Considering that the $e\mu$ event has some jet activity, and more notoriously, that is has a second muon in the forward region, the interpretation as a WW diboson event is less likely. We point out too, that muons from b decay in $t\bar{t}$ events tend to be produced in the central region, and a muon in the forward region is not typical of such events.

9.3.2 $ee, \mu\mu$

The dilepton invariant mass (M_{ll}) distribution is shown in Fig. 26 for the 271 dielectron events, 112 dimuon events, and for Monte Carlo $t\bar{t} \rightarrow ll + X$ events with $M_{top} = 90$ GeV/c^2. Monte Carlo Drell-Yan and Z^0 predictions which are also shown in this figure are in good agreement with the ee and $\mu\mu$ data. Measurements of the Drell-Yan and Z^0 cross section times branching ratio into dielectrons have been reported in earlier publications by CDF [38, 8]. Removal of the majority of Z^0 backgrounds is achieved by rejecting events with $75 < M_{ll} < 105$ GeV/c^2. The data sample is reduced to 50 ee and 15 $\mu\mu$ events with this requirement.

The distribution in the $\not{E}_T - \Delta\phi_{ll}$ plane is shown in Fig. 27 for $t\bar{t} \rightarrow ll + X$

Monte Carlo events with dilepton mass outside the Z^0 region. The corresponding distributions for CDF dielectron and dimuon data are shown in Fig. 28. After imposing the dilepton azimuthal opening angle and the missing transverse energy cuts, no dielectron or dimuon events are left in the data.

9.4 Efficiencies for $t\bar{t} \rightarrow ll + X$

We now describe the determination of the efficiencies that relate the observed cross section for dilepton events in the signal region to the total $t\bar{t}$ production cross section :

$$\sigma_{obs} = \sigma_{t\bar{t}} \cdot B_T \cdot \varepsilon_{Total} \ . \tag{2}$$

In this expression, the total efficiency for dileptons, ε_{Total}, is normalized to $B_T = \frac{4}{81}$, the double semileptonic branching fraction into $e\mu, ee,$ or $\mu\mu$. It can be decomposed into several parts and written as :

$$\varepsilon_{Total} = \sum_{Event\ class} \varepsilon_{Geom \cdot P_T} \cdot \varepsilon_{Trigger} \cdot \varepsilon_{Isol} \cdot \varepsilon_{ID} \cdot \varepsilon_{Event} \ , \tag{3}$$

where the sum extends over the 8 dilepton event classes under consideration.

The acceptance due to geometrical and transverse momentum cuts, $\varepsilon_{Geom \cdot P_T}$, is the fraction of $t\bar{t}$ events with dileptons inside the fiducial region and passing the P_T cuts. This acceptance is determined by using the ISAJET Monte Carlo[30] event generator and the geometry of the CDF detector.

As mentioned in Section 9.1, contributions to the signal in addition to the direct semi-leptonic decay of the $t\bar{t}$ pair, such as $t \rightarrow b, c \rightarrow l$ and $t \rightarrow \tau \rightarrow l$, are also counted. Table 13 shows the contributions for various top-quark masses. Double semileptonic decays account for about 80% of the signal. The next most abundant source for $M_{top} \simeq 90$ GeV/c^2 is from events with at least one lepton from the decay of a τ daughter of one top quark.

The trigger efficiency $\varepsilon_{Trigger}$ for each dilepton class is determined using the efficiencies measured for the single lepton triggers (Section 3). An additional correction is applied on the efficiency of the central muon trigger which was not operational during the earliest 15% of data taking. For dilepton events in categories that can be collected with two of the lepton triggers, the trigger efficiency is computed as is $1 - f_1 \cdot f_2$, where f_1 and f_2 are the separate probabilities for failing the first and second lepton triggers, respectively.

The the efficiency of the lepton isolation cuts, ε_{Isol}, is determined using ISAJET Monte Carlo events with full detector simulation. The efficiency of the identification cuts on isolated dileptons, ε_{ID}, is determined from $Z^0 \rightarrow e^+e^-$ and $Z^0 \rightarrow \mu^+\mu^-$ events. Finally, ε_{Event} is the fraction of Monte Carlo events passing all previous cuts which also satisfy the event topology cuts. The various efficiency terms are listed for each of the dilepton categories in Table 14, for $M_{top} = 90$ GeV/c^2. The total dilepton efficiency at this mass is $\varepsilon_{Total} = (16.2 \pm 1.8)$ %, corresponding to $0.162 \times \frac{4}{81} = 0.80\%$ of the $t\bar{t}$ cross section. Uncertainties in the top dilepton efficiency are discussed in the next section. The (small) top quark mass dependence of the efficiencies is illustrated in Fig. 29.

9.5 Uncertainties in the Dilepton Efficiency

The total efficiency for detecting dileptons from $t\bar{t}$, ε_{Total}, is affected by systematic uncertainties associated with each of the factors on the right hand side of Equation 3. We estimate a 4% uncertainty in the acceptance due to geometrical and P_T cuts

$\varepsilon_{Geom \cdot P_T}$. This was the variation observed in this acceptance when the PAPAGENO Monte Carlo calculation was used instead of ISAJET. The uncertainty due to trigger efficiency $\varepsilon_{Trigger}$ for dilepton events is taken as 2%, which is an upper bound from propagating the uncertainties in the measurements of the single lepton triggers (see Section 3).

The uncertainty in the efficiency of the isolation cuts is 4% per lepton, resulting in an 8% uncertainty in ε_{Isol}. For a single lepton from $t\bar{t}$, uncertainties in the isolation efficiency originate from uncertainties in the Monte Carlo gluon radiation model (3%), in the top fragmentation model (1%), and from the simulation of the calorimeter (2%).

The uncertainty in the efficiency for detecting isolated dileptons, ε_{ID} is 5% and results from propagating the uncertainty in the measurement of the efficiency of the identification cuts on single leptons from Z^0 decays (see Sections 4 and 5). Finally, we assign a systematic uncertainty of 2% on the efficiency of the final event topology cuts. This uncertainty in ε_{Event} reflects the overall change in efficiency caused by varying the $\not{E}_T$ cut by 20%, to represent the uncertainty in the calorimeter (jet) energy scale.

Adding these uncertainties in quadrature together with a 3% uncertainty due to Monte Carlo statistics, gives a total uncertainty of 11% on ε_{Total}. An additional 6.8% uncertainty in the measurement of integrated luminosity must added in quadrature to the uncertainty in ε_{total} to obtain the uncertainty in the number of $t\bar{t}$ dilepton events expected in the data sample.

9.6 Backgrounds

The $t\bar{t}$ dilepton signature can be mimicked by dilepton final states of Drell-Yan events ($\gamma/Z^0 \rightarrow ee, \mu\mu$ or $\gamma/Z^0 \rightarrow \tau\tau \rightarrow e\mu, ee, \mu\mu$), diboson events ($WW$ or $WZ \rightarrow$

$e\mu, ee, \mu\mu$), or heavy flavor events ($b\bar{b}$ or $c\bar{c} \rightarrow e\mu, ee, \mu\mu$). Events from ordinary QCD jet or $W + jet$ processes, with at least one misidentified lepton, conversion electron, or muon from hadronic decay-in-flight can also simulate the $t\bar{t}$ signature and are referred to as 'fake dilepton' backgrounds. In what follows we present estimates of the number of the various types of background events expected in the dilepton data sample.

The detection efficiency for the Drell-Yan, diboson and heavy flavor backgrounds, is decomposed into various terms, in the same way as was done for the $t\bar{t}$ signal, which is described in detail in Section 9.4. As before, the ISAJET Monte Carlo event generator was used together with a detector simulation to determine the geometrical and kinematical acceptance, the efficiency of the lepton isolation cuts, and the efficiency of the event topology (background rejection) cuts. Also as before, we used lepton identification efficiencies measured for isolated leptons from Z^0 and W events, and trigger efficiencies measured in data collected with independent triggers. The resulting number of background events expected in the data sample, both before and after the application of the event topology cuts, is shown in Table 15. The cross sections used to predict the background yields of Table 15 are those from ISAJET.

The overall efficiency of the event topology cuts is shown in Table 16 along with the separate efficiencies of the invariant mass, back-to-back, and missing E_T cuts. We note that in order for Drell-Yan events to pass these cuts, they must have an intermediate γ or Z^0 produced at high P_T. Such events will have dileptons which are not back-to-back, and jets. The jets can give rise to significant missing transverse energy when a large fluctuation in the calorimeter measurement occurs. More than 85% of the Monte Carlo ee and $\mu\mu$ Drell-Yan events passing the event topology cuts have $P_T(\gamma \text{ or } Z^0) > 50$ GeV/c. Only a small fraction (2%) of Drell-Yan events are produced at such high

P_T. Since the modeling of the tail of the P_T distribution is important, it is desirable to become independent of of the Monte Carlo prediction in this respect. Therefore, the shape of the P_T distribution measured for Z^0 events [39] was incorporated into the background estimation. The Drell-Yan event topology efficiencies were determined as a function of $P_T(\gamma$ or $Z^0)$ by using Monte Carlo, and were then convoluted with a parameterization of the measured P_T distribution [39]. Results for the event topology cut efficiencies and background are included in Tables 15 and 16.

The 'fake dilepton' backgrounds were calculated separately for each of the 8 dilepton categories using a common method. For concreteness, we now consider the $e\mu$ case. The number of $e\mu$ events with a fake muon can be estimated by allowing fake muons into the sample by removing the calorimeter minimum ionizing cut. The fake muon contamination in the final sample can be calculated from the number of extra events accepted without the minimum ionizing cut, combined with the probability for an ordinary isolated particle to satisfy the minimum ionizing cut. The 'fake probability' per isolated track is obtained from a background sample of events collected with a jet trigger with an E_T threshold for the jet of 20 GeV. The process is repeated for the electron side, i.e. the fake electron contamination in the final sample is derived from the number of events added to the sample by relaxing the electron identification cuts on EM clusters, and from a fake probablity for an EM cluster of the jet trigger background sample to pass the strict electron identification criteria.

Let N be the number of events in the sample (before topology cuts) for a given dilepton category and N' the total number of events accepted when the lepton identification requirements on one lepton are relaxed. The number of real and fake events

$(N_R,\ N_F)$ in the sample can be solved from the following equations :

$$N = N_R + N_F \tag{4}$$

$$N_R = P_R N'_R \tag{5}$$

$$N_F = P_F N'_F \tag{6}$$

$$N' = N'_R + N'_F\ , \tag{7}$$

where N'_R and N'_F are the number of real and fake events, respectively, in the sample with the relaxed cuts. P_F is the fake lepton probability per isolated track as described earlier; P_R is the efficiency for a lepton passing the relaxed cuts to also pass the tight cuts and is determined using leptons from Z^0 decays. Table 17 shows the values of P_R and P_F for the various lepton classes. To obtain the background expected after topology cuts, we scale N_F by the fraction of the events (added to the sample when the lepton identification requirements are loosened) that pass the topology cuts. Results for the number of fake events expected before and after topology cuts are presented in Table 18.

9.7 Summary of the Dilepton Analysis

We have searched for $t\bar{t} \to e\mu, ee$ or $\mu\mu + X$ in data containing two high-P_T leptons. To suppress backgrounds coming predominantly from Drell-Yan events, we applied cuts on M_{ll}, $\Delta\phi_{ll}$ and $\not{E}_T$. The dilepton selection has an overall efficiency of 0.80 ± 0.09 % for all produced $t\bar{t}$ events with $M_{top} = 90$ GeV/c^2. A total of 7.9 (4.9, 3.0) $t\bar{t}$ dilepton events are expected in the data for $M_{top} = 80$ (90, 100) GeV/c^2. No ee or $\mu\mu$ candidates are left in the data after all cuts are applied. One $e\mu$ candidate event is found in the $t\bar{t}$ signal region. Although some characteristics of the candidate (especially the presence of a second muon in the forward region) are atypical of the main background processes, it is not possible to give a firm conclusion about the identity of this event.

Based on the observation of one event in the signal region, a limit on $t\bar{t}$ production is presented in Section 11. A combined limit obtained by using the results of both the dilepton and $b \rightarrow \mu$ (Section 10) analyses is also presented in Section 11.

Dilepton Channel	Topology Cuts
$e\mu$	$\Delta\phi_{e\mu} < 160°$
ee, $\mu\mu$	reject $75 < M_{ll} < 105$ GeV/c^2 $\Delta\phi_{ll} < 160°$ $\not{E}_T > 20$ GeV

Table 11: Dilepton topology cuts.

Run 19250, Event 20435.

	Charge	P_T [GeV/c]	η	ϕ [degrees]
Central Electron	+	31.7	-0.81	132
Central Muon	−	42.5	-0.80	269
Forward Muon	+	9.9	-2.0	98
Jet 1		14	1.1	341
Jet 2		5	-2.8	88

Table 12: Characteristics of the top candidate event. Observed calorimeter E_T is used in the P_T column for the electron and jet clusters.

	M_{top} [GeV/c^2]			
	70	80	90	100
i) $t \rightarrow l$	0.80	0.78	0.82	0.74
ii) $\tau \rightarrow l$	0.08	0.09	0.12	0.11
iii) $b, c \rightarrow l$	0.12	0.13	0.06	0.15

Table 13: The fractions of $t\bar{t} \rightarrow ll + X$ having: i) both leptons coming directly from the top decay; ii) at least one lepton coming from the decay of a τ; and iii) leptons coming from the decays of a b or c quark.

Event class	$\varepsilon_{Geom \cdot P_T}$ %	$\varepsilon_{Trigger}$ %	ε_{Isol} %	ε_{ID} %	ε_{Event} %	ε_{Total} %
CE-CE	6.7	100	77	89	61	2.9
CE-MU	9.2	100	71	84	85	4.6
CE-MI	7.5	98	74	84	83	3.8
CE-PE	3.8	99	76	67	53	1.0
MU-MU	3.1	85	65	96	70	1.2
MU-MI	4.6	78	68	96	58	1.4
MU-PE	2.5	81	70	77	91	1.1
PE-MI	1.0	85	74	77	90	0.42
Total	38.3	94.4	72.6	84.3	73.3	16.2 ± 1.8

Table 14: Dilepton detection efficiencies for $M_{top} = 90$ GeV/c^2. The total dilepton efficiency at this mass is $\varepsilon_{Total} = (16.2 \pm 1.8)$ %.

		Number of events in 4.1 pb^{-1}	
		before topology cuts	after topology cuts
$e\mu$	$Z \to \tau\tau$	1.4	0.2 ± 0.1
	WW	0.15	0.12 ± 0.01
	WZ	0.03	0.022 ± 0.004
	$b\bar{b}$	1.5	0.3 ± 0.2
	Fake	1.6	0.6 ± 0.4
Total Bg. Expected		4.7	1.2 ± 0.5
CDF Data		4	1
$ee, \mu\mu$	$Z \to \tau\tau$	1.8	0.06 ± 0.03
	WW	0.12	0.071 ± 0.007
	WZ	0.083	0.007 ± 0.001
	$\gamma/Z \to ee, \mu\mu$	342	0.9 ± 0.7
	$b\bar{b}$	3.9	< 0.01
	Fake	3.7	0.4 ± 0.1
Total Bg. Expected		352	1.5 ± 0.8
CDF Data		383	0

Table 15: Dilepton yields in 4.1 pb^{-1}.

		ε_{Mass}	$\varepsilon_{\Delta\phi}$	$\varepsilon_{\not{E}_T}$	ε_{Event}
		%	%	%	%
$e\mu$	$Z \rightarrow \tau\tau$	-	13	-	13
	WW	-	79	-	79
	WZ	-	75	-	75
$ee, \mu\mu$	$Z \rightarrow \tau\tau$	97	10	8.5	3.1
	WW	83	77	77	61
	WZ	12	92	62	8.2
	$\gamma/Z \rightarrow ee, \mu\mu$	14	16	2.1	0.27

Table 16: Efficiencies of the event topology cuts on the various background processes. Only the back-to-back topology cut is applied in the $e\mu$ channel.

Lepton Type	P_R	P_F
CE (tight)	0.85 ± 0.03	0.004 ± 0.002
CE (loose)	0.96 ± 0.01	0.059 ± 0.007
PE	0.79 ± 0.04	0.09 ± 0.01
MU	0.98 ± 0.01	0.11 ± 0.04
MI	0.98 ± 0.01	0.010 ± 0.004

Table 17: The probabilities for passing the identification cuts for real leptons (P_R), and for isolated EM clusters or tracks (P_F).

Dilepton Class	Before Topology Cuts	After Topology Cuts
CEMU+CEMI	0.9 ± 0.4	0.3 ± 0.2
PEMU+PEMI	0.7 ± 0.4	0.3 ± 0.3
Total $e\mu$	1.6 ± 0.6	0.6 ± 0.4
CECE	1.2 ± 0.2	0.09 ± 0.04
CEPE	2.0 ± 0.8	0.10 ± 0.05
MUMU+MUMI	0.5 ± 0.3	0.10 ± 0.05
Total $ee + \mu\mu$	3.7 ± 0.9	0.4 ± 0.1

Table 18: The number of fake dilepton backgrounds expected in 4.1 pb^{-1}.

10 Tagging b quarks in top semileptonic decays

10.1 Introduction

The dilepton decay modes of the $t\bar{t}$ pair discussed in Section 9 have lower branching ratios than those involving hadrons. While the purely hadronic decay modes of the pair are difficult to distinguish from more copious QCD backgrounds, the modes in which one of the top quarks decays semileptonically into $be\nu$ or $b\mu\nu$ and the other top quark decays into hadrons can be used to look for top. In previous publications [15] we have reported on a search for top production in events with high-E_T electrons, missing transverse energy and and at least two jets, in which we established a 95% C.L. lower limit on the mass of the top quark of 77 GeV/c^2. The most important background to the search is from high P_T W events produced in association with jets ($p\bar{p} \rightarrow W + 2\ jets,\ W \rightarrow e\nu$). The method used to discriminate against this background is based on the transverse mass distribution of the electron and the $\not{E}_T$ (neutrino) and breaks down for top masses at or above the W mass (M_W), when the top quarks decay into real W bosons. Therefore, to extend the sensitivity to top masses higher than M_W, a different way of rejecting the background is needed.

The process $t\bar{t} \rightarrow e\nu b\ q\bar{q}\bar{b}$ differs from $W + 2\ jets$ production in that there are potentially four jets in the final state and, if $M_{top} \geq M_W$, two of the jets come from a hadronic W decay. The previous analysis required detection of a high E_T ($E_T > 20$ GeV) electron, $\not{E}_T > 20$ GeV and at least two jets of $E_T > 10$ GeV. It seems natural to try to extend the analysis by requiring additional jet activity in the event and/or requiring that two of the jets form an invariant mass equal, within the resolution, to

M_W. However, for top masses slightly above the W mass, the kinetic energy liberated in the top decay is small, so that the P_T of the b quarks in the laboratory frame is small (see Figure 9) and the probability for reconstructing the b-quark as a separate jet is not large (see Figure 18, where we show the probability as a function of P_T for a parton to be reconstructed as a jet of $E_T > 10$ GeV in the detector). The rates of expected top events with three jets are degraded significantly enough that the background from $W + 3$ *jets* remains very important. Furthermore, the extraction of a top signal from the invariant mass distribution of jets is also problematic because of the large uncertainties in the jet energy scale, the poor di-jet mass resolution, and the non-negligible background from W + *jets*. For these reasons we have chosen a different approach, namely to tag the bottom quarks in top events through their semileptonic decay into muons ($b \rightarrow \mu$ or $b \rightarrow c \rightarrow \mu$; see Figure 30). We search for low transverse momentum muons in the *lepton* + *jets* samples, where the high-P_T lepton is either a central electron or central muon.

10.2 *Lepton* + *jets* Event Selection

The selection of the e + *jets* events is identical to that of the previous analysis[15], and will only be summarized here. We select events with one isolated central electron with $E_T > 20$ GeV with the requirements described in Section 4 and with $\not{E}_T > 20$ GeV. Events with an additional electromagnetic cluster such that the invariant mass between this cluster and the electron candidate is above 70 GeV/c^2 are tagged as possible Z candidates and removed from the sample. Finally, we require that there be at least two jets with E_T >10 GeV and $|\eta| < 2$, where the pseudorapidity is determined from the center of the detector rather than the event vertex. This requirement ensures that the jets are contained in the central or plug calorimeters.

There are 104 events satisfying these criteria. Their transverse mass distribution is shown in Figure 31 [15] , together with a prediction for the $W + 2$ *jets* process from the PAPAGENO Monte Carlo, including full detector simulation. The agreement in the transverse mass shape between the data and the $W + 2$ *jets* Monte Carlo prediction is good. Events from b or c semileptonic decays, misidentified hadrons and residual photon conversions are expected to concentrate in the lower transverse mass region. By comparing the rates of isolated and non-isolated electrons passing all the cuts except isolation, we estimate the contribution of this class of events to the data sample to be $\simeq 12\%$.

The $\mu +$ *jets* selection mirrors the $e +$ *jets* selection : we require an isolated, high transverse momentum (P_T>20 GeV/c) muon (see Section 5), $\not{E}_T > 20$ GeV and at least two jets with E_T >10 GeV and $|\eta| < 2$. Events with an additional muon candidate such that the invariant mass of the two muons is within 20 GeV/c^2 of the Z mass are rejected. A total of 91 events pass these selection criteria.

The transverse mass of the $\mu +$ *jets* events is displayed in Figure 32. Just as in the $e +$ *jets* case, there is a clear Jacobian peak near the W mass, as expected from $W \rightarrow \mu\nu$ decays. Because of the limited acceptance of the muon chambers, it is expected that a small number of $Z +$ *jets* events remain in the sample. The background from misidentified hadrons and muons from bottom and charm decays would appear preferentially at low transverse mass. From the shape of the transverse mass distribution, and from a comparison of the relative rates of $\mu +$ *jets* and $e +$ *jets* events, the non-W/Z background in the $\mu +$ *jets* sample is estimated to be less than

20% [37].

10.3 Searching for Muons from Bottom Decays

To separate a possible top signal from the $W + jets$ background we perform a search in the 104 electron and 91 muon events for additional muon candidates from decays of the b or c quarks produced in top events. The selection requirements for these muons, which are expected to have a soft P_T spectrum (see Figure 10), are described in Section 5.2. The muon acceptance extends down to transverse momenta of approximately 1.6 GeV/c. Muons of lower momentum are stopped in the calorimeter without reaching the muon chambers. However, because of uncertainties in the detection efficiency of the lowest momentum muons, a lower transverse momentum cutoff of 2 GeV/c is imposed in the search. Furthermore, the additional muon is required to have transverse momentum below 15 GeV/c, to avoid overlap in acceptance with the dilepton search described in the previous section.

If the top quark mass is in the vicinity of the W mass, the two most energetic jets in top events are expected to originate mostly from hadronic W decays ($t \to Wb, W \to q\bar{q}$) and very rarely from the hadronization of the b-quarks. Therefore muons from bottom decays tend to be separated from the two highest-E_T jets. In order to minimize the background to the muon signal from decays-in-flight and hadron-shower leakage into the muon chambers in $W + jets$ events, the muon candidates are required to be well separated in the detector from the two highest E_T jets, where the track density and therefore the probability of reconstructing a fake muon is highest. We eliminate muon candidates within cones of radius $\Delta R = \sqrt{\Delta\phi^2 + \Delta\eta^2}$

= 0.5 centered around each of the two most energetic jets. The size of the cone has been chosen from studies of muon candidates in a sample of QCD jet events of $E_T >$ 10 GeV (see Figure 33; the majority of these muon candidates are fake muons; the contribution from prompt muons is negligible). This requirement reduces the acceptance for top events by approximately 25%.

The results of the search for additional muons of $2 < P_T < 15$ GeV/c in the 195 $lepton + jets$ events are displayed in Figure 34, which shows the η-ϕ distance between the μ candidates and the nearest of the two most energetic jets in the event. There are no candidate muons in the signal region, $\Delta R > 0.5$.

The expected background rate from shower leakage and decays-in-flight of kaons and pions in $W + jets$ events can be estimated from the same sample of QCD jet events described above. From these events we determine the probability, as a function of P_T, for a track pointing to the muon chambers to satisfy the very loose muon requirements (see Figure 35). We determine this probability separately for tracks inside a jet and for tracks outside a jet. We can then convolute these probabilities with the P_T spectra of tracks inside and outside the jets in the 195 $lepton + jets$ events (see Figure 36). In this manner we predict 7.7 background muon candidates of $P_T > 2$ GeV/c with $\Delta R < 0.5$; we see 9. The expected background rate in the signal region $\Delta R > 0.5$ is 0.9 events.

10.4 Acceptance Calculation

The acceptance for top events is determined from the ISAJET Monte Carlo and the detector simulation, as described in Section 8. In the acceptance calculation we include contributions from decay modes different from $t\bar{t} \rightarrow q\bar{q}b\, l\nu\bar{b}$, ($l = e$ or μ),

Decay mode of $t\bar{t}$	Acceptance contribution
(1) $q\bar{q}b \quad l\nu\bar{b}$	$\simeq 79\%$
(2) $e\nu b \quad l\nu\bar{b}$	$\simeq 8\%$
(3) $q\bar{q}b \quad \tau\nu\bar{b}, \quad \tau \rightarrow l$	$\simeq 5\%$
(4) $\tau\nu b \quad l\nu\bar{b}$	$\simeq 4\%$
(5) $\mu\nu b \quad l\nu\bar{b}$	$\simeq 2\%$
(6) $\tau\nu b \quad l\nu\bar{b}, \quad \tau \rightarrow \mu$	$\simeq 2\%$

Table 19: Decay modes of the $t\bar{t}$ pair and their relative contributions to the acceptance in the *lepton + jets* channel with one additional muon. The symbol l denotes the high P_T electron or muon. In modes (1)-(5) the additional muon originates from the decay of one of the b-quarks in the event. In mode (6) the additional muon is from the decay $\tau \rightarrow \mu$.

that are expected to contribute events in the signal region (see Table 19). These events increase the acceptance by approximately 20 %.

The relative contributions to the muon signal in the Monte Carlo from $t \rightarrow b \rightarrow \mu$ and $t \rightarrow b \rightarrow c \rightarrow \mu$ are approximately 70 and 30 %. A small ($\simeq 2\%$) expected contribution from $t \rightarrow b \rightarrow \tau \rightarrow \mu$ is included in the acceptance calculation. The ISAJET $t\bar{t}$ Monte Carlo also produces muons at a small rate through initial state gluon radiation, $p\bar{p} \rightarrow t\bar{t}\ g$, $g \rightarrow c\bar{c}$ or $g \rightarrow b\bar{b}$ followed by $c \rightarrow \mu$ or $b \rightarrow \mu$. The contribution from this class of events is uncertain and therefore is ignored in the acceptance calculation. Muons from misidentified hadrons in $t\bar{t}$ events are also not included in the acceptance calculation. The overall acceptance to top events of this analysis is shown in Table 20.

M_{Top}	$A_{t\bar{t}}$	f_μ
80	$\frac{24}{81}(0.161 \pm 0.015)$	0.042 ± 0.003
90	$\frac{24}{81}(0.195 \pm 0.019)$	0.045 ± 0.003
100	$\frac{24}{81}(0.222 \pm 0.021)$	0.044 ± 0.003

Table 20: $A_{t\bar{t}}$ is the acceptance to top events of the combined $e + jets$ and $\mu + jets$ selections. 24/81 is the sum of the two branching ratios for the $e + jets$ and $\mu + jets$ channels. f_μ represents the fraction of $lepton + jets$ events where we would expect to detect at least one additional muon from bottom or charm decays with $\Delta R > 0.5$.

10.5 Acceptance Uncertainties

There are a number of uncertainties in the evaluation of the acceptance of this analysis to $t\bar{t}$ events. The branching ratios for $b \to \mu$ and $b \to c \to \mu$ enter directly in the calculation, so any uncertainties in their values is reflected in an uncertainty in the acceptance. As discussed in Section 8, in the Monte Carlo calculation we use branching ratios compatible with values from the CLEO experiment and the Particle Data Group. The uncertainties on the CLEO branching ratio measurements are 4 % and 7 % for $b \to \mu$ and $b \to c \to \mu$ respectively. Given the relative contributions to the expected signal from direct and sequential decays (which are given in the previous Section), these uncertainties result in a 5 % uncertainty in the acceptance.

The acceptance is also sensitive to details of the bottom quark fragmentation. This is because the efficiency of the requirement P_T> 2 GeV/c on muons from b-decays depends on the fraction of the b-quark momentum taken up by the b-hadron after fragmentation. ISAJET uses the Peterson fragmentation model [40] to turn

b-quarks into b-hadrons :

$$D_Q^H(z) \;=\; \frac{N}{z[1-\frac{1}{z}-\frac{\epsilon}{1-z}]^2} \tag{8}$$

where $D_Q^H(z)$ is the probability that a quark Q will form a hadron H with momentum fraction $z = \frac{(E+p_L)_{Hadron}}{(E+p_L)_{Quark}}$, E is the energy, p_L is the longitudinal momentum, and N is a normalization constant. This model has been used to describe b and c fragmentation properties in e^+e^- experiments. For bottom quarks the measured value of ϵ is $\epsilon = 0.006 \pm 0.003$, corresponding to an average value $<z>= 0.83 \pm 0.03$ [41]. A larger (smaller) value of ϵ corresponds to a 'harder' ('softer') fragmentation.

ISAJET employs an independent fragmentation model to turn partons into hadrons. The model does not rigorously conserve energy. Energy conservation is imposed at the end of the event generation by appropriate rescaling of all three-momenta of the final state particles. This rescaling distorts the input $D_Q^H(z)$ function. An adjustable bottom quark fragmentation parameter in ISAJET is chosen in such a way that the average value of z in Monte Carlo $b\bar{b}$ events after rescaling agrees with measurements from e^+e^- experiments. We have checked that adjusting the b-fragmentation in ISAJET to correspond to the Peterson form with $\epsilon = 0.009$ (one σ away from the measured central value) changes the acceptance by less than 3 %. We have also investigated the sensitivity of the acceptance calculation to the ISAJET top fragmentation assumption. We find that when the ϵ parameter in the fragmentation of top quarks in the Monte Carlo is changed from the ISAJET default value of $0.5/M_{top}^2$ to $1.5/M_{top}^2$, the *lepton + jets* acceptance is reduced by less than 3 %.

Uncertainties in the understanding of the jet energy scale are reflected in an uncertainty in the efficiency of the *lepton + jets* selection, where we demand that there be at least two jets with $E_T >$ 10 GeV. As discussed in Section 8, the energy scale is known to ±20% for jets of E_T near 10 GeV. Scaling all the jet energies in the Monte Carlo by ±20% changes the acceptance by ±5%. Varying the parameters of the calorimeter simulation changes the efficiency of the isolation requirements by less than 3 %.

The ISAJET $t\bar{t}$ Monte Carlo generator includes radiation of gluons from the initial and final state partons. Emission of these gluons increases the jet multiplicity, and therefore increases the efficiency of the number-of-jets requirement. On the other hand, the presence of additional jets results in a lower lepton identification efficiency, since the probability of a overlap between a lepton and a jet is increased. We find that disabling gluon radiation in ISAJET increases the efficiency of the lepton isolation requirement by 5 % and decreases the efficiency of the jet multiplicity requirement by 15 %, for a total change in acceptance of 10 %. The uncertainty due to the Monte Carlo model of gluon radiation is taken to be one-half of this change, i.e. 5 %. Other features of the ISAJET modeling of $t\bar{t}$ production and decay have been compared with results from the PAPAGENO program. We find that differences in the P_T spectra of leptons from top decays affect the acceptance at the 2 % level.

The uncertainties in the trigger and lepton identification efficiencies have been discussed in previous sections of this report and are 2 % and 3 % respectively. Finally, there is a 7 % systematic uncertainty in the acceptance determination associated with the finite statistics of our Monte Carlo samples.

The uncertainties in the acceptance for this analysis are listed in Table 21. The total acceptance uncertainty is obtained by combining the individual uncertainties in quadrature and is 12 %. To this uncertainty we need to add the 6.8 % uncertainty in the luminosity of the experiment [8], for a total systematic uncertainty of 14 %.

10.6 Summary of the Search in the *lepton + jets* Channel

We have searched for evidence of $t\bar{t}$ production in a *lepton + jets* sample which consists mostly of $W + jets$ events. To suppress this background we have searched in these events for additional muons that would originate from decays of b and c quarks in $t\bar{t}$ events. We find nine events with a muon candidate within one of the two highest-E_T jets in the event, consistent with expectations from decay-in-flight and shower leakage backgrounds in $W + jets$ events. No muons are found outside the jets, in the region where the top signal is expected to concentrate.

Given the integrated luminosity of the experiment, and theoretical expectations for the $p\bar{p} \rightarrow t\bar{t}$ cross section [18, 19], we expect to observe 2.4 (1.6, 1.1) events with muons separated from the jets for $M_{top} = 80$ (90,100) GeV/c^2. This result can be combined with results from the search in the dilepton channel described in Section 9 to obtain an upper limit on the $t\bar{t}$ production crosss section, $\sigma_{t\bar{t}}$, and a lower limit on the mass of the top quark. The extraction of the M_{top} limit is the subject of the next Section.

11 Limits on the $t\bar{t}$ Production Cross Section and the Top Mass

The searches described in the previous Sections result in only one candidate event passing our $t\bar{t}$ selection criteria. With one event detected we can place upper limits on $\sigma_{t\bar{t}}$ and, using theoretical predictions for this cross section, we can also derive a limit on the mass of the top quark.

The results of searches in different channels are combined by adding acceptances and yields. Because of the requirement $P_T <$ 15 GeV/c on the possible muons from b-decays in the *lepton + jets* analysis of Section 10, there is no overlap in acceptance between that analysis and the dilepton analysis. In Table 22 we show the acceptances and the number of expected events as a function of the top mass in an exposure of 4.1 pb^{-1} using the central value of the theoretical prediction for the $t\bar{t}$ cross section from Reference [18]. The yield in the data is the one $e\mu$ candidate event described in Section 9.

The 95% confidence level (C.L.) upper limit on the cross section can be written as :

$$\sigma_{t\bar{t}} < \frac{N_{top}}{\int \mathcal{L}dt \; a_{top}} , \tag{9}$$

where N_{top} is the 95% C.L. upper limit on the number of expected top events, $\int \mathcal{L}dt$ is the integrated luminosity of the experiment ($\int \mathcal{L}dt = 4.1\ \mathrm{pb}^{-1}$) and a_{top} is the acceptance of our analysis to top events, including branching ratios. Note that since a_{top} varies slightly with top mass, the limit on $\sigma_{t\bar{t}}$ will also be a function of M_{top}.

The systematic uncertainties in a_{top} and $\int \mathcal{L}dt$, are summarized in Table 21. The total uncertainty (13%) for the number of top events predicted in the data is the acceptance-weighted average, taking into account correlations, of the uncertainties in the different analyses. This systematic uncertainty is used as the standard deviation of a Gaussian distribution which is convoluted with the Poisson statistical probability. The resulting distribution is used to obtain the 95% C.L. upper limit on the expected

Uncertainty Source	Dilepton	$t \rightarrow b \rightarrow \mu$	Combined analysis
Trigger efficiency	2%	2%	2%
High P_T lepton geometrical and kinematical acceptance	4%	2%	3.5%
High P_T lepton detection efficiency	5%	3%	4.5%
Monte Carlo gluon radiation	6%	5%	5.8%
Simulation of calorimeter isolation	4%	3%	3.7%
Top fragmentation	2%	1%	1.8%
Bottom fragmentation	-	3%	0.7%
BR($b \rightarrow \mu$)	-	5%	1.2%
Calorimeter (Jet) Energy Scale	2%	5%	1.9%
Monte Carlo statistics	3%	7%	2.9%
Luminosity	6.8%	6.8%	6.8%
Total	13%	15%	13%

Table 21: Summary of uncertainties in the acceptance calculation

number of top events as a function of M_{top}. Given that one event was observed, and without subtracting backgrounds, we find an upper limit of N_{top}=4.90 for having observed either zero or one event. (If the effect of systematic uncertainties had been ignored, N_{top}=4.74 would have been obtained.) The 95% C.L. limit on $\sigma_{t\bar{t}}$ varies slightly as a function of M_{top} and is 113 pb for M_{top} = 90 GeV/c^2.

Using theoretical expectations for $\sigma_{t\bar{t}}$, and assuming Standard Model charged current decays for the top quarks, the cross section limits can be translated into a lower

M_{top}	$\sigma_{t\bar{t}}$	Acc x Br (dilepton)	Acc x Br ($t \rightarrow b \rightarrow \mu$)	Number of events in 4.1 pb^{-1}
80 GeV/c^2	291 pb	0.68%	0.20%	10.5
90 GeV/c^2	150 pb	0.80%	0.26%	6.5
100 GeV/c^2	94 pb	0.83%	0.29%	4.3

Table 22: Fractions of $t\bar{t}$ events accepted by the dilepton and $t \rightarrow b \rightarrow \mu$ analyses. The numbers of expected events are for 4.1 pb^{-1}.

limit on the mass of the top quark. Figure 37 shows the upper limits on the $t\bar{t}$ cross section as a function of the top mass together with the calculation of this cross section from Reference [18]. This calculation is based on the QCD total cross section formulas for heavy quark production, complete through order α_s^3, by Nason *et al.* [19]. The shaded region represents the theoretical uncertainty in the calculation based on different choices of the renormalization scale and the QCD scale parameter Λ.

To set a lower limit on M_{top} we find the point at which the $\sigma_{t\bar{t}}$ limit curve crosses the lower (i.e. more pessimistic) bound of the theoretical prediction. At the 95% C.L. we find $M_{top} > 72$ GeV/c^2 for the $e\mu$ analysis of Reference [14], $M_{top} > 85$ GeV/c^2 for the dilepton analysis and $M_{top} > 91$ GeV/c^2 for the combination of the dilepton analysis with the $t \rightarrow b \rightarrow \mu$ analysis.

12 Acknowledgments

We thank the staff of the Fermilab Accelerator Division, the CDF technical and support staff, and the staffs of the collaborating institutions for their invaluable assistance. This work is supported in part by the United States Department of Energy; the National Science Foundation; the Istituto Nazionale di Fisica Nucleare (Italy); the Ministry of Science, Culture and Education of Japan, and the A.P. Sloan Foundation.

References

[1] S. L. Glashow, Nucl. Phys. 22, 579 (1961). S. Weinberg, Phys. Rev. Lett. 19, 1264 (1967). A. Salam, in *Elementary Particle Theory*, edited by N. Svartholm (Almqvist and Wiksell, Sweden, 1968), p. 367.

[2] S. L. Glashow, J. Illiopoulos and L. Maiani, Phys. Rev. D2, 1285 (1970); M. Kobayashi and M. Maskawa, Prog. Theor. Phys. 49, 652 (1973)

[3] A. Bean *et al.*, Phys. Rev. D35, 3533 (1987).

[4] W. Bartel *et al.*, Phys. Lett. 146B, 437 (1984).

[5] C. Albajar *et al.*, Z. Phys. C48, 1 (1990).

[6] T. Åkesson *et al.*, Z. Phys. C46, 179 (1990).

[7] see for example F. Dydak, Proc. 25th Int. Conf. on High Energy Physics, Singapore 1990 .

[8] F. Abe *et al.*, Phys. Rev. D44, 29 (1991).

[9] H. Albrecht *et al.*, Phys. Lett. 192B, 245 (1987); M. Artuso *et al.*, Phys. Rev. Lett. 62, 2233 (1989); G. Altarelli, P. Franzini, Z. Phys. C37, 271 (1988); J. Ellis *et al.*, Nucl. Phys. B304, 205 (1988).

[10] F. Abe *et al.*, Phys. Rev. Lett. 65, 2243 (1990).

[11] F. Abe *et al.*, Phys. Rev. D43, 2070 (1991).

[12] G. Abrams *et al.*, Phys. Rev. Lett. 63, 2173 (1989).

D. Decamp *et al.*, Phys. Lett. B231, 519 (1989).

P. Aarnio *et al.*, Phys. Lett. B231, 539 (1989).

B. Adeva *et al.*, Phys. Lett. B231, 509 (1989).

M. Z. Akrawy *et al.*, Phys. Lett. B231, 530 (1989).

J. Alitti *et al.*, Phys. Lett. B241, 150 (1990).

[13] W. Marciano and A. Sirlin, Phys. Rev. D29, 945 (1984); D. Bardin *et al.*, Z. Phys. C32, 121 (1986); U. Amaldi *et al.*, Phys. Rev. D36, 1385 (1987); P. Langacker and M. Luo, Phys. Rev. D44, 817 (1991); J. Carter, Proceedings of the International Lepton-Photon Symposium, CERN, 1991.

[14] F. Abe *et al.*, Phys. Rev. Lett. 64, 147 (1990).

[15] F. Abe *et al.*, Phys. Rev. Lett. 64, 142 (1990); F. Abe *et al.*, Phys. Rev. D43, 664 (1991).

[16] F. Abe *et al.*, Fermilab-Pub-91/280-E, submitted to Phys. Rev. Lett..

[17] The muon trigger was not fully operational in the early part of the run, the integrated luminosity for data collected with this trigger is 3.5 pb^{-1}.

[18] G. Altarelli, M. Diemoz, G. Martinelli and P. Nason, Nucl. Phys. B308, 724 (1988). R.K. Ellis Fermilab-Pub-91/30-T

[19] P. Nason, S. Dawson and R.K. Ellis, Nucl. Phys. B303, 607 (1988).

[20] See for instance, V. Barger and R. Phillips, Collider Physics, Addison-Wesley Publishing Company (1987).

[21] F. Abe *et al.*, Nucl. Instrum. Methods A271, 387 (1988).

[22] The CDF coordinate system defines z along the proton beam direction, θ as the polar angle and ϕ as the azimuthal angle.

[23] D. Amidei *et al.*, Nucl. Instrum. Methods A269, 51 (1988).

[24] C. Grosso-Pilcher and S. White, CDF Collaboration, Fermilab-Pub-91/550-E.

[25] G. Ascoli *et al.*, Nucl. Instrum. Methods A269, 63 (1988).

[26] G.W. Foster *et al.*, Nucl. Instrum. Methods A269, 93 (1988).

[27] J.T. Carrol *et al.*, Nucl. Instrum. Methods A300, 552 (1991).

[28] H. Areti et el., Proc. 23rd Int. Conf. on High Energy Physics, Berkeley CA, 1986; I. Gaines et al., Proc. Int. Conf. on Computing in High Energy Physics, Asilomar, 1987 Comput. Phys. Commun 45 (1987) 233; J. Biel et al., ibid., p 331.

[29] For details on plug electron identification and several aspects of the dilepton analysis, see Y. Seiya, University of Tsukuba, Ph. D. thesis, 1992.

[30] F. Paige and S.D. Protopopescu, BNL Report No. BNL 38034, 1986 (unpublished). We used version 6.22.

[31] J. Freeman, Proceedings of the Workshop on Detector Simulation for the SSC, edited by L. E. Price, Argonne National Laboratory (1987), p. 190.

[32] F. Abe *et al.*, Phys. Rev. Lett. 62, 613 (1989).

[33] M.A. Worris, Proceed. of the Rice Meeting (1990 Meeting of the Division of Particle and Fields of the APS), 470 (1990)

[34] B. Adeva *et al.*, L3 preprint No. 27, (1991)

[35] Particle Data Group, J. J. Hernandez *et al.*, Phys. Lett. B239, 1 (1990).

[36] I. Hinchliffe, Private Communication.

[37] For details on muon backgrounds and several aspects of the $\mu + jets$ analysis, see L. Demortier, Brandeis University, Ph. D. thesis, 1991.

[38] F. Abe *et al.*, Phys. Rev. Lett. 67, 2418 (1991).

[39] F. Abe *et al.*, Phys. Rev. Lett. 67, 2937 (1991).

[40] C. Peterson, D. Schlatter, I. Schmitt and P. Z. Zerwas, Phys. Rev. D27, 105 (1983).

[41] J.Chrin, Z. Phys. C36, 163 (1987); D. Decamp *et al.*, Phys. Lett. B244 , 551 (1990).

FIGURE CAPTIONS

Figure 1: The expected P_T spectrum of leptons from $t \rightarrow Wb, W \rightarrow l\nu$ from the ISAJET Monte Carlo program for $M_{top} = 90$ GeV/c^2.

Figure 2: The CDF detector as configured for the 1988-89 run. Closest to the interaction point are the VTPCs, surrounded by the CTC, the coil of the solenoid, the central calorimeters and the central muon chambers. To the left are forward gas calorimeters and muon toroids. The detector is forward-backward symmetric about the interaction point.

Figure 3: Efficiencies of the lepton triggers as a function of transverse momentum. (a) Efficiency for central electrons. (b) Efficiency for plug electrons. (c) Efficiency for central muons; the solid line is the nominal efficiency curve of the track processor; delta-rays cause the efficiency at high-P_T to be slightly lower than the nominal. The efficiency for bins where all events passed the trigger are plotted with no error bar.

Figure 4: Central electron quality variables for $Z \rightarrow ee$ events. Also shown are the values of the cuts for the $e + jets$ central electron selection. (a) Ratio of calorimeter energy and momentum ; (b) Ratio of hadronic and electromagnetic energy deposition; (c) Lateral shower profile variable; (d) Match in the Rϕ-view between the track and the shower position as measured in the strip chambers ; (e) Match in the z-view between the track and the shower position as measured in the strip chambers; (f) Chi-squared for the electron hypothesis from the shape of the shower in the z-view of the strip chamber; (g) Chi-squared for the electron hypothesis from the shape of the shower in the Rϕ-view of the strip chamber.

Figure 5: Distributions of HAD/EM and χ^2_{trans} for plug electron candidates from W decays. Also indicated in the Figure are the cutoffs used in the selection of plug electrons.

Figure 6: Efficiency for the CTC (a), VTPC (b), and combined track matching (c) as a function of rapidity (η) for plug electrons from Z decays.

Figure 7: Energy deposited in the calorimeter by cosmic ray muons (a) EM calorimeter (b) EM+HAD calorimeter.

Figure 8: The match (δ_x) between the CTC track extrapolated to the lowest wire plane of the muon chambers and the muon chamber track for a sample of muons from W decays of $P_T > 20$ GeV/c.

Figure 9: The transverse momentum distribution of b-quarks from the ISAJET Monte Carlo program for M_{top}= 90 GeV/c^2 (arbitrary normalization).

Figure 10: The expected transverse momentum distribution of muons from b-decays in $t\bar{t}$ events with $|\eta| \leq 0.63$, for M_{top}= 90 GeV/c^2 from the ISAJET Monte Carlo program (arbitrary normalization).

Figure 11: Invariant mass distribution for oppositely charged dimuon candidates. One muon in these events is required to have $|\delta_x| < 10$ cm.

Figure 12: The Pt distribution of muons in the J/ψ peak, 3.0 GeV/c^2< $M_{\mu\mu}$ < 3.16 GeV/c^2. The contribution from the continuum underneath the peak has been subtracted using the events in the sideband regions. The threshold behavior at P_T = 3 GeV/c is an artifact of the trigger.

Figure 13: The distribution of $\delta_x\ P_T$ (GeV/c)/ 15 cm for the second muon in the J/ψ peak. The distribution has been corrected for the background under the peak using the events in the sidebands. Also shown is a Gaussian, centered at zero, and of unit standard deviation.

Figure 14: The efficiency for the requirement $|\delta_x| < \min(15\text{ cm}, 60\text{cm}/P_T)$, evaluated from events in the J/ψ peak after applying a correction for the non-muon background contamination using the events in the sideband regions.

Figure 15: Isolation distributions for leptons from Z^0 decay. a) E_T^{cone} for central electrons. b) $I = E_T^{cone}/E_T^e$ for plug electrons. c) E_T^{cone} for central muons. d) P_T^{cone} for central muons. The histograms are from Monte Carlo and the points are from CDF data. The cut values used in the dilepton analysis are indicated with arrows.

Figure 16: Isolation distributions for leptons from $t\bar{t}$ Monte Carlo with M_{top} = 90 GeV/c^2. a) E_T^{cone} for central electrons. b) $I = E_T^{cone}/E_T^e$ for plug electrons. c) E_T^{cone} for central muons. d) P_T^{cone} for central muons. The cut values used in the dilepton analysis are indicated with arrows.

Figure 17: Distribution of the isolation variable E_T^{iso} for CDF inclusive electrons (points), Monte Carlo bottom electrons (solid curve), and Monte Carlo top electrons (M_{top}=75 GeV/c^2, histogram). Residual W and Drell-Yan events form the peak in the lowest E_T^{iso} bin. The $b\bar{b}$ Monte Carlo curve has been normalized to the data in the region above 0.5 GeV. From Reference [15].

Figure 18: Efficiency for reconstructing a cluster of $E_T \geq$ 10 GeV in the hemisphere opposite the photon candidate as a function of the photon E_T.

Figure 19: The transverse mass distribution of $W \rightarrow e\nu + 1\ jet$ candidates compared to Monte Carlo expectations.

Figure 20: The regions in η-ϕ space covered by central electrons (CE), plug electrons (PE), muons in the central muon detector (MU) and muons outside the central muon region detected as minimum ionizing particles (MI). Not to scale.

Figure 21: The expected number of $e\mu$ events in 4.1 pb^{-1} with the transverse momentum of both leptons above a common threshold P_T^{min}, as a function of the threshold, for ISAJET $t\bar{t}$ and $b\bar{b}$ events. Lepton isolation cuts were not imposed for this figure.

Figure 22: CDF electron-muon data with integrated luminosity of 4.1 pb^{-1}. a) Electron transverse energy vs. muon transverse momentum. b) Transverse momentum of the least energetic lepton vs. dilepton azimuthal angle. The region to the right of the dotted line is excluded by the back-to-back cut.

Figure 23: Monte Carlo $t\bar{t} \rightarrow e\mu + X$ events for $M_{top} = 90$ GeV/c^2 (unnormalized). a) Electron transverse energy vs. muon transverse momentum. b) Transverse momentum of the least energetic lepton vs. dilepton azimuthal opening angle.

Figure 24: Monte Carlo $Z^0 \rightarrow \tau\tau \rightarrow e\mu + X$ events (unnormalized). a) Electron transverse energy vs. muon transverse momentum. b) Transverse momentum of the least energetic lepton, Min(E_T^e, P_T^μ), vs. the azimuthal separation between electron and muon.

Figure 25: Displays of the top candidate event. a) View of the tracking chamber in the transverse plane. b) Calorimeter transverse energy depositions in η-ϕ space.

Figure 26: Dilepton invariant mass distributions. a) CDF dielectron data with integrated luminosity of 4.1 pb^{-1}. The curve is a Monte Carlo Drell-Yan prediction. b) CDF dimuon data with integrated luminosity of 4.1 pb^{-1}. c) Monte Carlo $t\bar{t} \rightarrow ll+X$ for $M_{top} = 90$ GeV/c^2 (unnormalized).

Figure 27: Monte Carlo distributions in the $\not{E}_T - \Delta\phi_{ll}$ plane for $t\bar{t} \rightarrow ee + X$ with $M_{top} = 90$ GeV/c^2 (unnormalized). Events with dilepton masses in the range 75-105 GeV/c^2 are not included in the figure.

Figure 28: Distributions in the $\not{E}_T - \Delta\phi_{ll}$ plane for CDF data with integrated luminosity of 4.1 pb^{-1}. Dotted lines indicate the event topology cuts. a) Dielectrons. b) Dimuons. Events with dilepton masses in the range $75 < M_{ll} < 105$ GeV/c^2 are not included in the figure.

Figure 29: The efficiencies of the dilepton analysis as a function of M_{top}.

Figure 30: The decay chain used in the top search in the $l + jets$ channel. The muon can come from either b-quark or from the decay chain $b \rightarrow c \rightarrow \mu$.

Figure 31: Transverse mass distribution of $e+jets$ events compared with a $W+2$ $jets$ prediction from the Papageno Monte Carlo and the detector simulation. The Monte Carlo prediction is normalized to the number of events observed in the data.

Figure 32: Transverse mass distribution of $\mu + jets$ events compared with the same Monte Carlo of Figure 31.

Figure 33: The η-ϕ distance ΔR between muon candidates and the nearest jet of E_T > 10 GeV in QCD jet events.

Figure 34: The η-ϕ distance ΔR between the muon candidate and the nearest of the two most energetic jets in the lepton + jets sample. Also shown is the 90 GeV/c^2 $t\bar{t}$ Monte Carlo prediction (arbitrary normalization).

Figure 35: The probability for a track in QCD jet events to be reconstructed as a muon with the requirements described in the text. (a) $\Delta R < 0.5$ from the nearest jet of $E_T > 10$ GeV; (b) $\Delta R > 0.5$.

Figure 36: The transverse momentum spectrum of tracks within the solid angle covered by the muon chambers in the 195 lepton+ jet events; (a) $\Delta R < 0.5$ from the two highest E_T jets (b) $\Delta R > 0.5$.

Figure 37: Our 95% C.L. limits on $\sigma_{t\bar{t}}$ compared with a band of theoretical predictions from Reference [18]. We show three sets of experimental limits : (1) From the eμ analysis of Reference [14]; (2) From the analysis in the dilepton modes ee, eμ and $\mu\mu$; (3) From the combination of the dilepton analysis with the $t \rightarrow b \rightarrow \mu$ analysis.

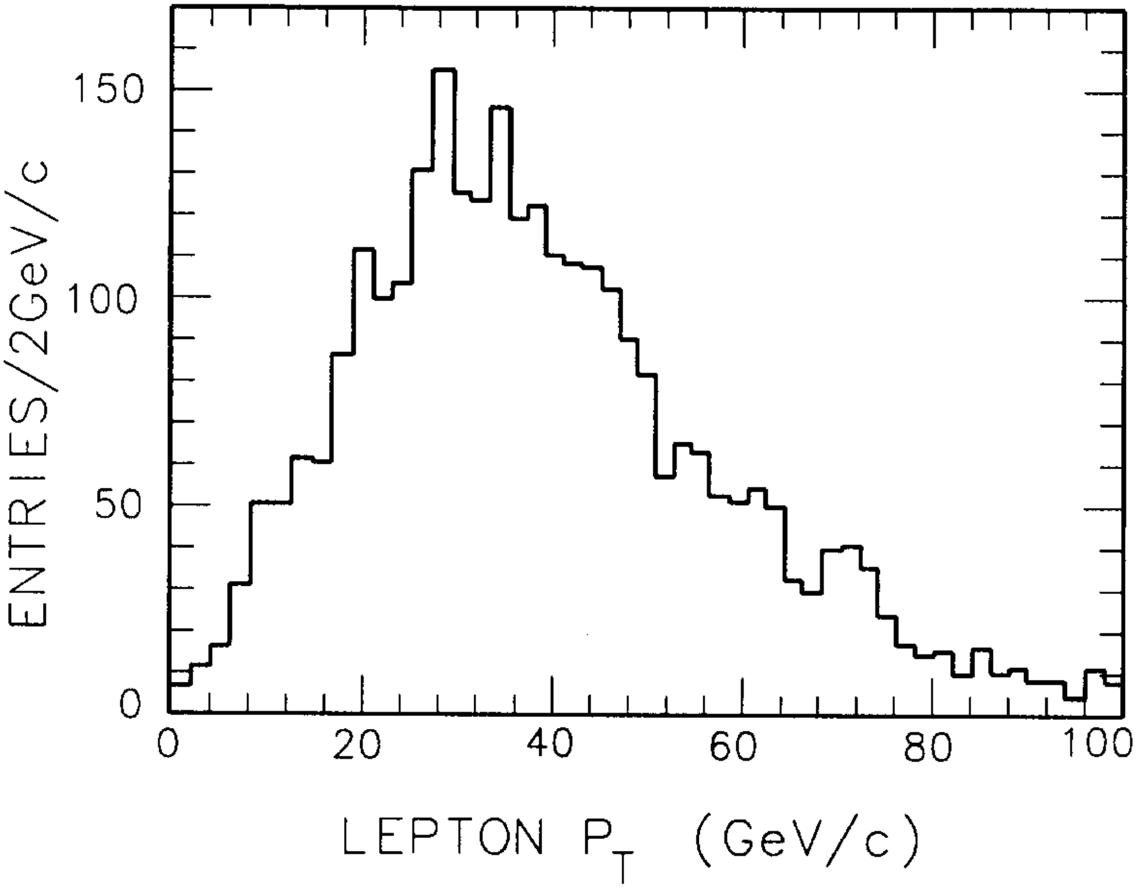
ENTRIES/2GeV/c
0
50
100
150
0
20
40
60
80
100
LEPTON P_T (GeV/c)

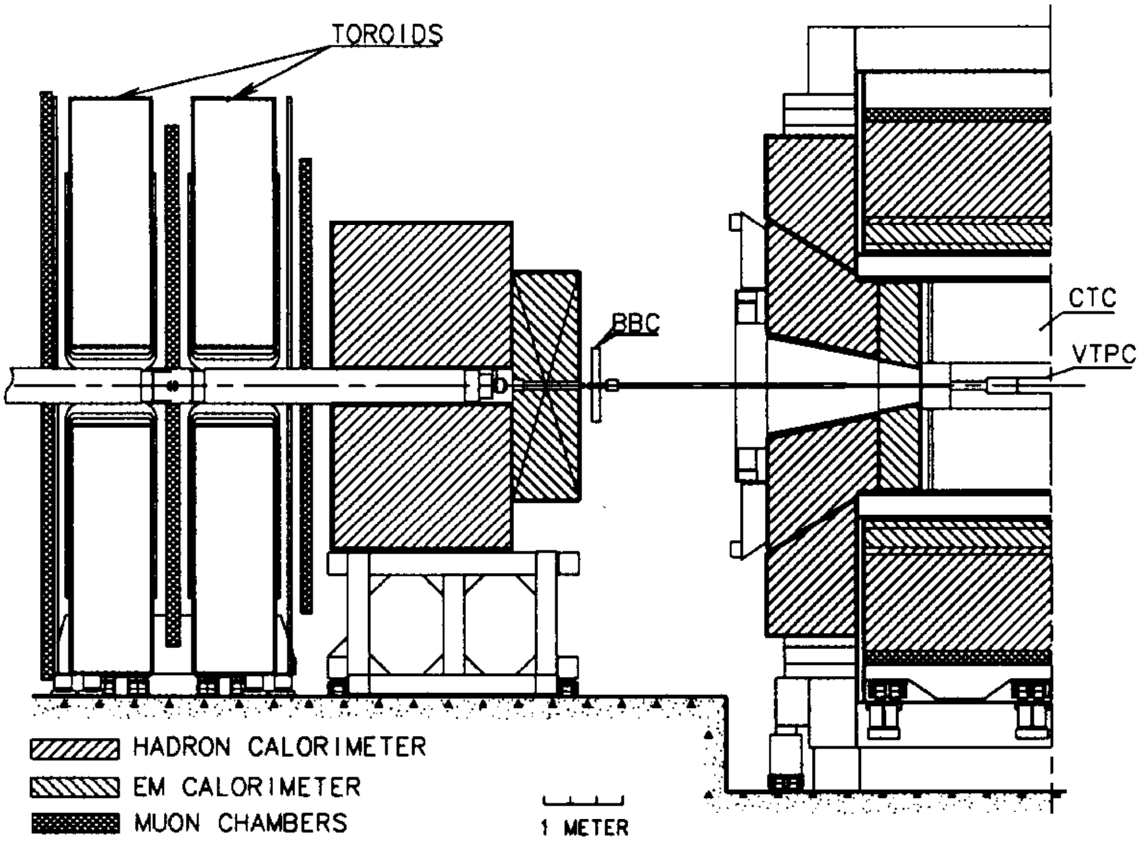
TOROIDS
BBC
CTC
VTPC
HADRON CALORIMETER
EM CALORIMETER
MUON CHAMBERS
1 METER

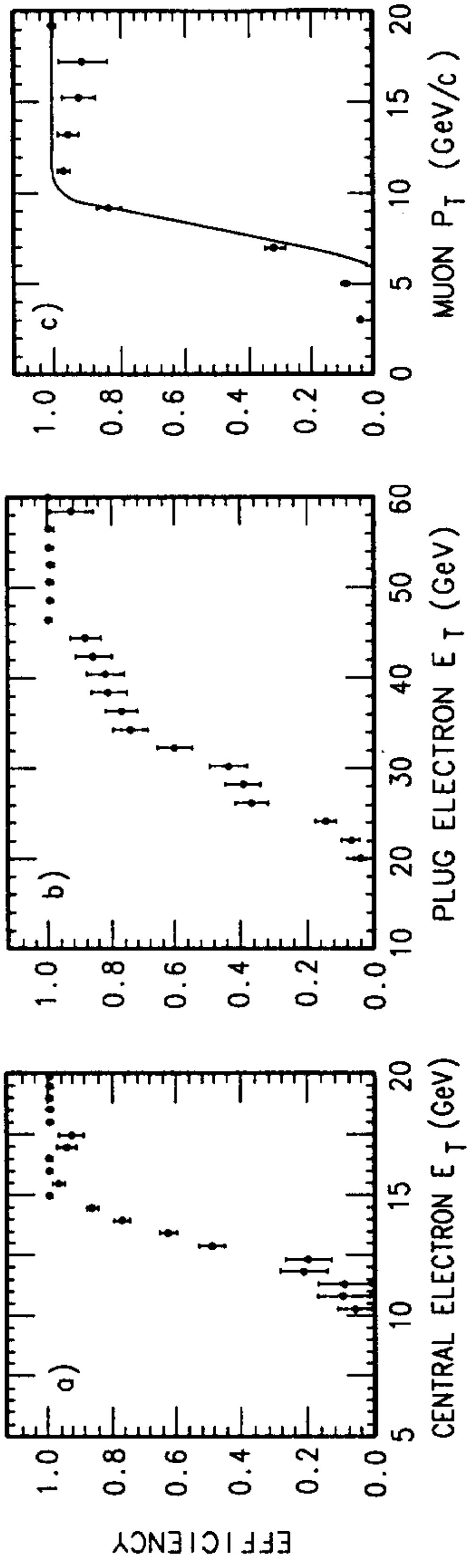
EFFICIENCY
a)
CENTRAL ELECTRON E T (GeV)
b)
PLUG ELECTRON E T (GeV)
c)
MUON P T (GeV/c)
0.0
0.2
0.4
0.6
0.8
1.0
5
10
15
20
10
20
30
40
50
60
0
5
10
15
20

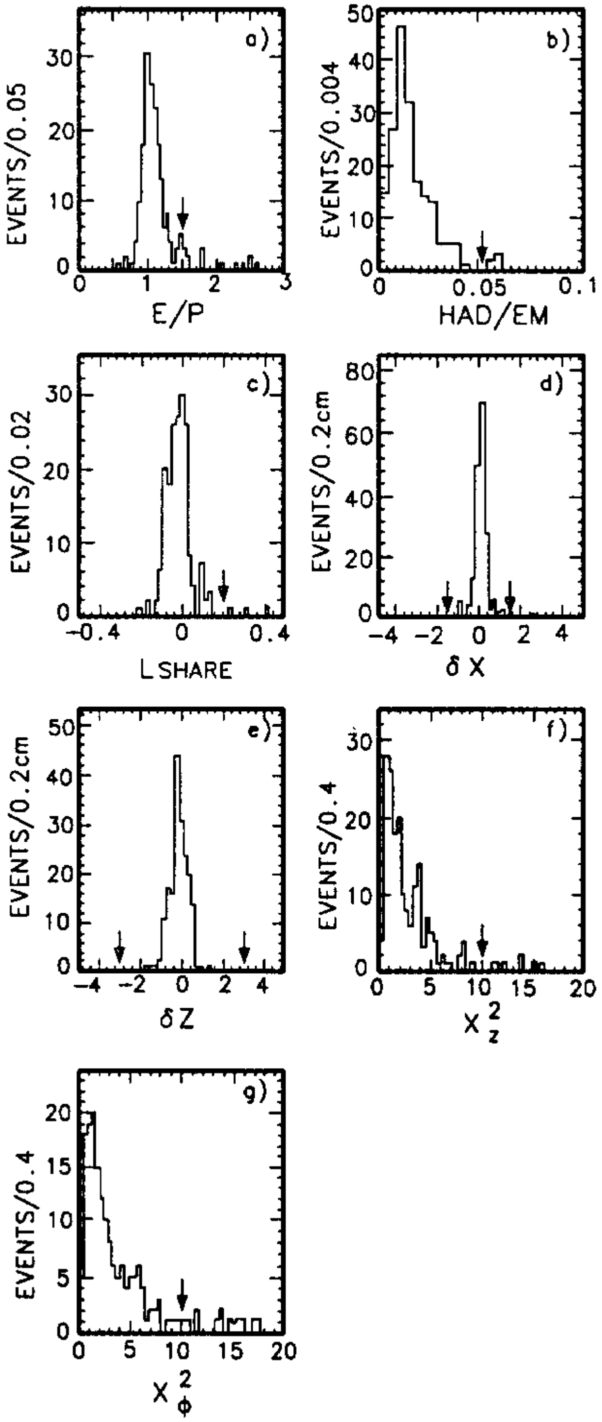
a)
EVENTS/0.05
E/P
0 1 2 3
0 10 20 30
b)
EVENTS/0.004
HAD/EM
0 0.05 0.1
0 10 20 30 40 50
c)
EVENTS/0.02
LSHARE
−0.4 0 0.4
0 10 20 30
d)
EVENTS/0.2cm
δ X
−4 −2 0 2 4
0 20 40 60 80
e)
EVENTS/0.2cm
δ Z
−4 −2 0 2 4
0 10 20 30 40 50
f)
EVENTS/0.4
χ^2_z
0 5 10 15 20
0 10 20 30
g)
EVENTS/0.4
χ^2_ϕ
0 5 10 15 20
0 5 10 15 20

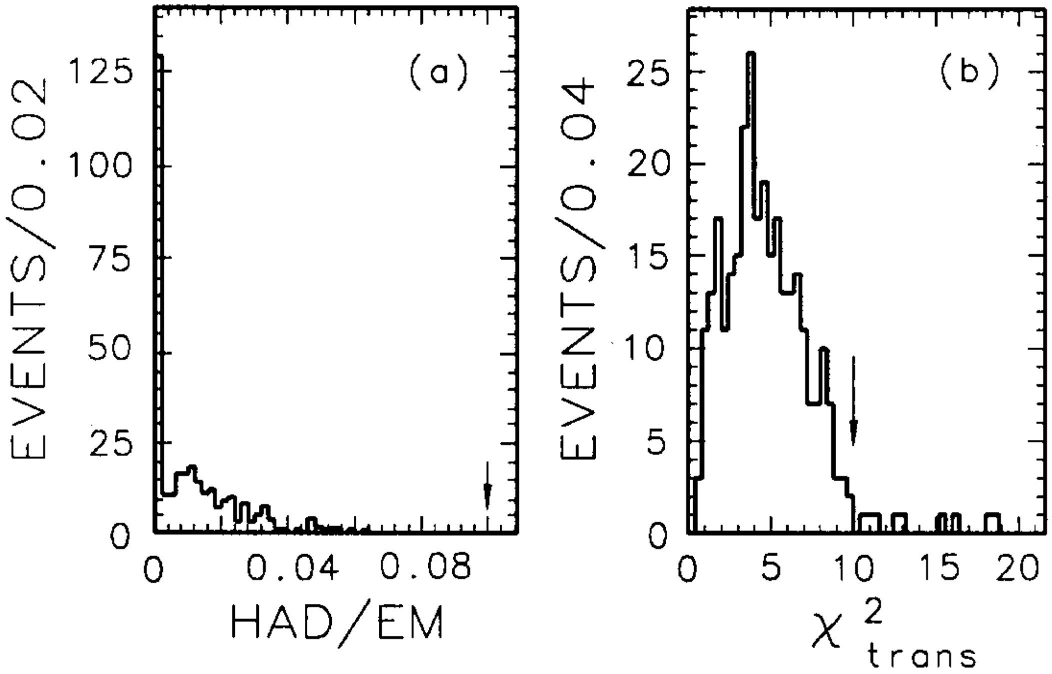
(a)
EVENTS/0.02
0
25
50
75
100
125
0
0.04
0.08
HAD/EM
(b)
EVENTS/0.04
0
5
10
15
20
25
0
5
10
15
20
χ^2_{trans}

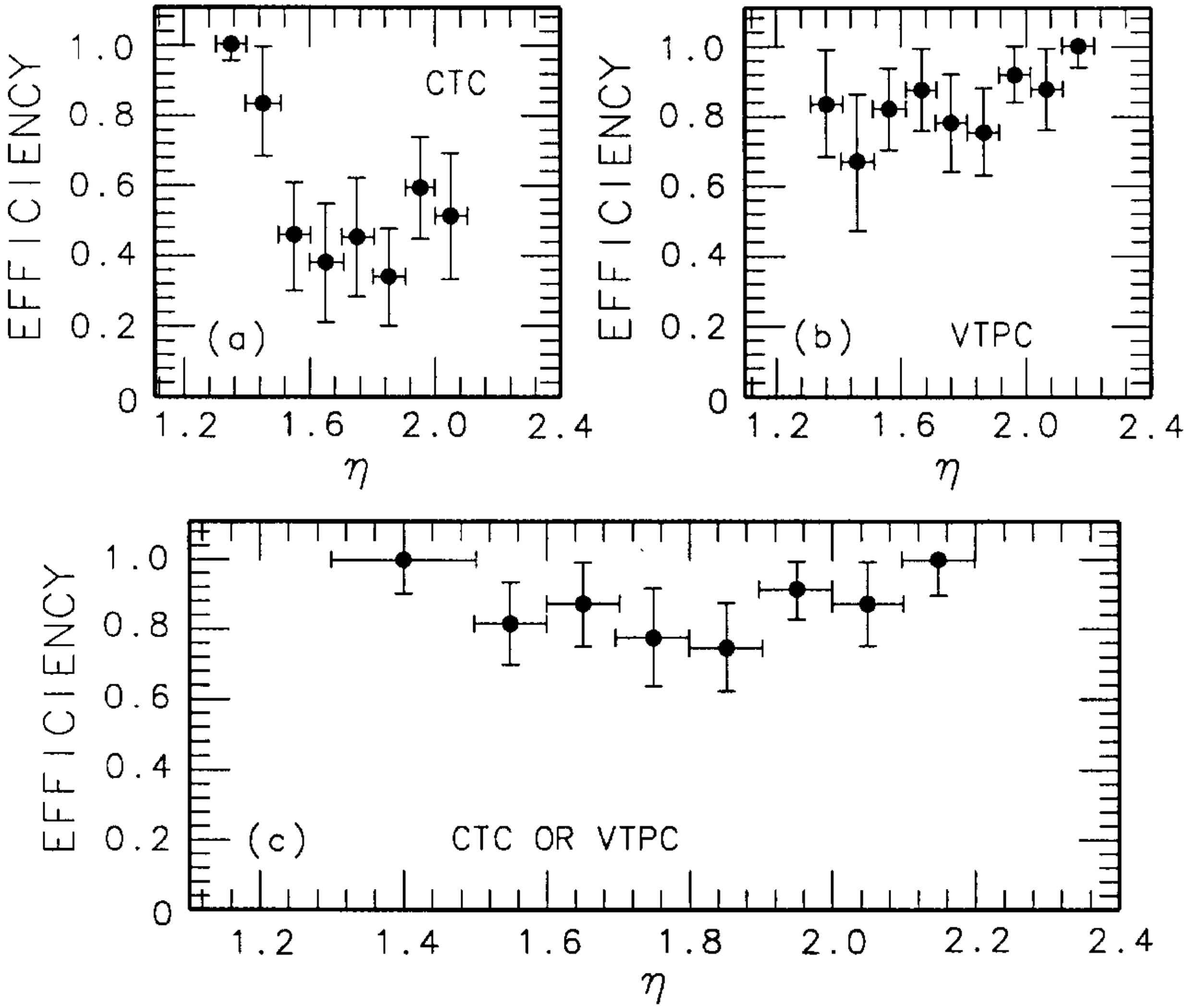
EFFICIENCY
η
1.0
0.8
0.6
0.4
0.2
0
1.2
1.6
2.0
2.4
(a)
CTC
(b)
VTPC
(c)
CTC OR VTPC
1.4
1.8
2.2

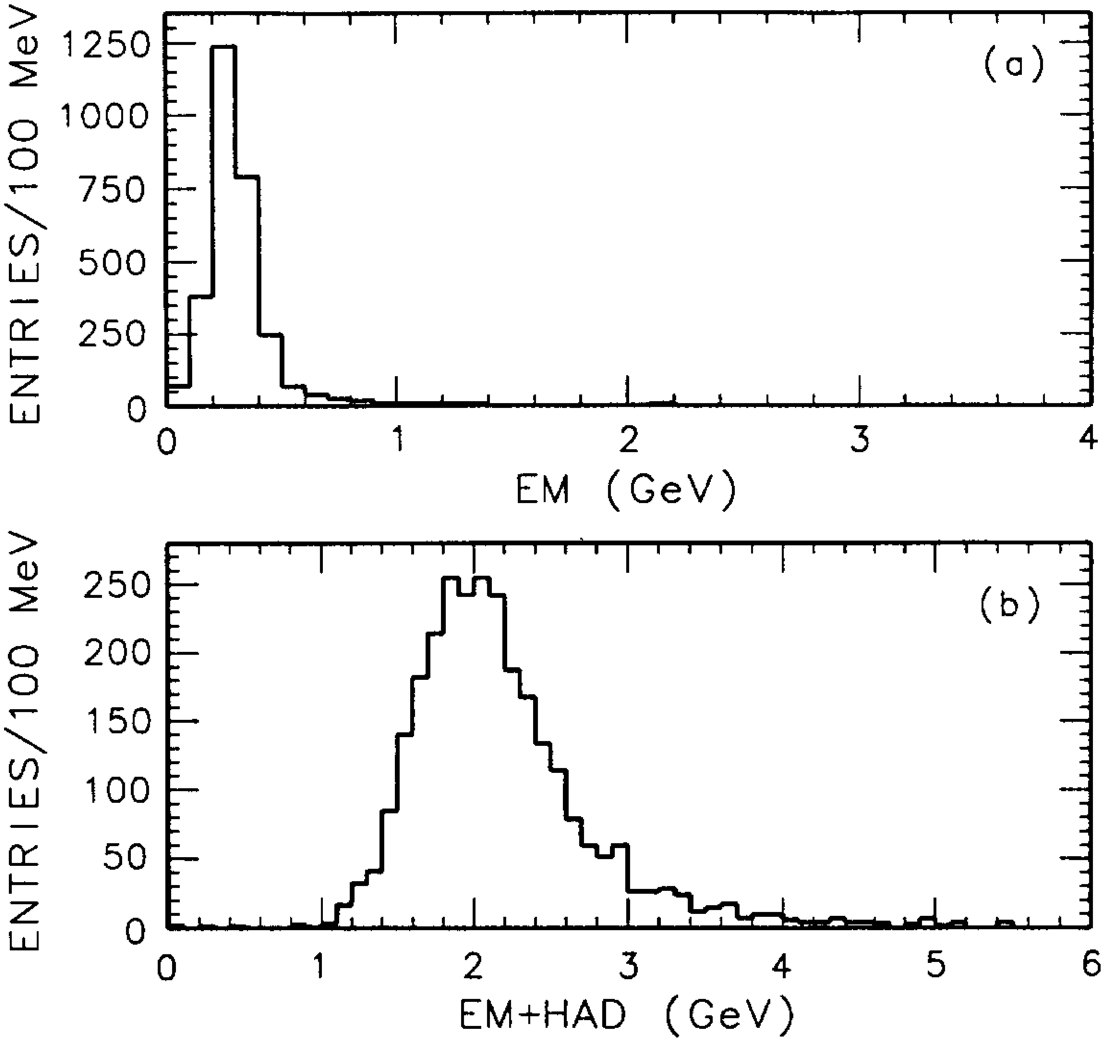
ENTRIES/100 MeV
1250
1000
750
500
250
0
(a)
0
1
2
3
4
EM (GeV)
ENTRIES/100 MeV
250
200
150
100
50
0
(b)
0
1
2
3
4
5
6
EM+HAD (GeV)

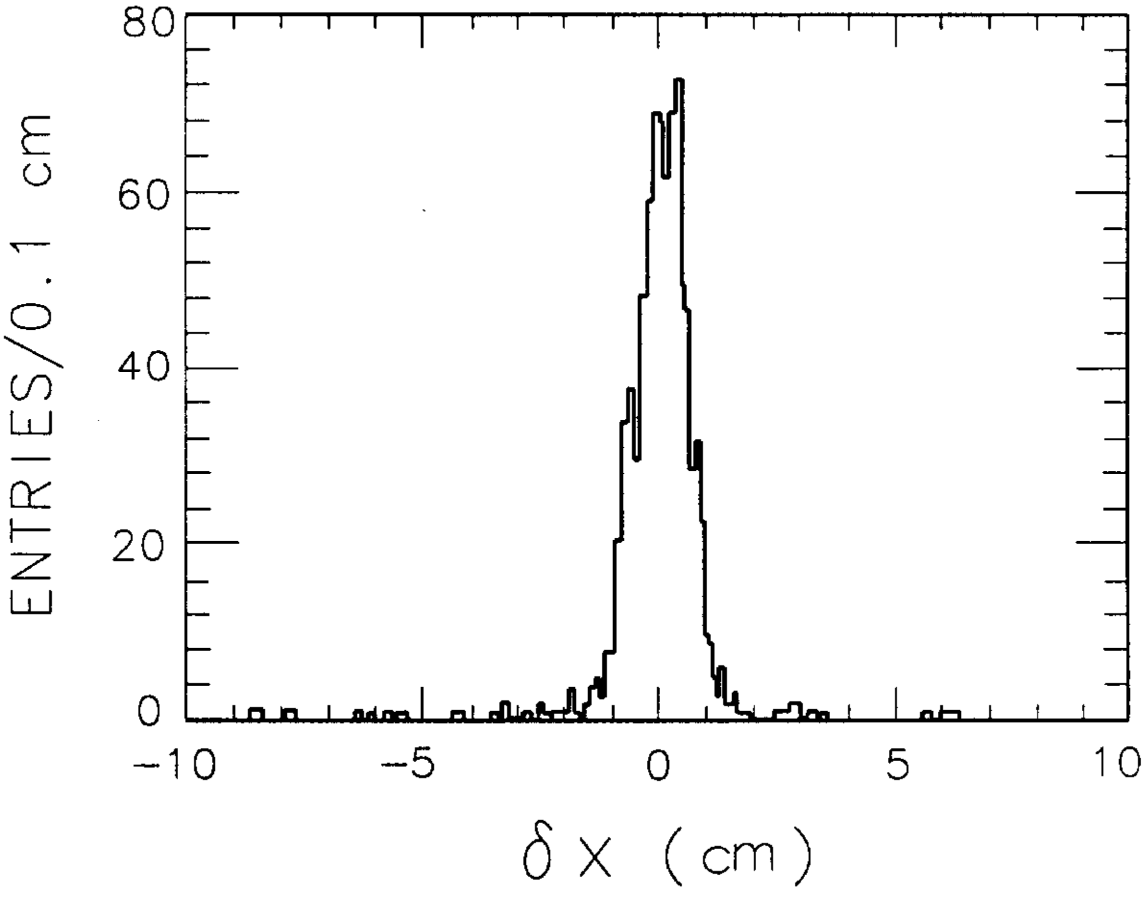
80
60
40
20
0
ENTRIES/0.1 cm
−10
−5
0
5
10
δ X (cm)

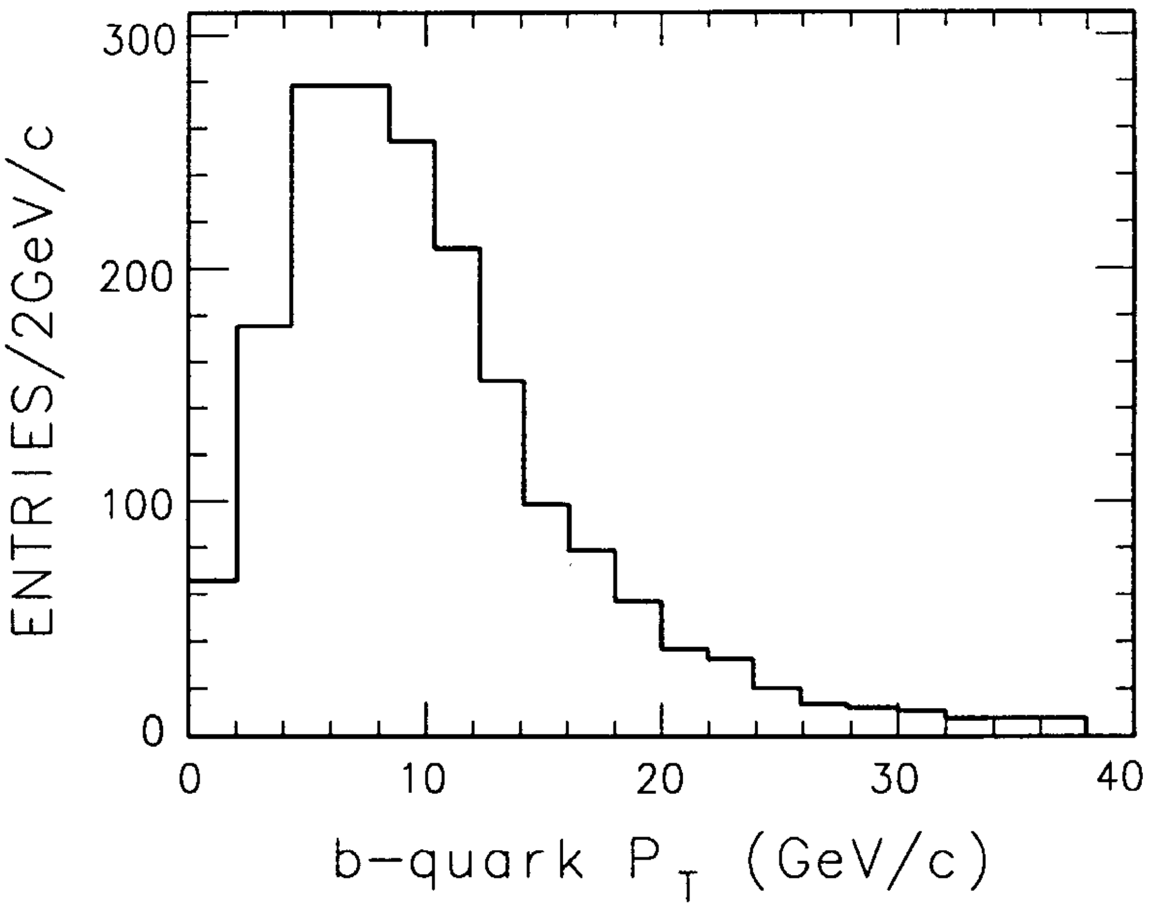
ENTRIES/2GeV/c
300
200
100
0
0
10
20
30
40
b-quark P_T (GeV/c)

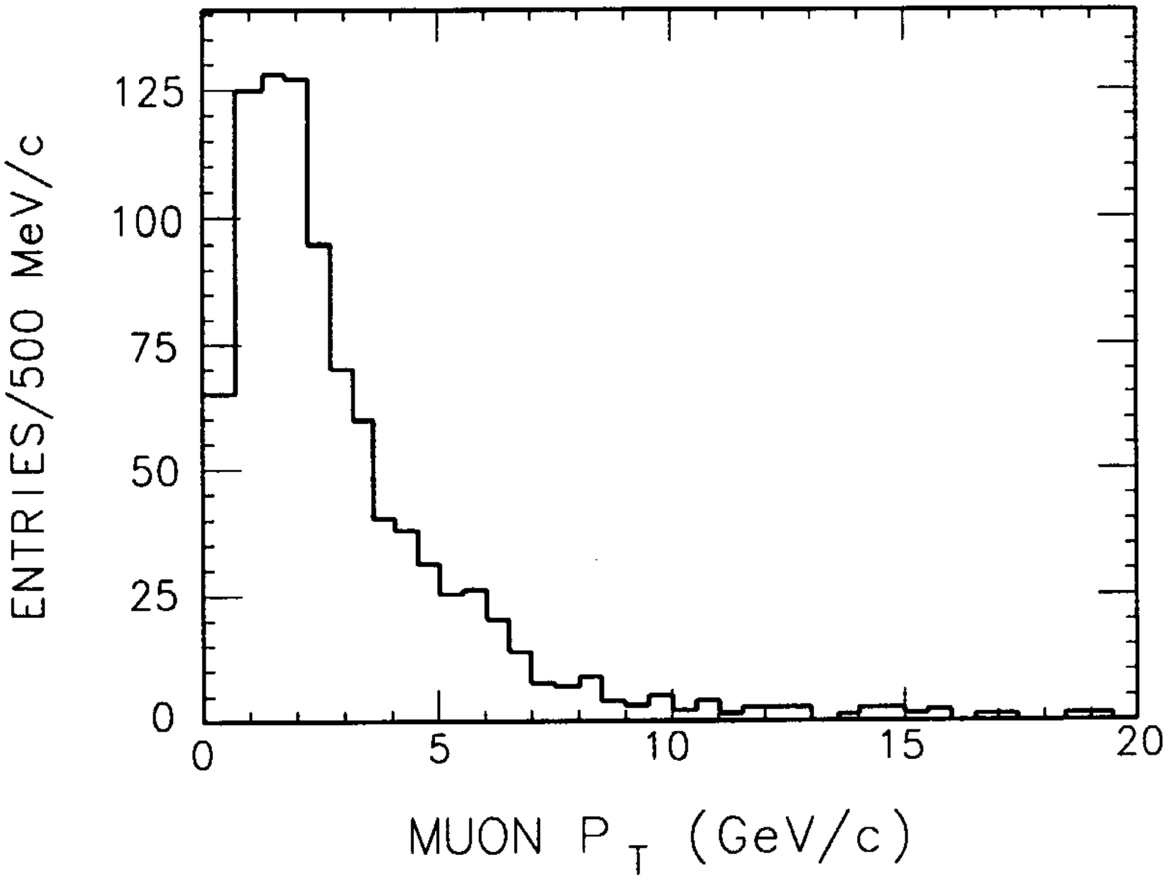
ENTRIES/500 MeV/c
0
25
50
75
100
125
0
5
10
15
20
MUON P_T (GeV/c)

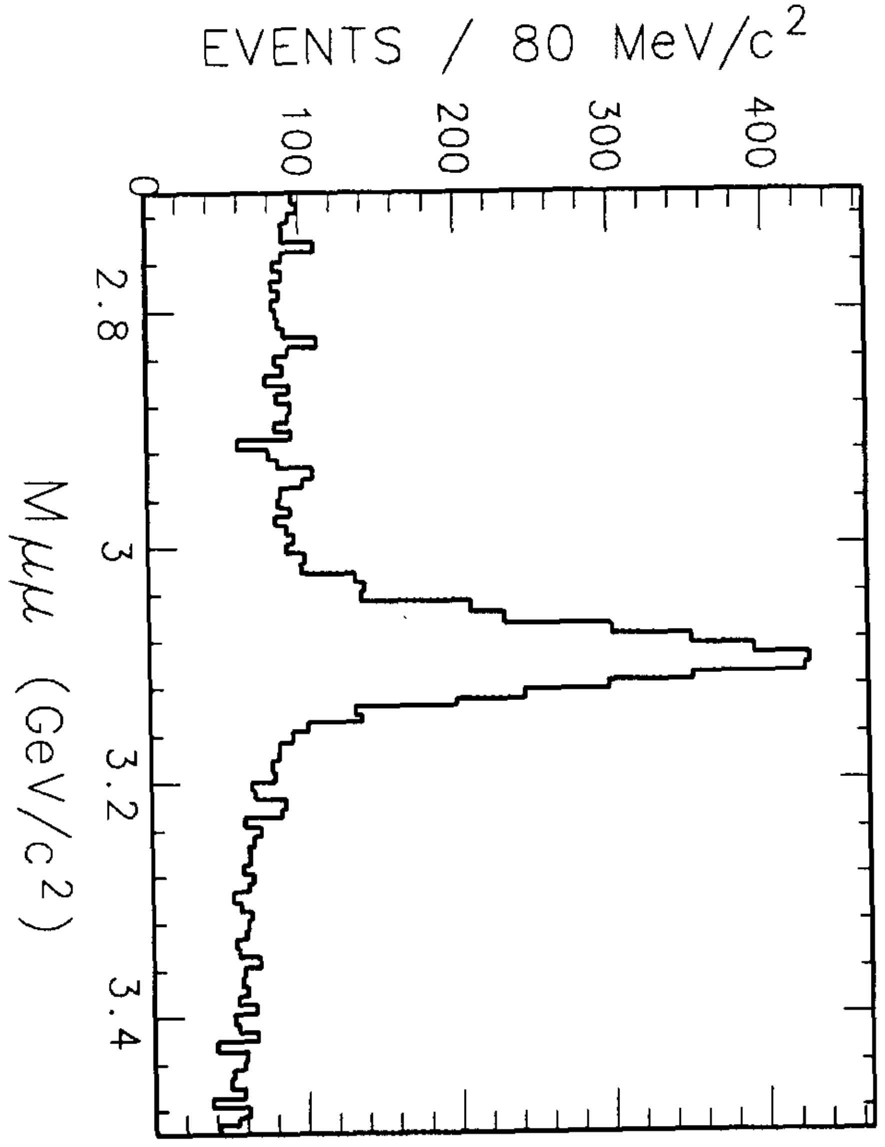
EVENTS / 80 MeV/c^2
0
100
200
300
400
2.8
3
3.2
3.4
$M_{\mu\mu}$ (GeV/c^2)

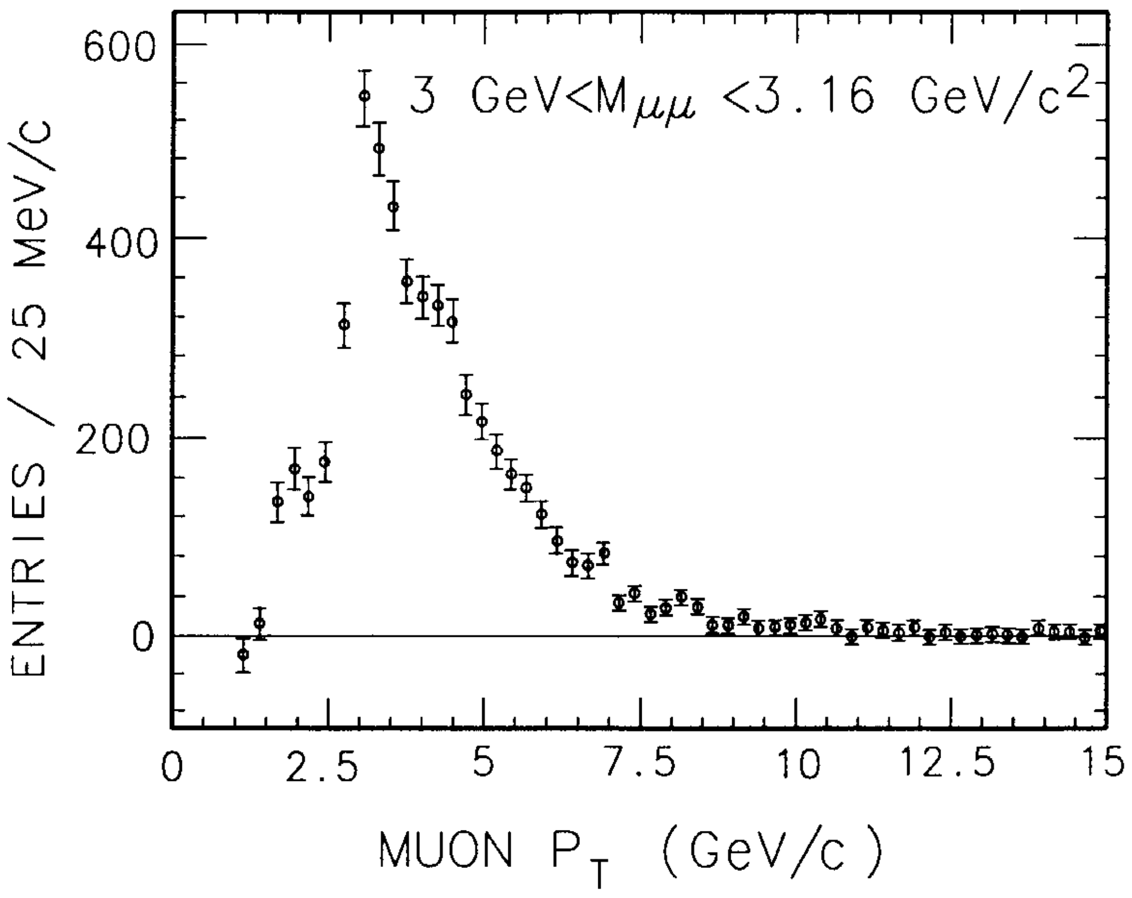
3 GeV<$M_{\mu\mu}$ <3.16 GeV/c^2
ENTRIES / 25 MeV/c
600
400
200
0
0
2.5
5
7.5
10
12.5
15
MUON P_T (GeV/c)

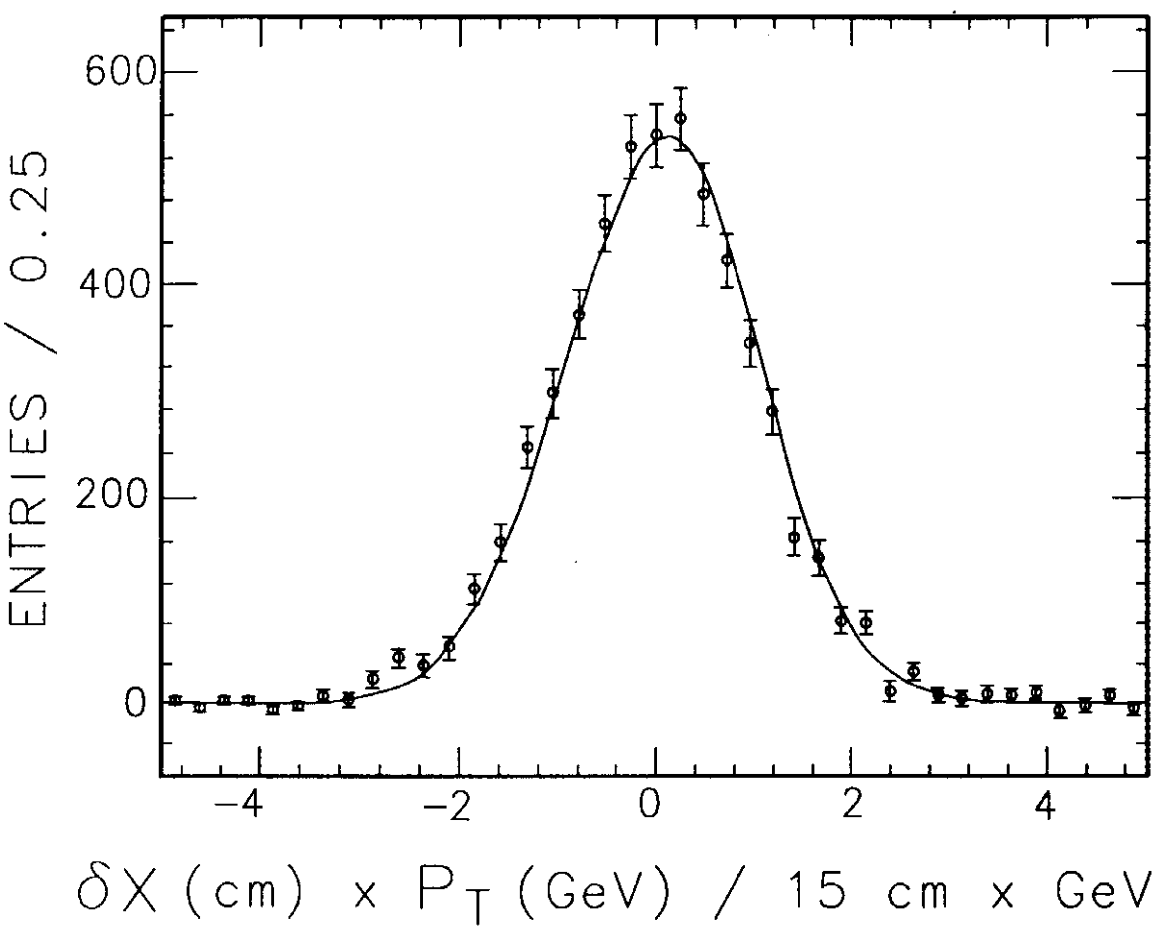
ENTRIES / 0.25
600
400
200
0
−4
−2
0
2
4
δX (cm) x P_T (GeV) / 15 cm x GeV

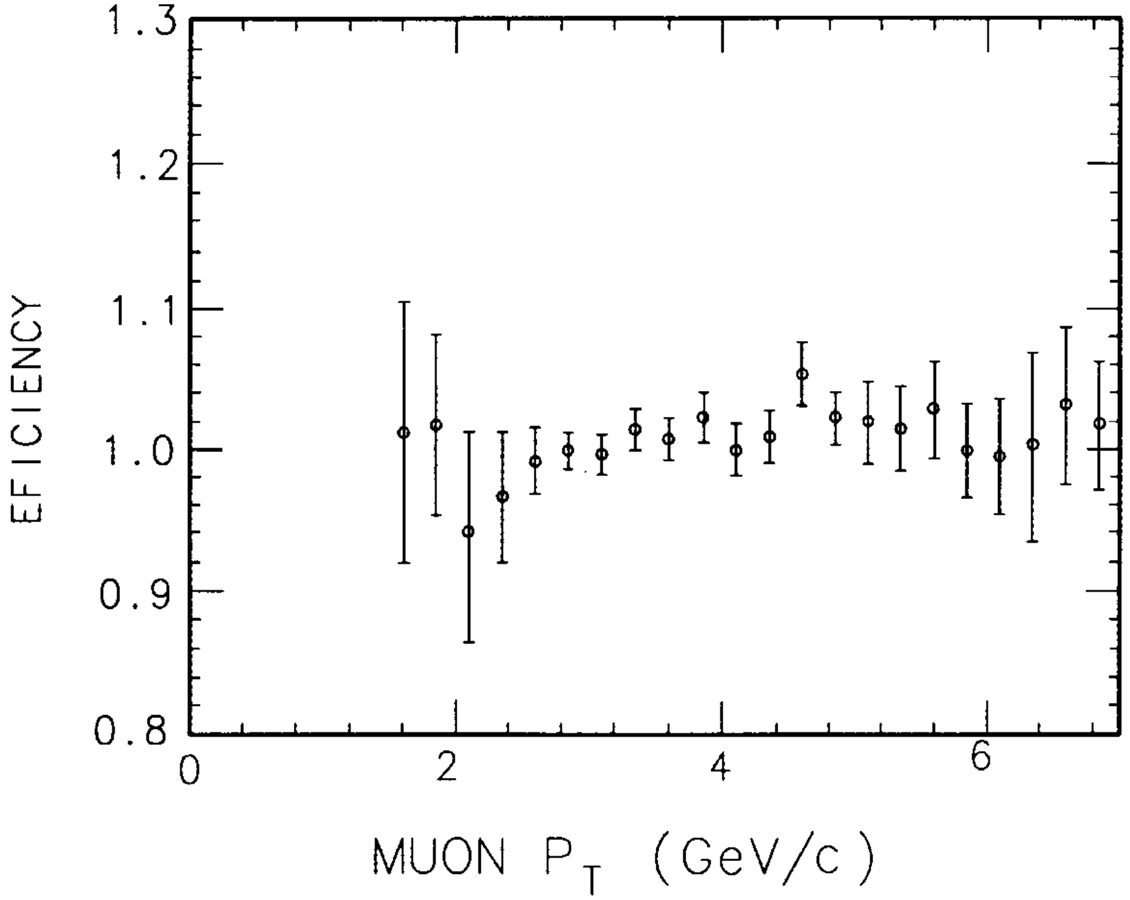
1.3
1.2
1.1
1.0
0.9
0.8
EFICIENCY
0
2
4
6
MUON P_T (GeV/c)

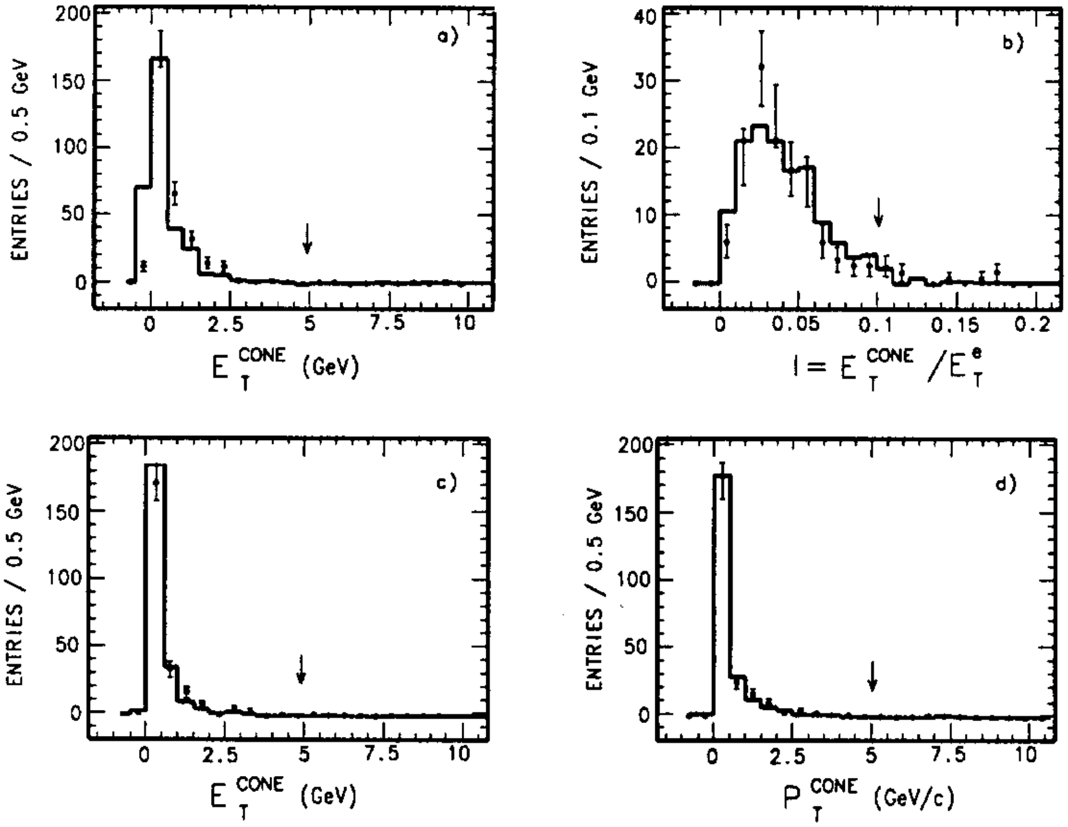
a)
ENTRIES / 0.5 GeV
0
50
100
150
200
0
2.5
5
7.5
10
E_T^{CONE} (GeV)
b)
ENTRIES / 0.1 GeV
0
10
20
30
40
0
0.05
0.1
0.15
0.2
$I = E_T^{CONE} / E_T^{e}$
c)
ENTRIES / 0.5 GeV
0
50
100
150
200
0
2.5
5
7.5
10
E_T^{CONE} (GeV)
d)
ENTRIES / 0.5 GeV
0
50
100
150
200
0
2.5
5
7.5
10
P_T^{CONE} (GeV/c)

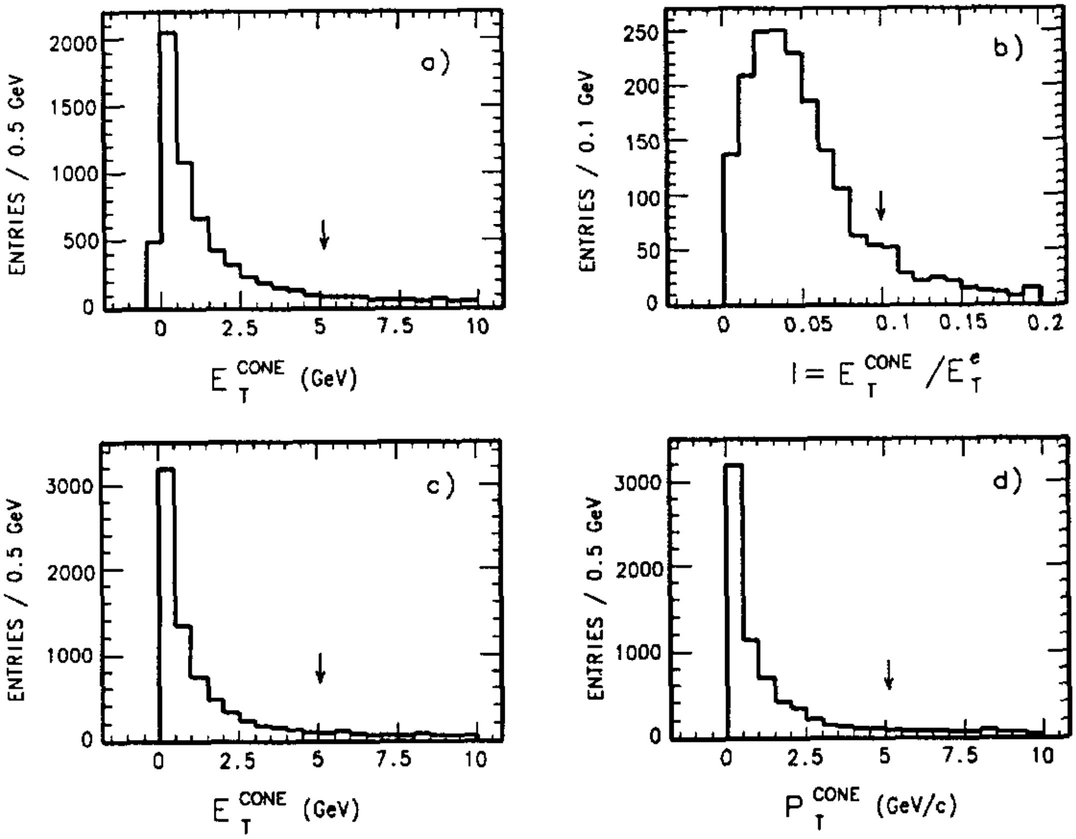
a)
ENTRIES / 0.5 GeV
0
500
1000
1500
2000
0
2.5
5
7.5
10
E_T^{CONE} (GeV)
b)
ENTRIES / 0.1 GeV
0
50
100
150
200
250
0
0.05
0.1
0.15
0.2
$I = E_T^{CONE} / E_T^e$
c)
ENTRIES / 0.5 GeV
0
1000
2000
3000
0
2.5
5
7.5
10
E_T^{CONE} (GeV)
d)
ENTRIES / 0.5 GeV
0
1000
2000
3000
0
2.5
5
7.5
10
P_T^{CONE} (GeV/c)

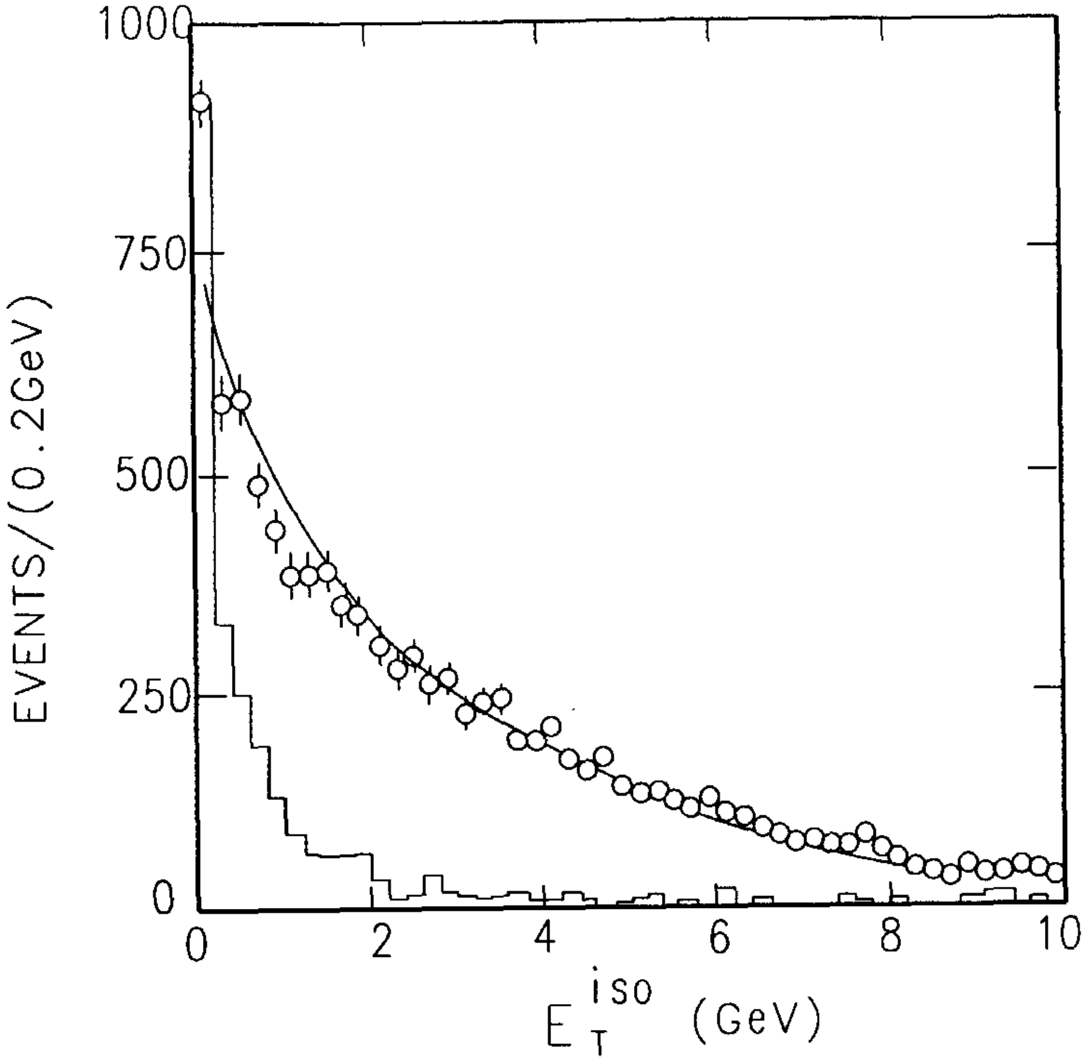
1000
750
500
250
0
EVENTS/(0.2GeV)
0
2
4
6
8
10
E_T^{iso} (GeV)

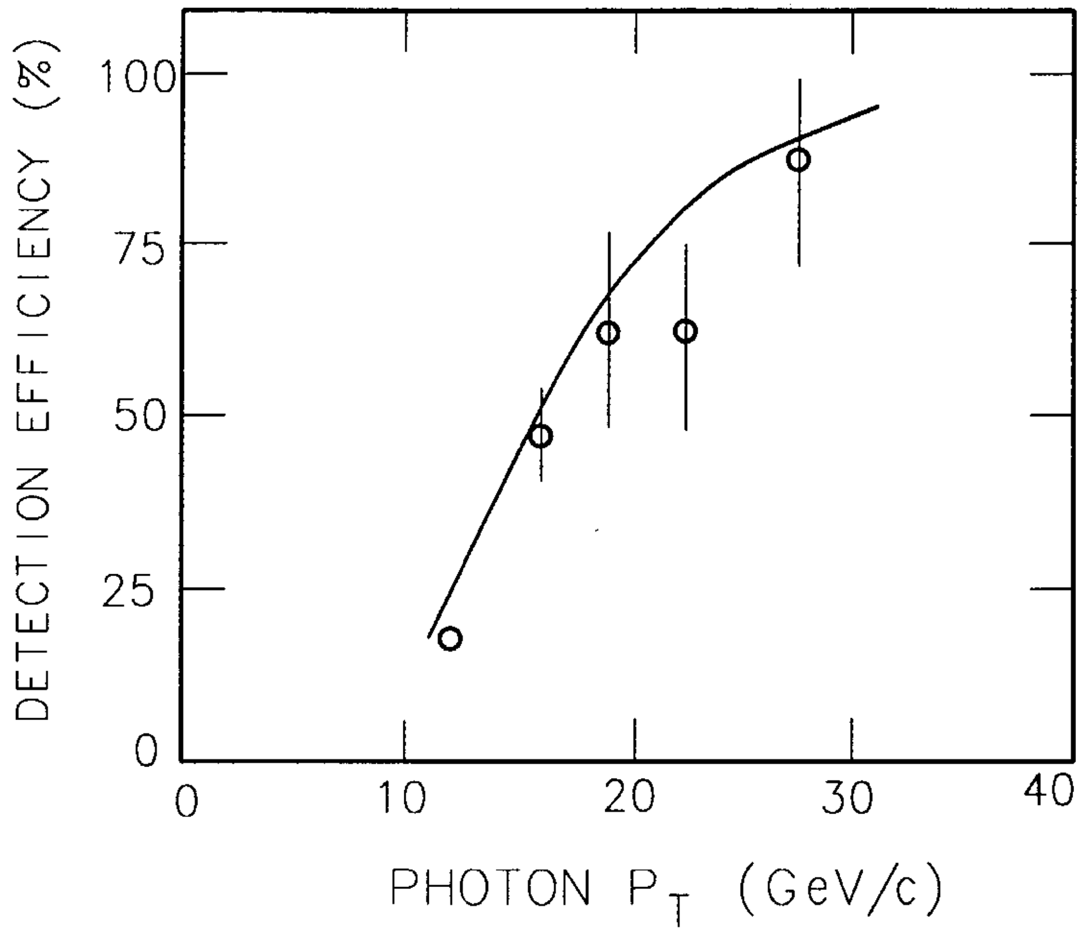
DETECTION EFFICIENCY (%)
0
25
50
75
100
0
10
20
30
40
PHOTON P_T (GeV/c)

mc 18-91

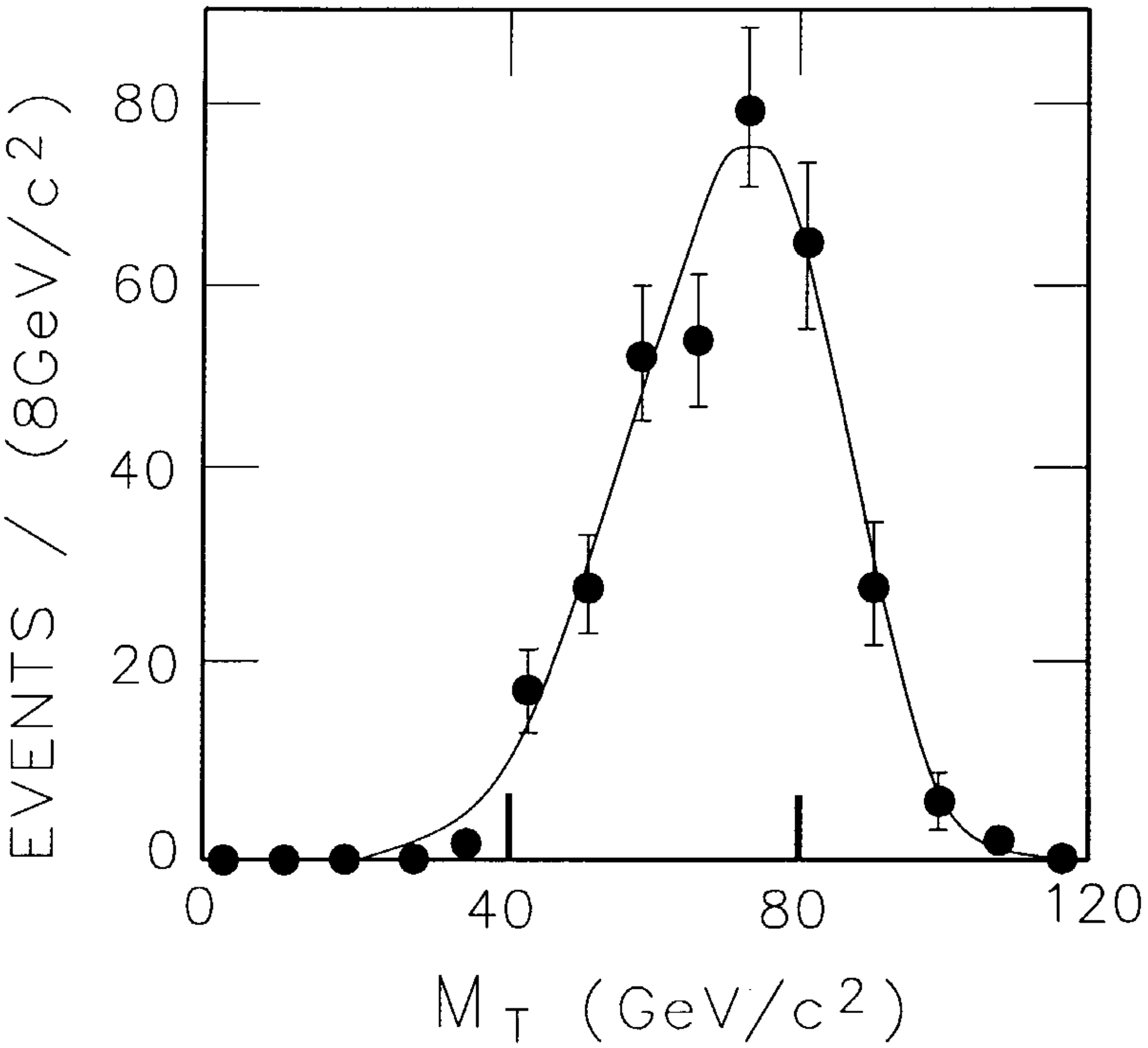
EVENTS / (8GeV/c²)
0
20
40
60
80
0
40
80
120
M_T (GeV/c²)

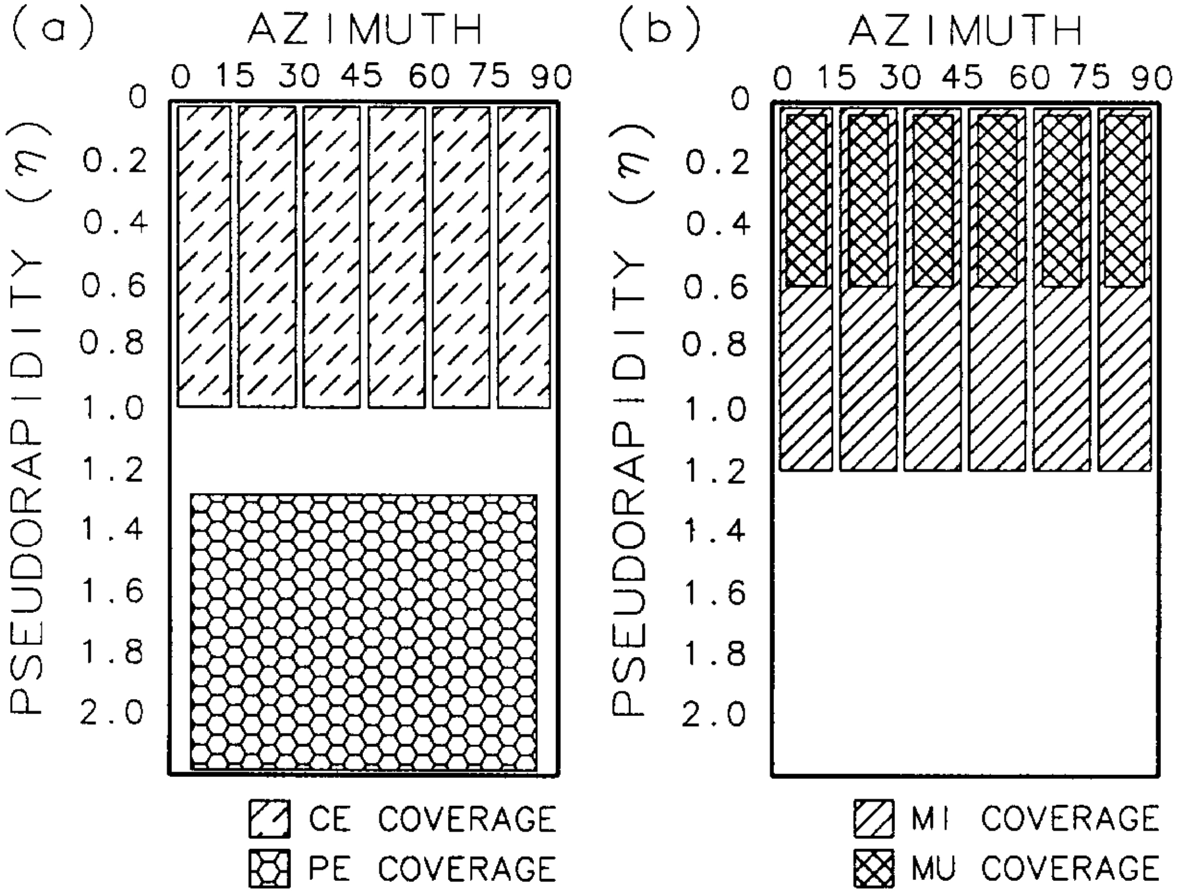
(a)
AZIMUTH
0 15 30 45 60 75 90
PSEUDORAPIDITY (η)
0
0.2
0.4
0.6
0.8
1.0
1.2
1.4
1.6
1.8
2.0
CE COVERAGE
PE COVERAGE
(b)
AZIMUTH
0 15 30 45 60 75 90
PSEUDORAPIDITY (η)
0
0.2
0.4
0.6
0.8
1.0
1.2
1.4
1.6
1.8
2.0
MI COVERAGE
MU COVERAGE

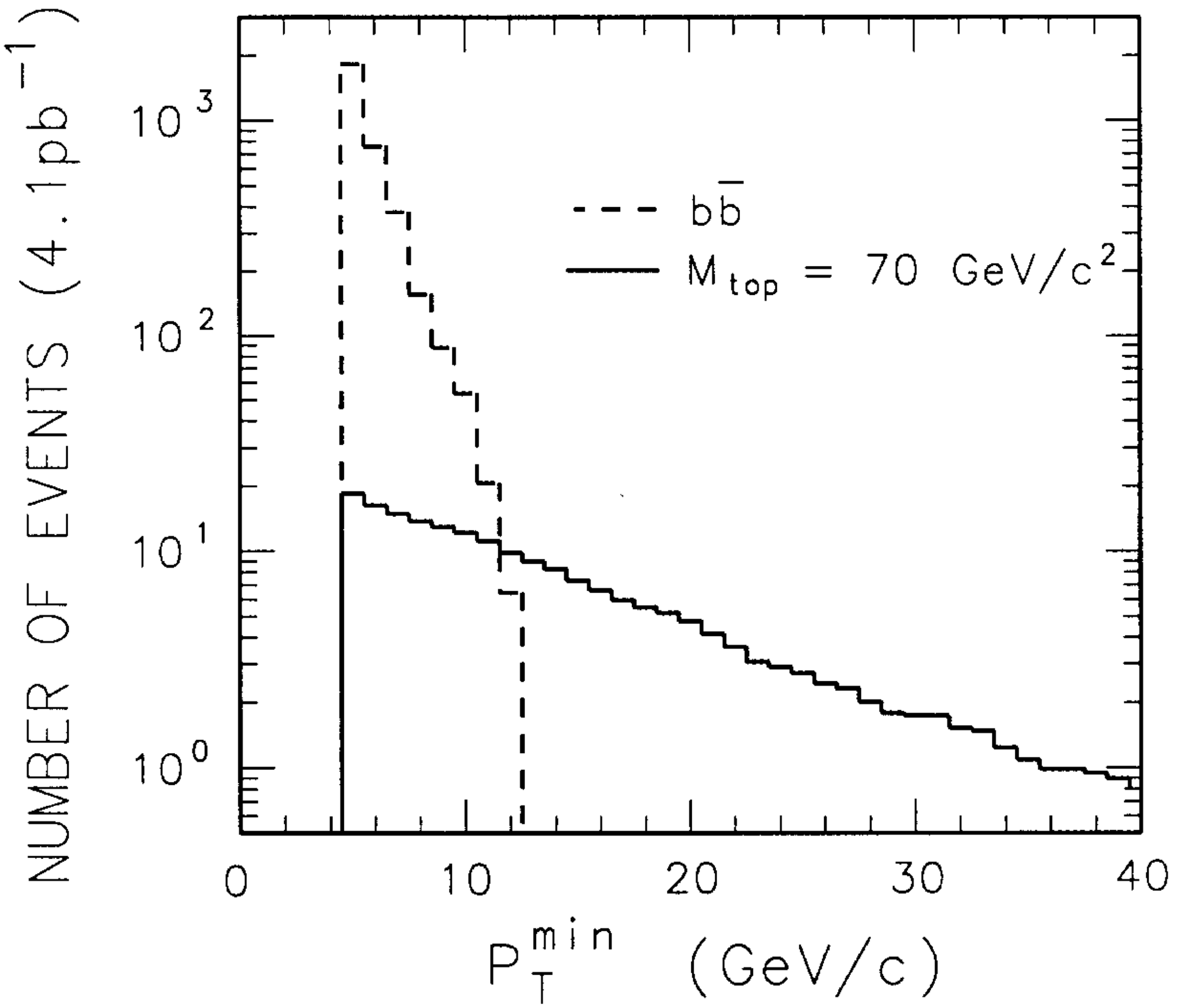
NUMBER OF EVENTS (4.1pb^{-1})
10^3
10^2
10^1
10^0
0
10
20
30
40
P_T^{min} (GeV/c)
$b\bar{b}$
M_{top} = 70 GeV/c^2

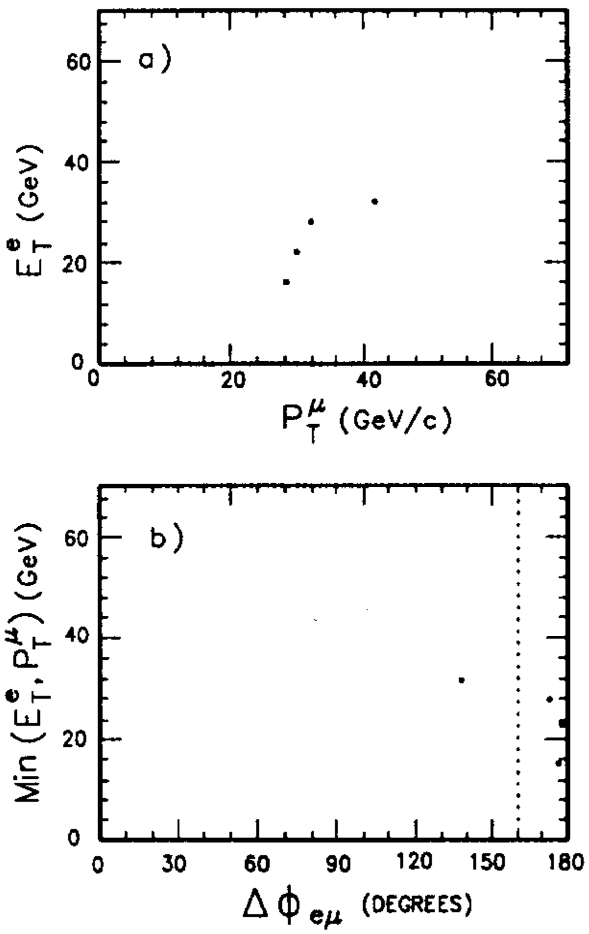
a)
E_T^e (GeV)
0
20
40
60
0
20
40
60
P_T^μ (GeV/c)
b)
Min (E_T^e, P_T^μ) (GeV)
0
20
40
60
0
30
60
90
120
150
180
$\Delta\phi_{e\mu}$ (DEGREES)

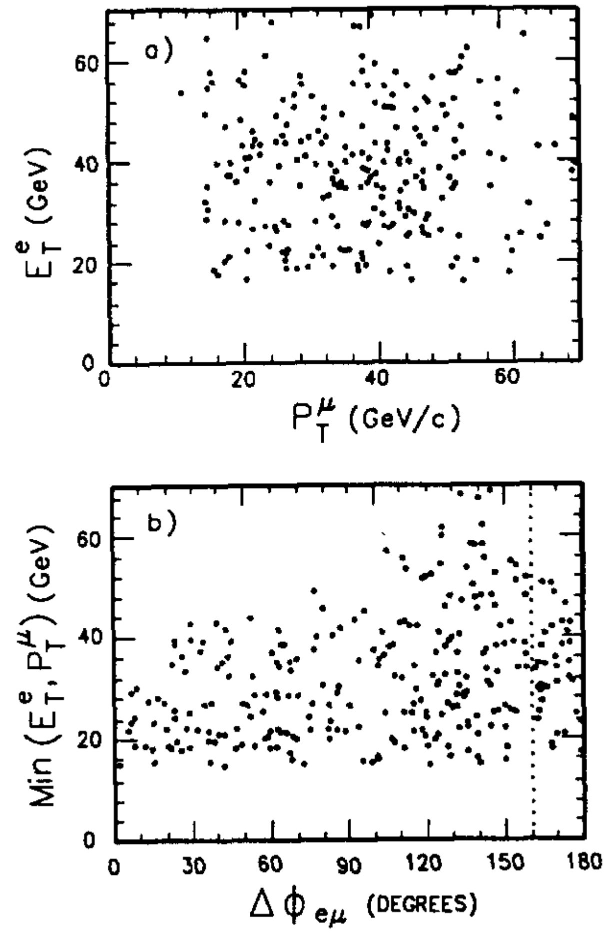
a)
E_T^e (GeV)
0
20
40
60
0
20
40
60
P_T^μ (GeV/c)
b)
Min (E_T^e, P_T^μ) (GeV)
0
20
40
60
0
30
60
90
120
150
180
$\Delta\phi_{e\mu}$ (DEGREES)

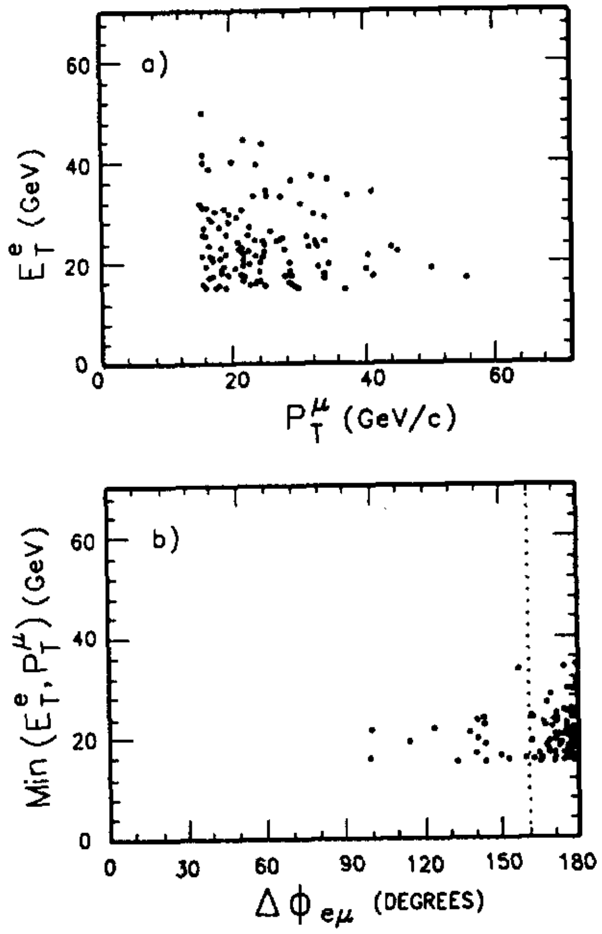
a)
E_T^e (GeV)
0
20
40
60
0
20
40
60
P_T^μ (GeV/c)
b)
Min (E_T^e, P_T^μ) (GeV)
0
20
40
60
0
30
60
90
120
150
180
$\Delta\phi_{e\mu}$ (DEGREES)

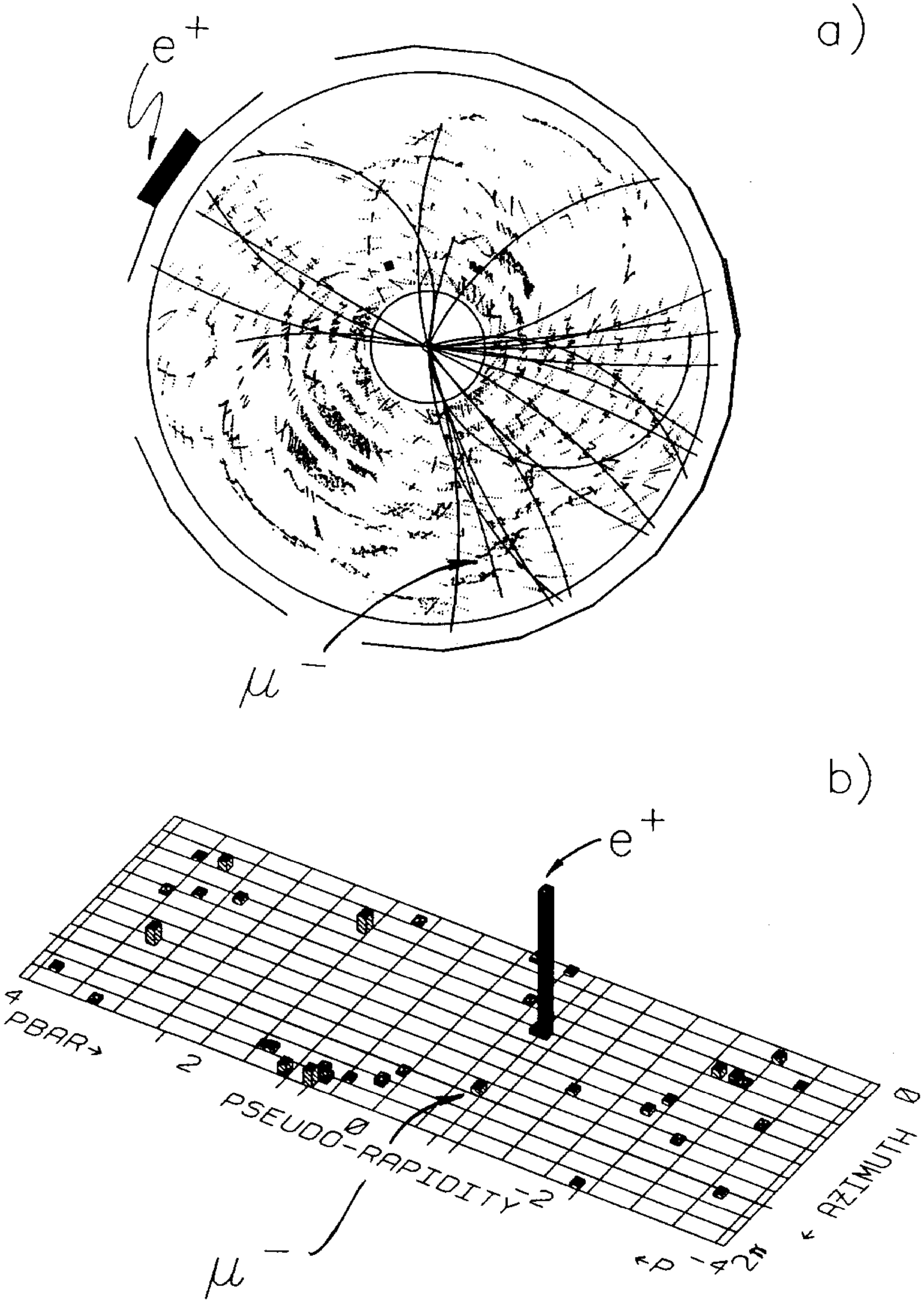

2.5

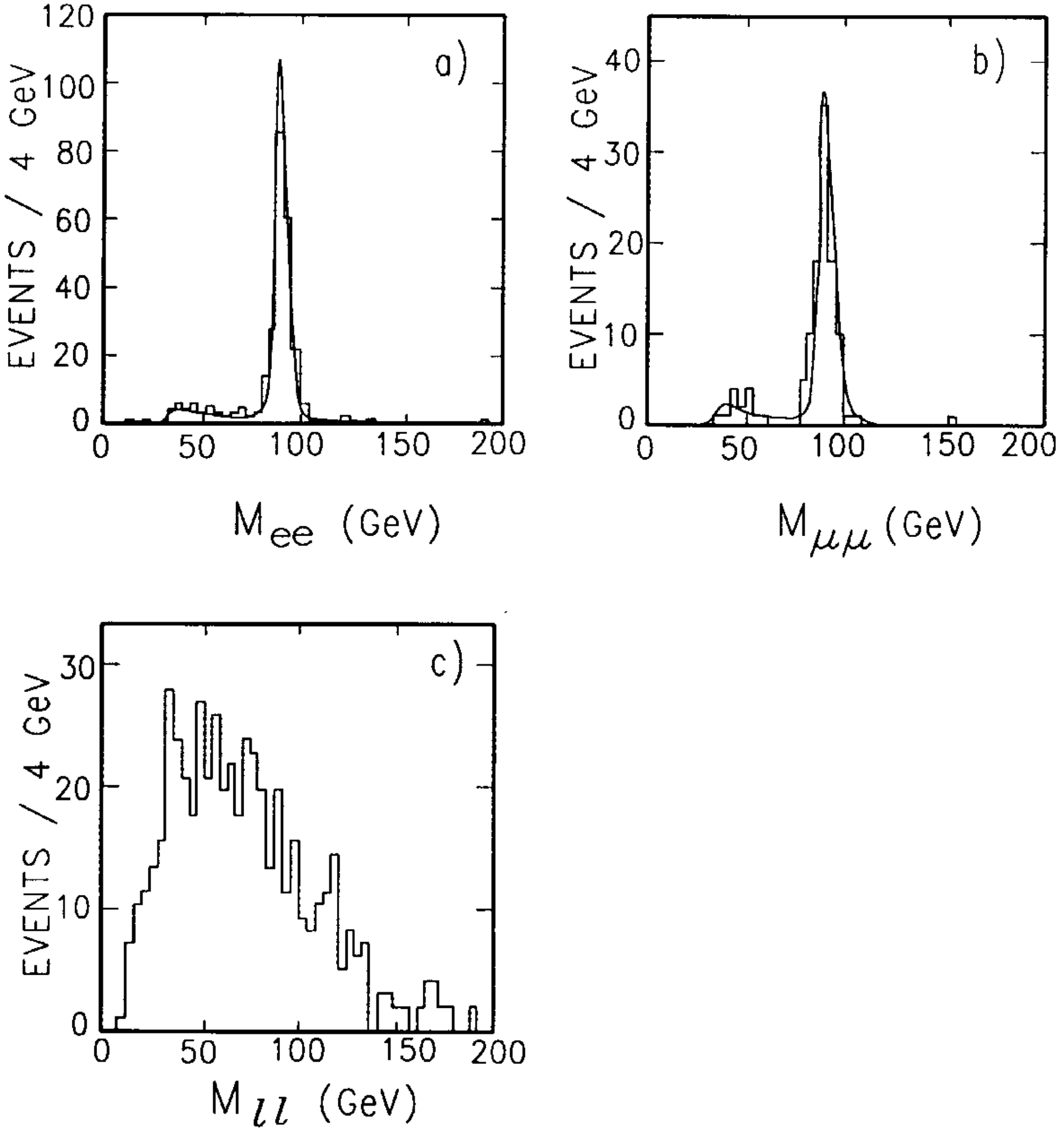
a)
EVENTS / 4 GeV
0
20
40
60
80
100
120
0
50
100
150
200
M_{ee} (GeV)
b)
EVENTS / 4 GeV
0
10
20
30
40
0
50
100
150
200
$M_{\mu\mu}$ (GeV)
c)
EVENTS / 4 GeV
0
10
20
30
0
50
100
150
200
M_{ll} (GeV)

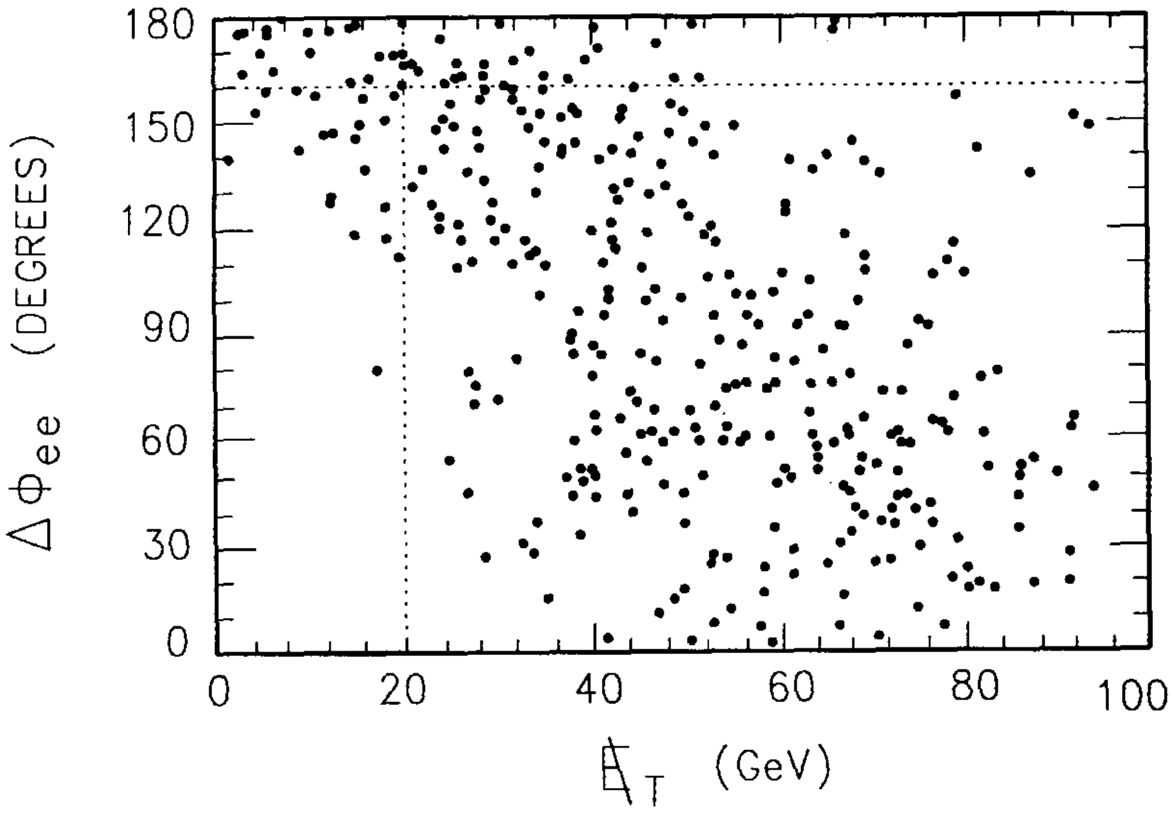
$\Delta\phi_{ee}$ (DEGREES)
0
30
60
90
120
150
180
0
20
40
60
80
100
$\not{E}_T$ (GeV)

nic 27

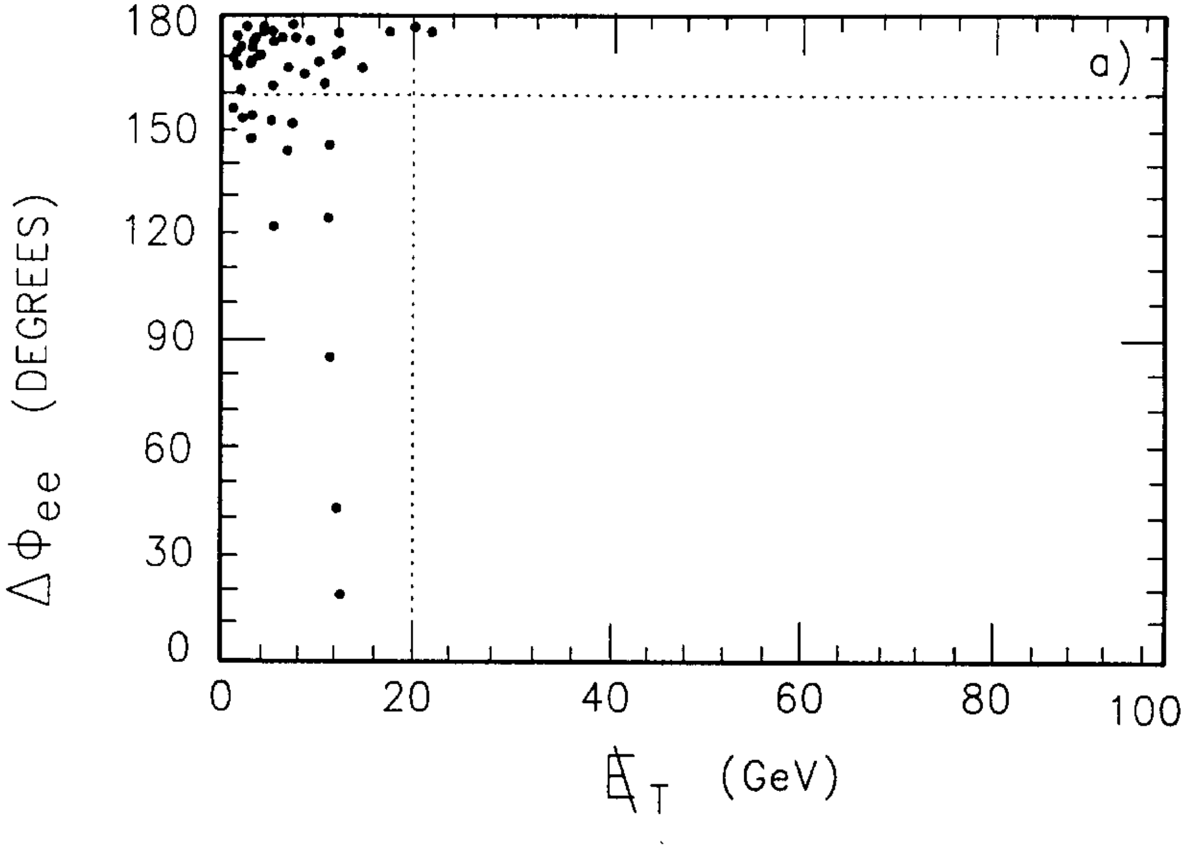

180
150
120
90
60
30
0
0
20
40
60
80
100
$\Delta\Phi_{ee}$ (DEGREES)
$\not\!E_T$ (GeV)
a)

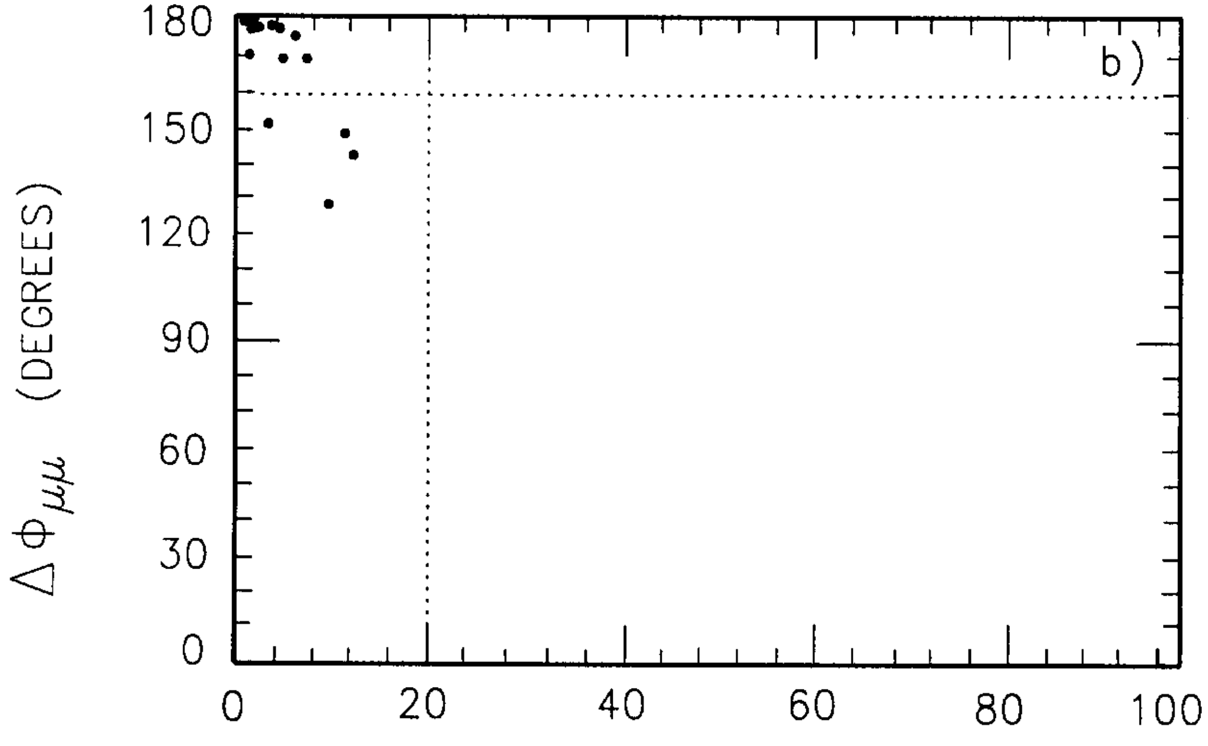

180
150
120
90
60
30
0
0
20
40
60
80
100
$\Delta\Phi_{\mu\mu}$ (DEGREES)
$\not\!E_T$ (GeV)
b)

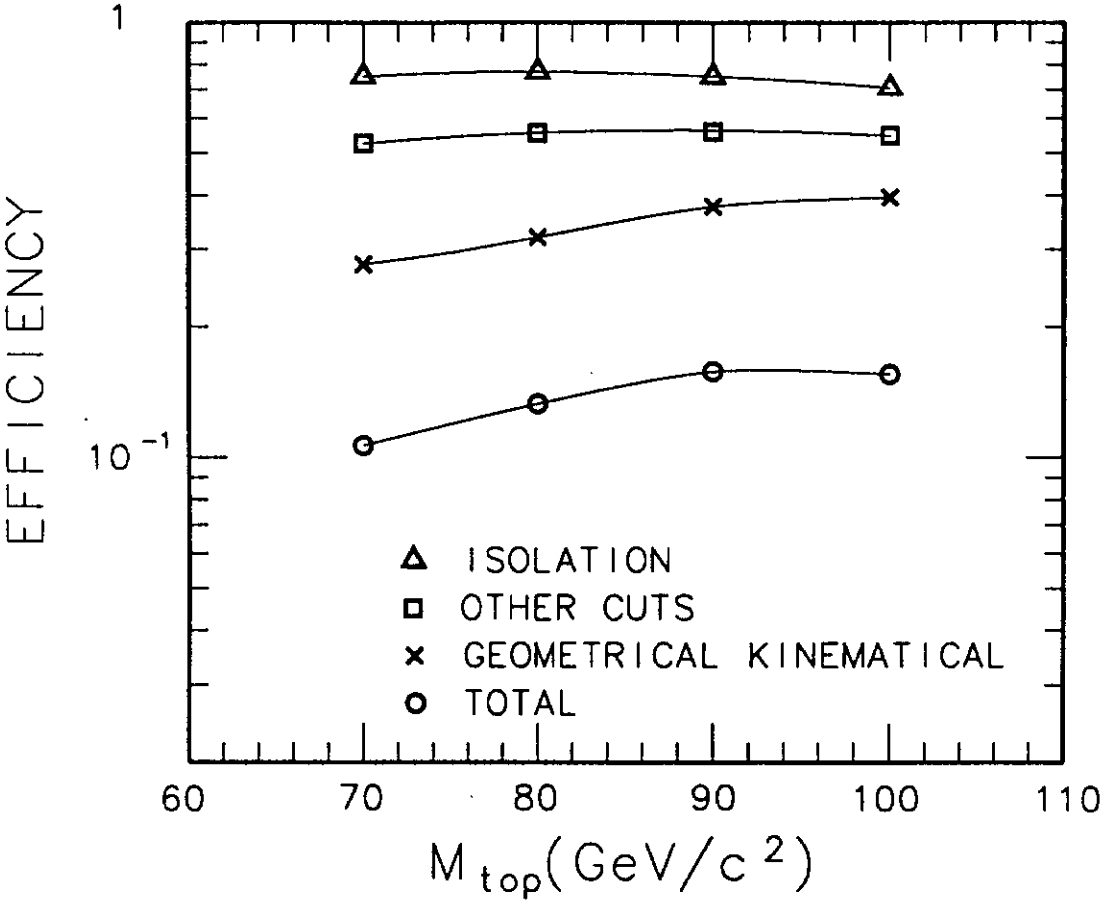
1
10^{-1}
EFFICIENCY
60
70
80
90
100
110
M top (GeV/c 2)
△ ISOLATION
□ OTHER CUTS
× GEOMETRICAL KINEMATICAL
○ TOTAL

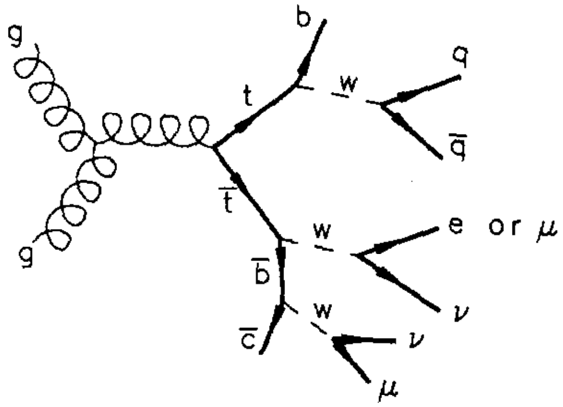
g
g
t
b
w
q
q̄
t̄
w
e or μ
ν
b̄
w
c̄
ν
μ

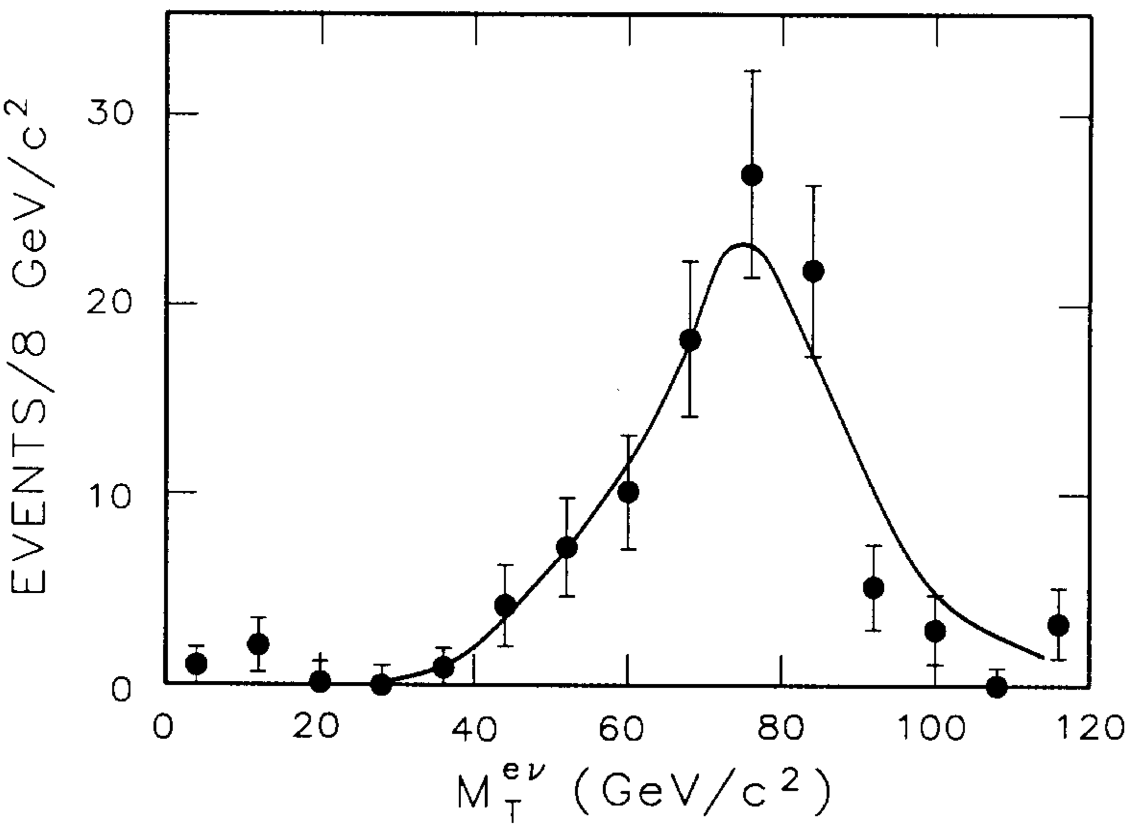
EVENTS/8 GeV/c^2
0
10
20
30
0
20
40
60
80
100
120
$M_T^{e\nu}$ (GeV/c^2)

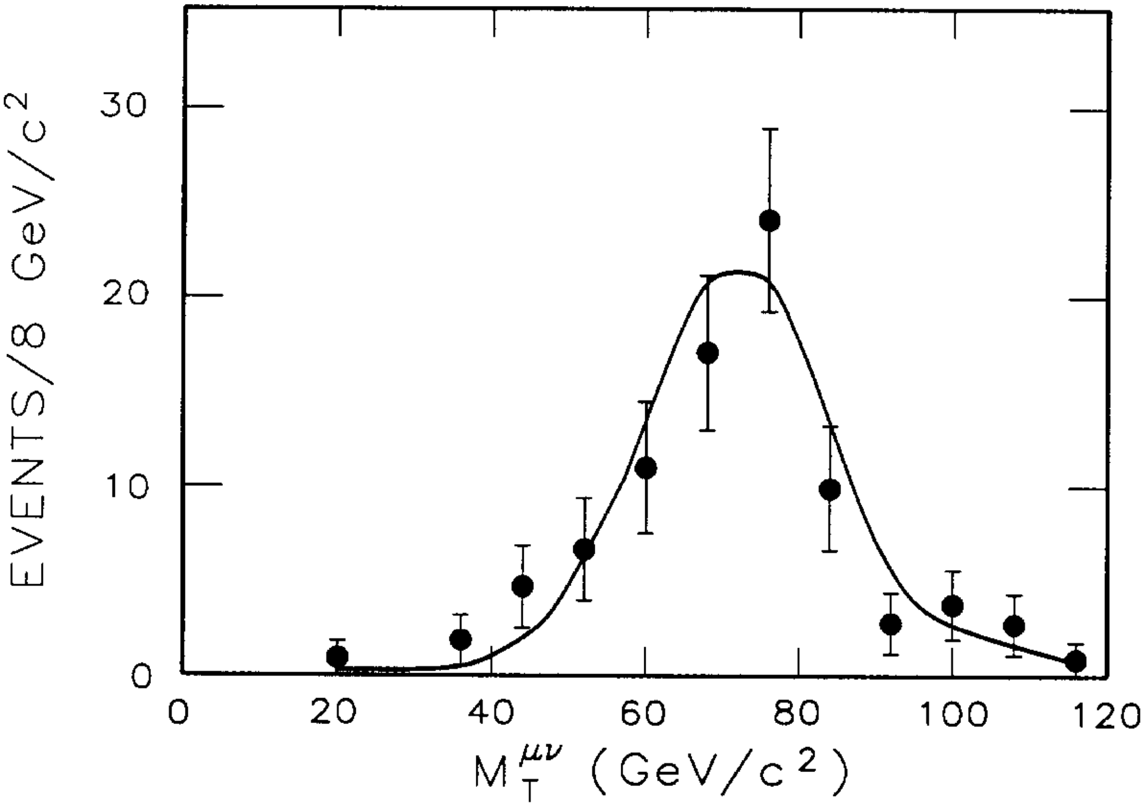
EVENTS/8 GeV/c^2
30
20
10
0
0
20
40
60
80
100
120
$M_T^{\mu\nu}$ (GeV/c^2)

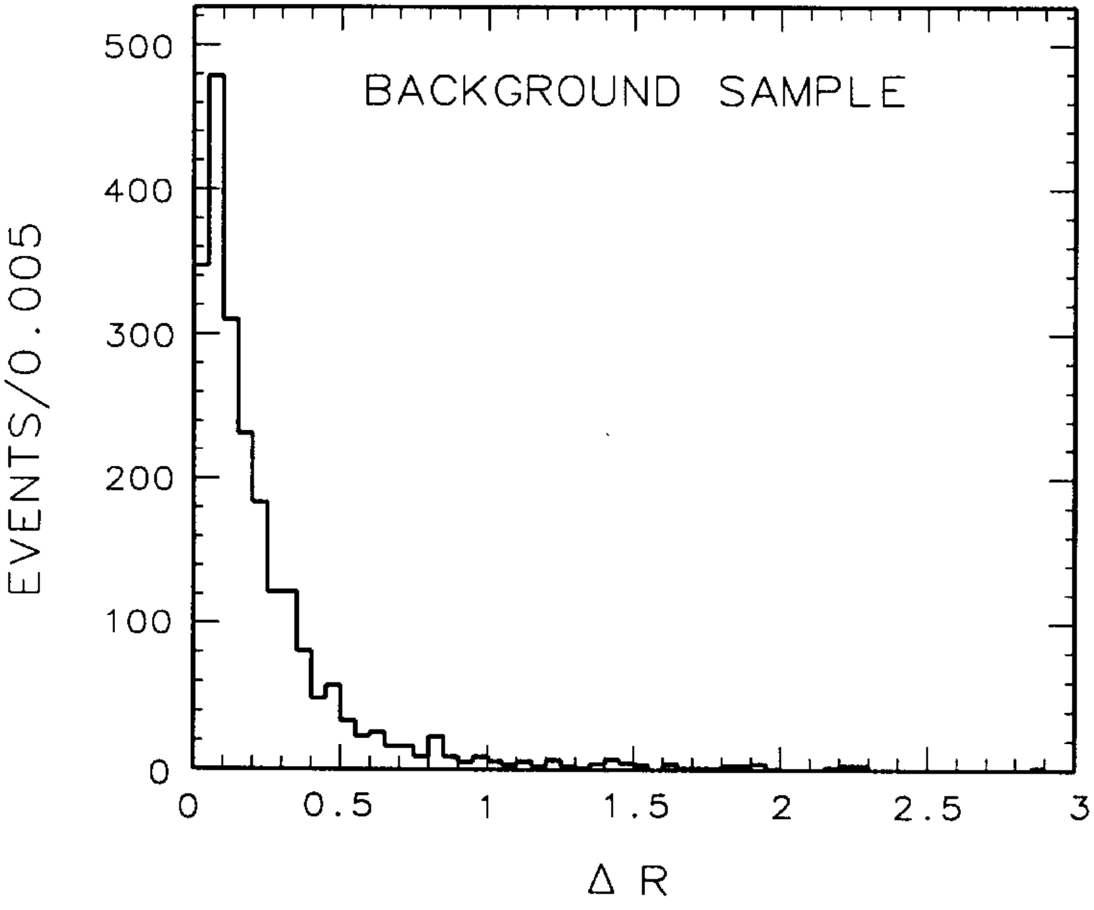
BACKGROUND SAMPLE
EVENTS/0.005
0
100
200
300
400
500
0
0.5
1
1.5
2
2.5
3
Δ R

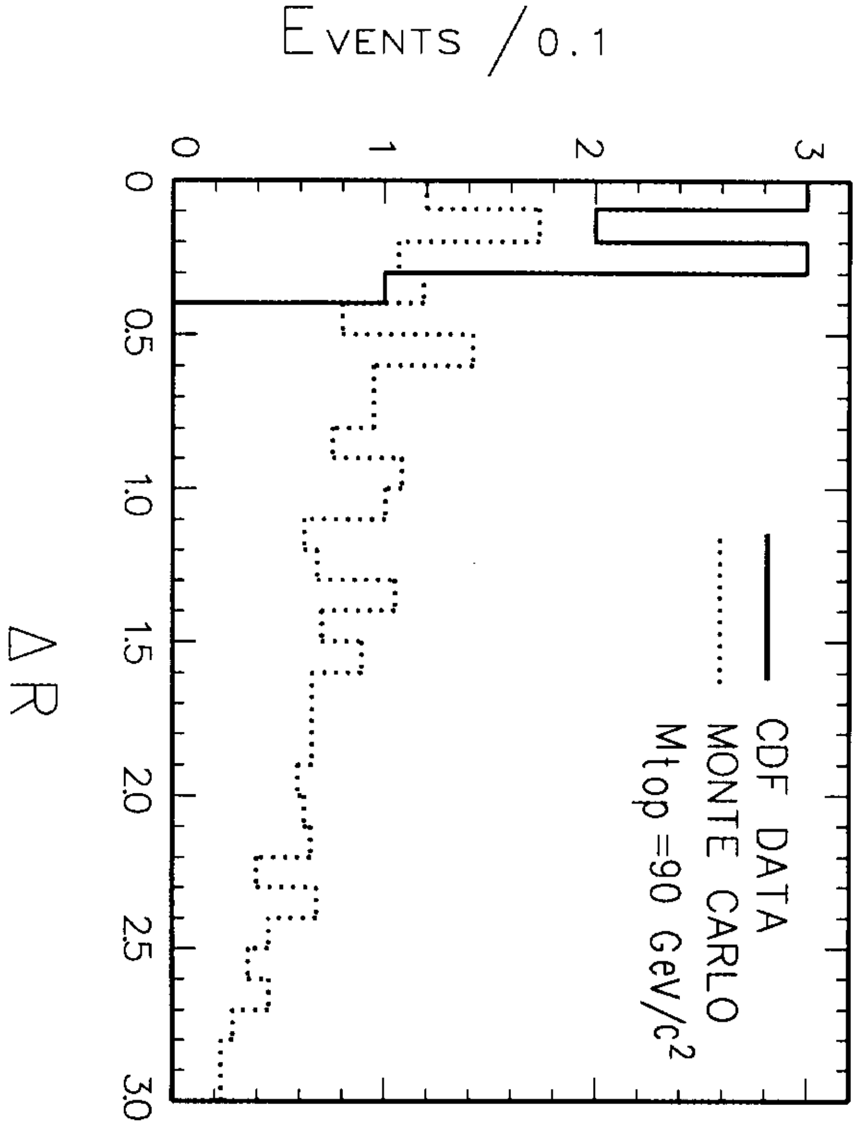
Events /0.1
0
1
2
3
0
0.5
1.0
1.5
2.0
2.5
3.0
ΔR
CDF DATA
MONTE CARLO
Mtop =90 GeV/c^2

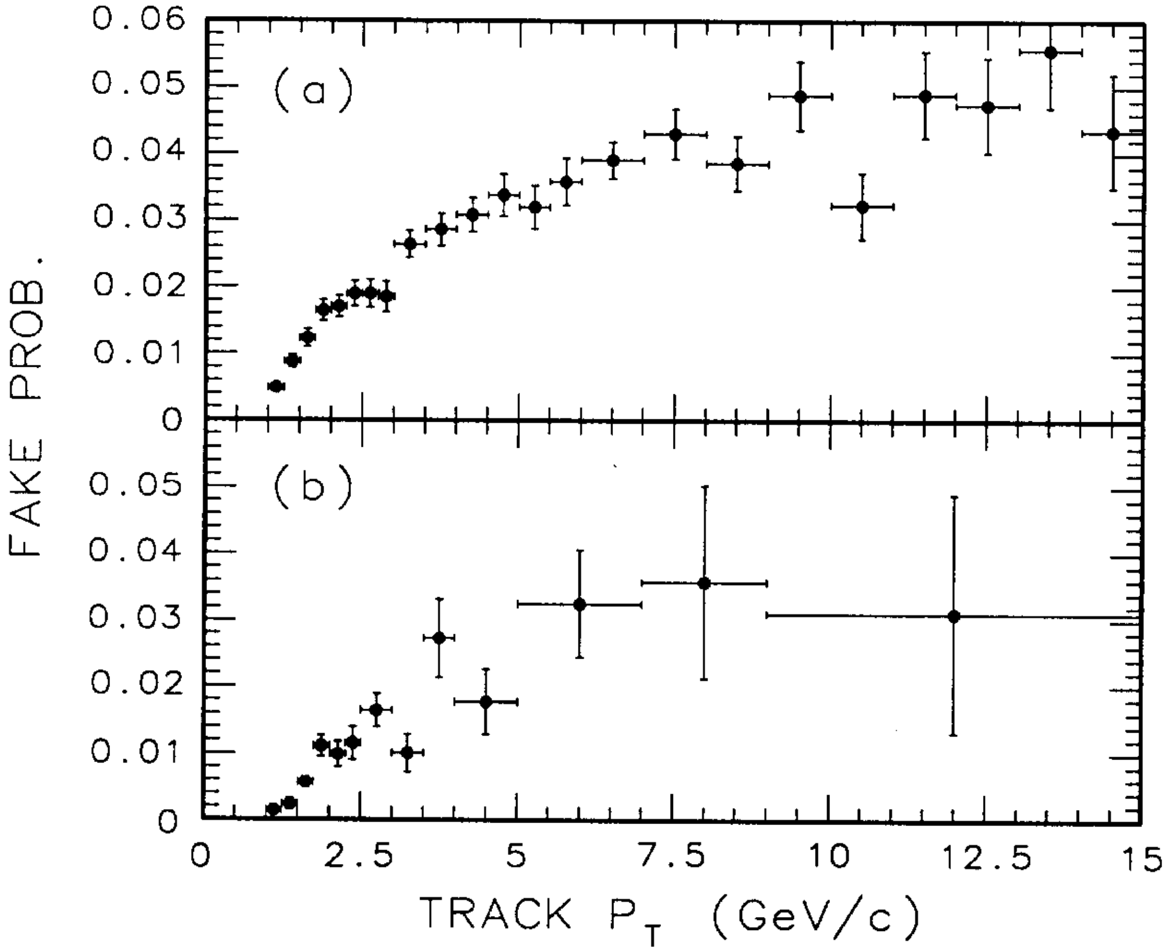
0.06
0.05
0.04
0.03
0.02
0.01
0
(a)
(b)
FAKE PROB.
0
2.5
5
7.5
10
12.5
15
TRACK P_T (GeV/c)

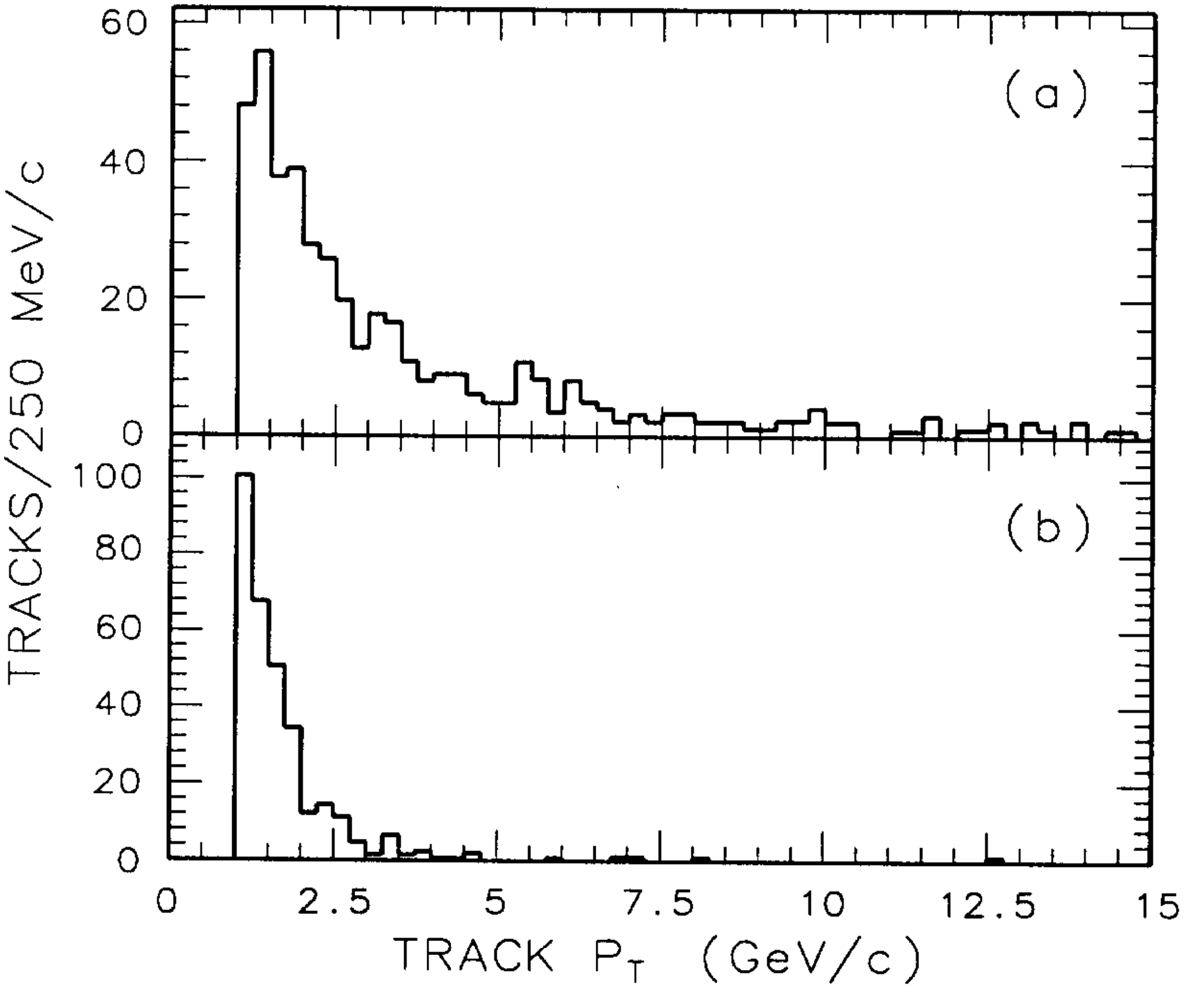

TRACKS/250 MeV/c
60
40
20
0
(a)
100
80
60
40
20
0
(b)
0
2.5
5
7.5
10
12.5
15
TRACK P_T (GeV/c)

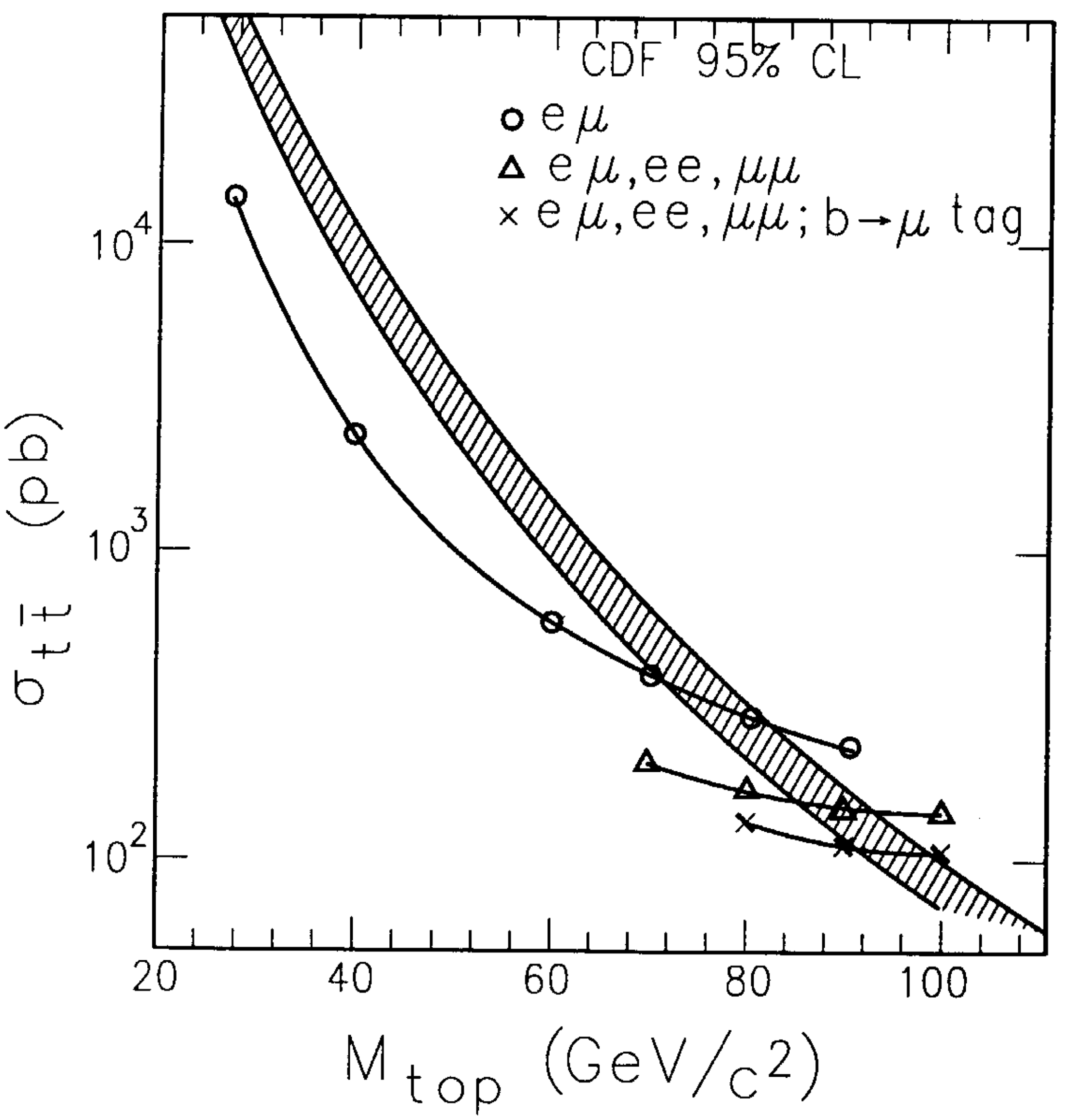
CDF 95% CL
○ $e\mu$
△ $e\mu, ee, \mu\mu$
× $e\mu, ee, \mu\mu; b \rightarrow \mu$ tag
10^4
10^3
10^2
$\sigma_{t\bar{t}}$ (pb)
20
40
60
80
100
M_{top} (GeV/c^2)